



UNIVERSITÀ
DEGLI STUDI
FIRENZE

DOTTORATO DI RICERCA IN SCIENZE CHIMICHE

CICLO XXXV

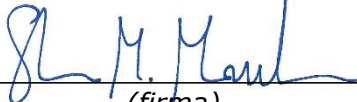
COORDINATRICE Prof.ssa Anna Maria Papini

ANALYSIS AND STUDY OF INDUSTRIALLY AND
TECHNOLOGICALLY INTERESTING SURFACES

Settore Scientifico Disciplinare CHIM/01

Dottorando

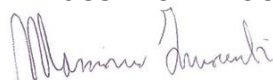
Dott. Stefano Mauro Martinuzzi



(firma)

Tutore


Prof. Massimo Innocenti



(firma)

Co-Tutore

Dott. Stefano Caporali



(firma)

Coordinatrice

Prof.ssa Anna Maria Papini

(firma)

Anni 2019/2022

Section 1	7
1 Metallic coating processes.....	8
1.1 Electrodeposition.....	8
1.1.1 Introduction.....	8
1.1.1.1 Faraday’s Laws.....	11
1.1.1.2 Current Efficiency	11
1.1.1.3 Current Density.....	12
1.1.1.4 Equilibrium Potential and Overpotential	12
1.1.2 Electrolytes Used for Electrodeposition	13
1.1.3 Operating Parameters in Electrodeposition Processes.....	14
1.1.4 Surface Preparation.....	17
1.1.4.1 Physicochemical cleaning	18
1.1.4.2 Mechanical methods	19
1.1.4.3 Rinsing.....	19
1.1.5 Electrodeposition	19
1.1.6 Electrodeposited coatings defects	20
1.1.7 Composition, Structure, and Properties of Electrodeposited Coatings.....	24
1.2 Physical Vapor Deposition (PVD).....	27
1.2.1 Introduction.....	27
1.2.2 Thermal Evaporation.....	29

1.2.2.1	Resistance Heating Method	29
1.2.2.2	Electron Beam Evaporation	30
1.2.2.3	Molecular Beam Epitaxy	31
1.2.2.4	Pulsed Laser Deposition	33
1.2.3	Sputtering.....	36
1.2.3.1	Introduction.....	36
1.2.3.2	Magnetron Sputtering	39
1.2.3.2.1	Direct Current (DC) Magnetron Sputtering	39
1.2.3.2.2	Radio Frequency (RF) Magnetron Sputtering	41
1.2.3.2.3	Reactive Sputter Deposition	43
1.2.3.2.4	Ion Beam Sputtering	44
1.2.4	Arc Discharge.....	44
1.2.5	Common features of PVD processes.....	47
1.2.5.1	Advantages	47
1.2.5.2	Disadvantages.....	47
1.3	Metallic coating characterization	49
1.3.1	Corrosion	49
1.3.1.1	Introduction.....	49
1.3.1.2	Forms of Corrosion	49
1.3.1.3	Corrosion Thermodynamics	54
1.3.1.4	Corrosion Kinetics and Polarization Curves.....	59

1.3.1.5	Corrosion Testing.....	63
1.3.1.5.1	Salt Spray Test.....	63
1.3.1.5.2	Weight-Loss Measurements	65
1.3.1.5.3	Electrochemical Tests	65
1.4	Metal Coatings Thickness Measurement Techniques	84
1.4.1	Introduction.....	84
1.4.2	Destructive Methods.....	85
1.4.2.1	Microscopical Methods: Light and Electron Microscopy	85
1.4.2.2	Profilometric stylus method	89
1.4.2.3	Gravimetric Methods.....	90
1.4.2.4	Weight Gain Method	91
1.4.2.5	Strip and weigh method	91
1.4.2.6	Coulometric method.....	91
1.4.2.7	Ball crater test.....	92
1.4.3	Non-destructive Methods	93
1.4.3.1	Magnetic methods.....	93
1.4.3.2	X-ray Fluorescence Spectroscopy	94
Section 2	97
2	A robust and cost-effective protocol to fabricate calibration standards for the thickness determination of metal coatings by XRF	98
2.1	Introduction	98

2.2	Material and methods	104
2.2.1	Electroplating	105
2.2.2	Current density simulation (IDC2D)	106
2.2.3	XRF measurements.....	106
2.2.4	Cross-section analysis.....	107
2.3	Results and Discussion	108
2.3.1	Current density simulation.....	108
2.3.2	XRF measurements.....	111
2.3.2.1	Deposit thickness distribution	111
2.3.2.2	Galvanic deposition reproducibility.....	113
2.3.2.3	LM and SEM-EDS cross-sectional thickness measurement 115	
2.3.2.4	XRF Thickness measurement comparison.....	117
2.4	Conclusions	119
2.5	Addendum.....	120
2.5.1	Introduction.....	121
2.5.1.1	Finite Element Method.....	121
2.5.1.2	FEM in Electrochemistry.....	122
2.5.1.3	Electrodeposition simulation with COMSOL Multiphysics 124	
2.5.2	Numerical simulation	125

2.5.3	Results and Discussion	128
2.5.4	Conclusions.....	131
Section 3	142
3	Electrodeposited white bronzes on brass: corrosion in 3.5% sodium chloride solution	143
3.1	Introduction	143
3.2	Materials and Methods.....	145
3.2.1	White Bronzes Electrodeposition.....	145
3.2.2	FIB/SEM measurements.....	146
3.2.3	XPS Measurements	147
3.2.4	XRD experiments.....	148
3.2.5	Color Measurements.....	148
3.2.6	Corrosion Measurements.....	149
3.3	Results and Discussion	150
3.3.1	SEM investigation.....	150
3.3.1.1	Surface Morphology	150
3.3.1.2	Coating Thickness	152
3.3.1.3	Bulk composition of the coatings	154
3.3.2	Surface composition (XPS)	157
3.3.3	XRD Measurements.....	162
3.3.4	Characterization of the color	164

3.3.5	Electrochemical corrosion in 3.5% sodium chloride	165
3.4	Conclusion.....	175
Section 4	177
4	A Comparative Research on Corrosion Behaviour of Electroplated and Magnetron Sputtered Chromium Coatings	178
4.1	Introduction	178
4.2	Materials and Methods.....	182
4.2.1	Cr Thin Films Deposition	182
4.2.2	Characterization Methods.....	183
4.3	Results.....	186
4.3.1	XRF Thickness Measurement	186
4.3.2	Color Measurement	187
4.3.3	Morphological and Near Surface Chemical Investigation.	189
4.3.4	X-Ray Investigation.....	191
4.3.5	Electrochemical Characterization	192
4.3.5.1	OCP	192
4.3.5.2	Potentiodynamic Polarization	194
4.3.5.3	Electrochemical Impedance Spectroscopy (EIS).....	195
4.3.5.4	Salt Spray Test (Free Corrosion)	197
4.4	Conclusion.....	198
References	200

Section 1

1 Metallic coating processes

1.1 Electrodeposition

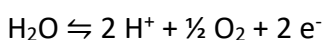
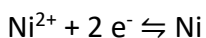
1.1.1 *Introduction*

Electrodeposition is an electrochemical process that allows the preparation of solid deposits on the surface of conductive materials. It is a commercially highly relevant process, providing the basis for many industrial applications, such as electro-winning, refining, and metal plating. Metal plating is the process that has perhaps the closest contact with most people's everyday life because we are surrounded by things with a protective or decorative coating, such as watches, buttons, belt buckles, doorknobs, handlebars, etc.

Electrodeposits are formed by the action of an electric current passing through an electrochemical cell. This device consists of two electrodes, a cathode, and an anode, immersed in an electrolyte. Cathode and anode are referred to as working electrode (WE) and counter electrode (CE), respectively. The working electrode consists of the object to be electrodeposited, while the counter electrode completes the electrical circuit. Electrolytes are usually aqueous solutions containing positive and negative ions, prepared by dissolving metal salts. The electric current that flows between the two conductive electrodes in the presence of an external voltage is because of the motion of charged species, via migration and diffusion, towards the surfaces of the polarized electrodes. At the surface of the electrodes, the conduction mechanism must change from ionic to electronic, an interface process mediated by the occurrence of

electrochemical reactions that promote the reduction or the oxidation (redox reactions) of the ionic species.

An electrochemical cell with a power source is illustrated in Figure 1. The metallic salt NiSO_4 (nickel sulfate) dissolved in water is a practical example of an electrolyte for nickel-plating metallic objects. In this example, the object to be plated is a key placed as the working electrode. By applying an external voltage with the battery's negative terminal connected to the working electrode, the Ni^{2+} moves to this electrode, where deposition occurs, and the SO_4^{2-} moves toward the positively charged counter-electrode. An essential characteristic of electrochemical reactions is that the exchange of charge does not occur between chemical species, as in a typical chemical reaction, but between chemical species and the electrode. The electrochemical reaction that is most important for the electrodeposition process is the one that occurs at the WE. As for the example in Figure 1, at the cathode occurs the Nickel reduction, while at the anode, the electrolysis of the water:



It is essential that the anode does not limit the electrodeposition reaction. For this reason, it generally has a high surface area with respect to the cathode. Can be distinguished between two types of anode, (1) inert electrodes, also known as dimensionally stable anodes (DSA), which does not participate in the electrochemical reaction, and (2) dissolving anodes (non-inert electrode), which, instead, are made of the same metal to be electrodeposited, whose electrodisolution replenish the solution with electroactive metal ions.

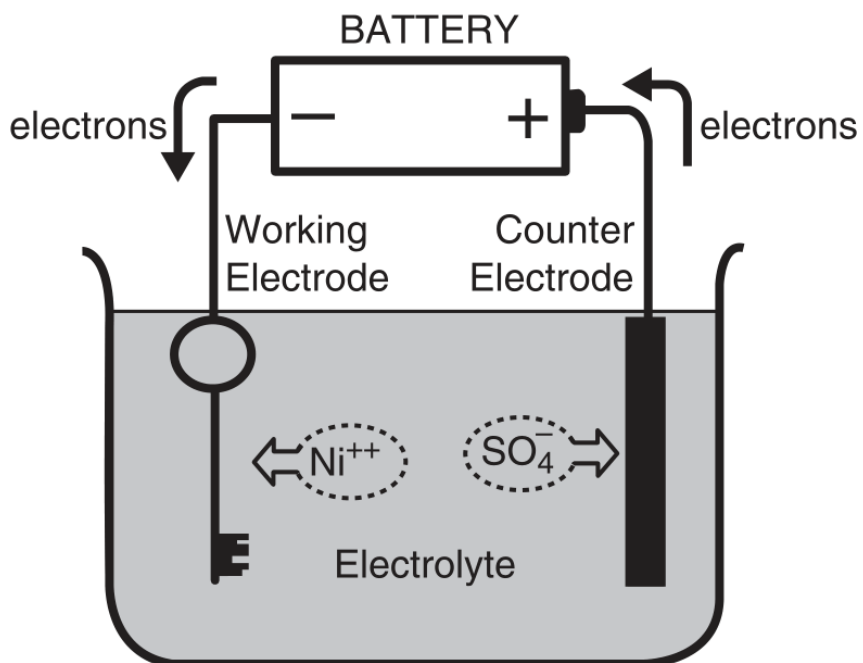


Figure 1 Positively charged nickel ions in the electrolyte are attracted by the negatively charged key (working electrode). At the key surface, they are reduced by gaining two electrons, and metal is deposited.

1.1.1.1 Faraday's Laws

Faraday's laws are fundamental in the quantitative description of the electrodeposition process. It states that the amount of electrochemical reaction that occurs at an electrode is proportional to the quantity of electric charge passed through an electrochemical cell. Mathematically:

$$W = \frac{QM_w}{nF} \quad (1)$$

Where:

- W is the weight of the deposit in g
- Q is the charge in Coulomb
- M_w is the atomic weight of the deposited element in g/mol
- F, is the Faraday constant, which is 96485 C/mol, the amount of electric charge carried by 1 mol, or the Avogadro's number of electrons.

1.1.1.2 Current Efficiency

Cathode efficiency, usually expressed as a percentage, is the ratio of the actual amount of the deposited material to the theoretical amount that should be deposited according to Faraday's Law:

$$CE = \frac{W_{act}}{W_{Theo}} \quad (2)$$

In most practical electrodeposition processes, a certain amount of current is consumed for undesirable processes occurring alongside metal deposition. In aqueous-based electrolytes, one of the most striking side reactions is

hydrogen evolution. Its effect on cathode current efficiency is especially remarkable in the electrodeposition of metals characterized by low overpotentials for hydrogen discharge (e.g., Cu, Ni, Co, Fe, Pt, Cr).

1.1.1.3 Current Density

Another important parameter in electrodeposition is the current density, defined as current in amperes per unit area of the electrode. It is crucial because it governs the rate of the deposition process. The current density is the most practical measure for the rate of any electrochemical process since its value is readily determined from an ammeter reading and the knowledge of the electrode area. Current density is usually assumed to be uniform across the surface. However, any real surface has heterogeneous properties, and electrochemical processes at solid electrodes start first at high-energy sites, called active centers or growth sites. Consequently, the current density is initially highly non-uniform, and its distribution tends to change during film growth.

1.1.1.4 Equilibrium Potential and Overpotential

When the electrode reaction reaches its thermodynamic equilibrium, no net current flows across the electrode-electrolyte interface. The corresponding potential, i.e., the equilibrium potential, is defined by the well-known Nernst relation:

$$E = E^{\circ} - (RT/nF) \ln \{(a_{\text{products}})/(a_{\text{reactants}})\} \quad (3)$$

To start metal deposition, an external power source must shift the electrode potential beyond its equilibrium value in the cathodic (negative) direction.

This additional driving force needed to start the electrodeposition process is called the overpotential (overvoltage) and is usually indicated by the Greek letter η :

$$\eta = E - E_{eq} \quad (4)$$

In real-world applications, the overpotential typically ranges from a few mV up to more than 2 V. The deposit's structure and properties are largely influenced by its value, which also dictates the overall process rate. Relatively high η are generally associated with dense and fine-grained coatings. The overpotential also affects the amount of surface-active components adsorbing at the electrode, having a significant impact on the deposition process and deposit structure.

1.1.2 Electrolytes Used for Electrodeposition

Metal deposition can be made from simple solutions of some salt or other soluble compound containing the metal to be electrodeposited. In practice, electrolytes, i.e., electroplating baths, are complex mixtures containing different compounds, each playing a specific role. Supporting electrolytes like inorganic acids or alkalis are added to increase the bath's electrical conductivity without taking part in electrode processes. Higher conductivity allows a lowering in voltage (and therefore saves energy) and increases the deposit's thickness homogeneity. Buffering agents help in maintaining a stable pH value. Buffering is especially needed when hydrogen evolution occurs because H^+ consumption increases the pH value near the electrode.

Along with these most important components, so-called 'additives' are also widely used in practice. Surfactants, for example, are added to plating baths

to reduce the surface energy of the electrode and facilitate the detachment of hydrogen bubbles from its surface. Adhesion of hydrogen bubbles to the electrode leads to undesirable pitting, that is, macroscopic point defects (pits or pores) at the plated surface. Other process-specific additives have been developed to enhance the deposit's properties: brighteners improve deposits' brightness. Levelers smoothen the surface filling pre-existing scratches or pits.

Additionally, some additives decrease the deposit's internal stresses, activate anode dissolution, increase current efficiency, suppress dendrite formation, etc. The additives usually inhibit the deposition and, thus, increase the overpotential. Their action is based predominantly on adsorption at the electrode surface. Additives' concentration decreases over time due to incorporation by the growing deposit or following decomposition at the cathode. Therefore periodic additions are needed to maintain bath performance.

1.1.3 Operating Parameters in Electrodeposition Processes

Electroplating is a complex process, and many operating variables must be fine-tuned to obtain the desired coating characteristics. The most relevant ones will be described below.

- *Temperature*: is one of the most important parameters. Depending on the metal to be electrodeposited and the bath's formulation, it can range from RT up to 80°C. Each process has its optimum operating temperature reported in the bath technical specification. Therefore, it is important to have efficient control of the temperature since

allowances generally do not exceed $\pm 5^{\circ}\text{C}$ from the optimum one. Even though the role of temperature varies significantly from case to case, it is still possible to describe some general trends. Elevated temperatures provide some advantages, improving solubility and electric conductivity.

On the other hand, higher temperature means more power consumption (bath heating represents the main cost item in a plating plant). Moreover, temperature increases evaporation and corrosion processes. Additionally, an increase in temperature hampers additive adsorption reducing its efficacy; consequently, deposits become more coarse-grained. On the other hand, a low temperature requires a drop in current density (and in growth rate) to avoid depositing under diffusion-limited conditions. Lower temperatures slow down diffusion kinetics, often resulting in stressed deposits more prone to embrittlement. Temperature also influences rate processes; typically, a temperature increase by 1°C results in a 10% increase in the rate of electrochemical processes and an enhancement in the rate of mass transfer by 2%.

- *Substrate material and surface finishing* greatly influence the initial plating stages. The nucleation rate on the substrate differs from that on the freshly plated deposit. In some cases, especially when the substrate is free of oxides and with a crystal structure similar to that of the deposit, the substrate influence may propagate up to a thickness of about $10\ \mu\text{m}$. Therefore, a smooth, mechanically polished substrate is required to reduce the surface's detrimental

effect on film growth. The nature of the substrate also determines the type of surface treatment (cleaning, degreasing, chemical or electrochemical etching) necessary to remove surface oxides and contaminants to ensure good adhesion.

- Also, the concentration of electroactive species affects the deposition process and, therefore the deposit properties. More precisely, depositing from dilute solutions results in more fine-grained coatings and lower deposition rate. Also, ions that do not participate in electrode reactions can nevertheless influence the electrodeposition process mainly by adsorbing in the growing films and changing the solution conductivity.
- *Stirring* the electroplating bath is a common practice. It enhances ion transport to the substrate, decreases the thickness of the diffusion layer, and shifts the optimum current density to higher values. Stirring is performed mainly by mechanical stirrers, compressed air bubbling, or eductor nozzles (Venturi agitation). Ultrasound stirring is also effective, but its use is limited due to the high equipment cost. Stirring alone does not have major effects on the coating properties, but adequate agitation is nonetheless required.
- *pH* also plays an essential role because it influences cathode efficiency (related to hydrogen evolution) and hydroxides precipitation. In addition, pH governs bulk electrochemical equilibria affecting the relative concentration of different electroactive species' compounds.

1.1.4 Surface Preparation

The surface preparation is a crucial step in obtaining the required coating characteristics. Prior to being electroplated, substrates undergo various pretreatment processes. These include surface cleaning, surface modification, and rinsing. A schematic flowchart of a typical electroplating plant, including surface treatment and waste treatment, is depicted in Figure 2.

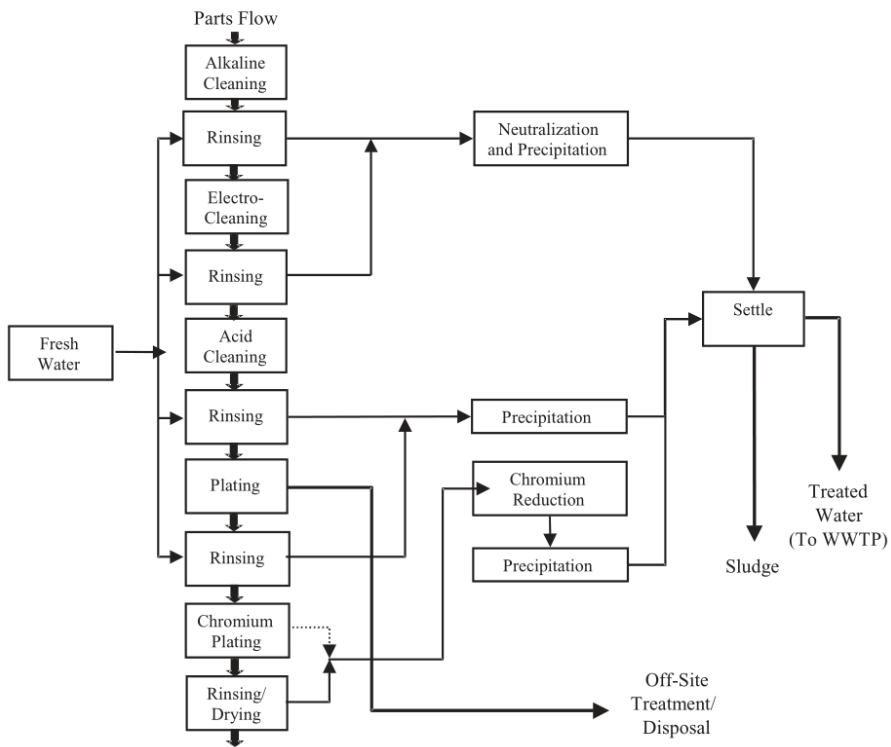


Figure 2 Process flowchart of a typical electroplating processing plant

The purpose of surface pretreatment is to remove contaminants, such as dust and films, from the substrate surface. The surface contamination can be

extrinsic, composed of organic debris and mineral dust from the environment or preceding processes, or intrinsic, such as a native oxide layer. All these contaminations interfering with the substrate-coating bonding could result in poor adhesion or even prevent deposition altogether.

Therefore, surface pretreatment is essential to ensure plating quality. Most surface treatment operations have three basic steps: surface cleaning, surface treatment, and rinsing.

1.1.4.1 Physicochemical cleaning

A physicochemical approach usually includes:

- *Solvent Degreasing.* Contaminants consist of oils and grease of various types, waxes, and miscellaneous organic materials. Suitable organic solvents can remove these impurities from workpieces either by directly dipping in the solvent or by vapor degreasing.
- *Alkaline Cleaning.* Workpieces are immersed in hot alkaline cleaning solutions tanks to remove dirt and solid soil. Alkaline cleaning is often carried out as an electrocleaning method. In this case, the workpiece is the cathode (direct cleaning) or the anode (reverse cleaning) of an electrolytic cell. Electrocleaning adds to the chemical action of the cleaner, the mechanical one caused by gas evolution at the surface of the workpiece.
- *Acid Cleaning.* It removes heavy scale, heat-treat scale, oxide, and the like. The most commonly used acids include sulfuric and hydrochloric.

As for alkaline cleaning, pickling can also be combined with a current to be more effective.

1.1.4.2 Mechanical methods

Mechanical preparations include polishing, buffing, and some variations. Polishing is removing small amounts of metal by employing abrasives. It produces a surface that is free of the larger imperfections left by grinding and is a preliminary to buffing. Buffing is similar to polishing but uses finer abrasives producing an extremely smooth surface.

1.1.4.3 Rinsing

When workpieces are transferred from one treating tank to another, they carry some of the solution in which it has been immersed. This effect is referred to as drag-out. In most cases, this residue solution should be removed from the workpiece's surface by rinsing before the next step. The dirty rinse water will be sent to the wastewater treatment facilities before being discharged to a public sewage system.

1.1.5 Electrodeposition

Electrochemical deposition through direct-current (DC) potential is the most common technique for decorative coatings.

Electrochemical deposition in DC mode is the most common technique for decorative coatings. A rectifier, converting AC current electricity to regulated low-voltage DC current, provides the necessary current. Electrodes immersed in the electroplating bath are connected to the output of a DC current source. The workpieces to be plated act as a negatively charged

cathode, and the positively charged anodes complete the electric circuit. The thickness distribution of the deposited film depends on the shape and contour of the workpieces. As a general rule, coatings are thicker in sharp corners and features and thinner in the recessed ones, reflecting the local current density distribution. Therefore, an appropriate bath design, both in terms of racks and anodes configuration (sizing and placement) as well as current density adjustment, are required to limit thickness inhomogeneities.

Both potentiostatic and galvanostatic modes are used for electroplating. As its name suggests, in galvanostatic mode, power supplies keep the current flowing through the electrolytic cell constant. The potentiostatic mode, on the contrary, is carried out at fixed voltage. During DC plating, the current and the potential must be continuously adjusted to compensate for load changes that could be very high in magnitude, especially in the initial stages of deposition. These variations are chiefly related to (a) surface modifications (roughness, morphology) in the growing film and (b) changes in solution near the cathode (concentration of chemical species, pH).

1.1.6 Electrodeposited coatings defects

Rarely coatings manufacturing is a one-step process. Generally, coatings are multilayered structures in which each layer plays a specific role in achieving the overall properties (improve wear resistance, corrosion resistance, adhesion, appearance, block the diffusion of the underlying metals, etc.). Contrary to what one might expect, the object's outer appearance is not solely determined by the top layer. Because plating consists of consecutive steps, any defects in the production line can affect the final results. Therefore, to obtain the desired coating characteristics, each step of the

manufacturing process must be compliant with well-defined quality requirements. What has been said is especially true in decorative electroplating, as the bright mirror-like plated finish, the most common one, can fall short of perfection in many ways (low defect tolerance). If not, various defects can be noticed. Common defects include roughness, pitting, blistering, high stress and low ductility, discoloration, burning at high current density areas, and failure to meet thickness specifications.

- *Roughness* is usually caused by the incorporation of insoluble particles in the deposit. Insoluble particles may arise from incomplete polishing of the basis metal so that silvers of metal protrude from the surface, incomplete cleaning of the surface so that soil particles remain on the surface, detached flakes of deposit from improperly cleaned racks, dust carried into the tank from metal-polishing operations and other activities, insoluble salts, and metallic residues from the anode material. Good housekeeping and regular inspection and control prevent roughness from incomplete polishing, cleaning, and inadequate rack maintenance. Roughness caused by dust can be controlled by isolating surface preparation and metal-polishing operations from the plating area, by supplying clean air, and by removing dirt from areas near and above the tanks. Roughness caused by the precipitation of calcium sulfate can be avoided by using demineralized water. Continuous filtration of the plating solution can also reduce roughness problems. In this regard, if soluble anodes are used, it is advisable to use suitable bags (anode bags) to retain their residues.

- *Pitting* is caused by many factors, including air or hydrogen bubbles adhesion to the parts being plated. Pitting from adherent hydrogen bubbles can result from a solution that is chemically out of balance, at too low a pH, or is inadequately agitated. In addition, incorrect racking of complicated components, too low a concentration of wetting or antipitting agents, use of incompatible wetting agents, the presence of organic or inorganic contaminants, incomplete cleaning of the basis material, and incomplete dissolution of organic additives that may form oily globules can all result in pitting. Pitting is avoided by maintaining the composition of the plating solution within specified limits, controlling the pH and temperature, and preventing impurities of all kinds from entering the solution.
- *Blistering* is generally due to poor adhesion due to poor or incorrect surface preparation prior to plating. Blistering may also be related to incomplete removal of grease, dirt, or oxides; formation of metal soaps from polishing compounds; or silica films from cleaning solutions. In the case of zinc-based die castings or aluminum castings, blistering during or immediately after plating may be due to surface porosity and imperfections that trap the plating solution under the coating.
- *High stress and low ductility* usually occur when organic addition agents are out of balance and because of impurities.
- *Discoloration* in low-current-density areas is most likely the consequence of metallic contamination of the plating solution. The effects can be evaluated systematically by plating over a reproducible

range of current densities on a Hull cell cathode. Hull cells are trapezoid in shape. Therefore, the metal of interest can be deposited onto a standard panel over a predictable range of current densities. The current density variation over the panel's face is achieved by placing the panel at a specified angle to the anode.

- *Burning* at high current densities can be caused by applying the full load on the rectifier to the lowest parts on a rack as it is lowered into the tank. This can be controlled by applying a reduced load or ramping the current during immersion of the rack. Burning is sometimes related to the presence of phosphates in solution introduced via contaminated activated carbon. In addition, incorrect levels of organic additives can cause burning.
- *Failure to meet thickness specifications* is most frequently due to the application of too low a current or too short a plating time. This can be avoided by measuring the area of the parts to be plated, then calculating the total current required for a specified current density, and plating for the appropriate time. Obtaining surface area can be troublesome for complex-shaped objects. Another major cause of failure to meet thickness requirements is a non-uniform current distribution leading to a lower deposition rate in low-current-density areas. Poor electrical contact and stray currents can also cause thin deposits. Anode and cathode bars, hooks, and contacts should be kept clean.

1.1.7 Composition, Structure, and Properties of Electrodeposited Coatings

Metal deposition processes occurring in parallel with the process of interest result in the incorporation of impurities in the deposit; when other metals are added purposely, an alloy deposit is formed. Growth of the deposit may also result in incorporating any component present in the near-electrode region of the solution. These processes may be beneficial or harmful to the deposit properties and should be monitored. The incorporation rate of adsorbed species is proportional to their coverage and depends on the surface residence time of said species. This incorporation mechanism is characteristic of most additives and auxiliary compounds present in the electrolyte. Hydrogenation is also a co-deposition process that can bring with it many issues, one above all, the so-called hydrogen embrittlement.

The structure of the deposit is characterized first of all by its grain size and shape. The size of crystal grains is obtained by X-ray diffraction analysis. On the other hand, crystallites are often grouped and unlikely can be resolved even by electron microscopy techniques. Transmission electron microscopy can characterize other defects, such as point defects, twins and stacking faults. The use of X-ray diffraction methods can determine the crystallographic orientation of deposits.

In addition, metallographic studies reveal morphological features such as columnar or layered crystal growth and distinctive deposits consisting of non-oriented, randomly packed small grains. Surface morphology can also be examined by scanning electron microscopy (SEM), enabling the observation of various features such as pyramidal, stepwise or spheroid types of surface

shapes which can sometimes be related to the interior structure of the deposit. When studying the substrate influence on deposit structure, it is common to specify whether epitaxial growth is exhibited and the maximum deposit thickness to which it may propagate. Above this thickness, the deposit structure is usually entirely determined by the deposition conditions and not by the substrate.

When deposits are in the form of alloy, determining their phase composition is another essential step in characterization; it is necessary to determine whether the deposit is a solid solution, a mechanical mixture of crystals, or an intermetallic compound. These data are then compared with the thermodynamic phase diagram of the alloy with the same chemical composition. As a rule, the phase composition of electrodeposited alloys may differ from that of the equilibrium state (for instance, of the annealed metallurgical alloy). The formation of a supersaturated solid solution, for example, is often observed.

Of special interest is the structure of deposits with a bright surface; in most cases, bright deposits are observed when the grain size is much smaller than the wavelength of visible light. One further problem that can be tackled with structural studies is defining the degree of porosity and its source, determining if it arises from the substrate or is related to the plating process.

Metal purity and structure depend on several factors, which also affect the physical characteristics of the deposits. This concerns both mechanical (strength, ductility, hardness, adhesion to substrate) and electrical (conductivity, contact resistance) properties, and in the case of iron group metals also, their magnetic properties. Variations in deposit properties are partly due to microstructure changes, particularly at grain boundaries, such

as the segregation of impurities and their structure (e.g., dislocations density or disorientation angle). High internal stress is one of the peculiarities of electrodeposited metals and alloys. Electrodeposits with high tensile stresses, such as chromium and nickel, often show a net of cracks on their surface (Figure 3).

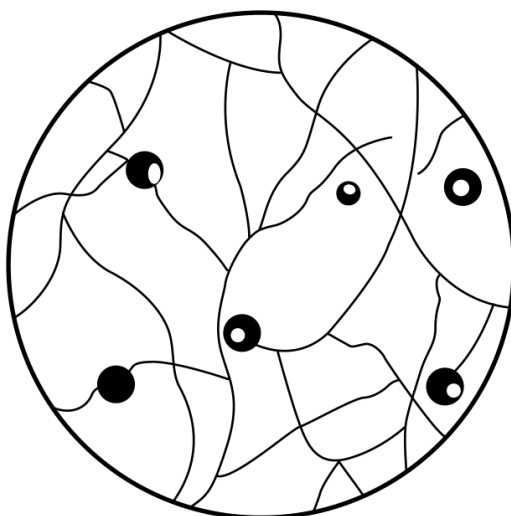


Figure 3 Scheme of nickel deposits cracking. The lines show the cracks, the rounds are the pits generated by hydrogen bubbles

1.2 Physical Vapor Deposition (PVD)

1.2.1 Introduction

Physical vapor deposition (PVD) encompasses a wide range of vapor-phase technologies. It is a general term used to describe various methods to produce (thin) solid films by condensing a vaporized form of the solid precursors onto various surfaces. All PVD processes are essentially based on three stages: (1) evaporation of the solid source, (2) vapor phase transport from the source to the substrates, and (3) vapor condensation on the substrates. The vapor-phase material can consist of ions or plasma and is often chemically reacted with gases introduced into the vapor, called reactive deposition, to form new compounds.

Generically, according to the energy source used in vaporizing the material to be deposited, PVD processes can be divided into three main categories:

1. *Evaporation*: vaporization is induced by the thermal heating of a solid (sublimation) or liquid (evaporation). How thermal energy is delivered can further differentiate deposition methods. For example, heating with a resistive wire is the most straightforward approach, but delivering more tightly focused energy is possible using an electron beam. These are known as resistive evaporation and electron beam evaporation, respectively, as shown in Figure 4.
2. *Sputtering*: is a non-thermal process in which atoms are extracted from the target by momentum and energy transfer with colliding particles.

3. *Arc discharge*: the cathode material is vaporized by a supersonic stream of fully ionized plasma, i.e., an electric arc.

PVD is often associated with “thin film” because most early applications did not rely on the mechanical properties of the deposited material; they relied on the optical and electrical properties of thin deposits. However, over the past decades, vacuum-deposited coatings have been increasingly used for mechanical, electrical, tribological, and corrosion performance improvements, for which thicker deposits are required. Machining tools are probably, one of the most common applications of this deposition technique, sometimes used together with Chemical Vapour Deposition (CVD) in order to increase their lifespan, decreasing the friction and improving the thermal properties.

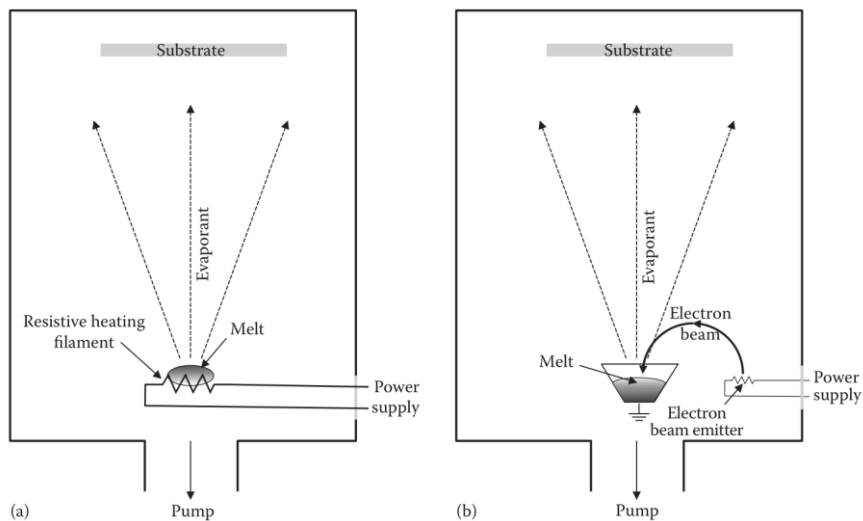


Figure 4 (a) Resistively heated evaporation and (b) electron-beam-heated evaporation.

1.2.2 Thermal Evaporation

Thermal evaporation is conceptually very simple. It basically comprises evaporating source materials in a vacuum chamber below $1 \text{ e-}04 \text{ Pa}$ and condensing the evaporated atoms on a substrate. The temperature of a material is raised until it evaporates at a sufficiently high rate to produce deposition on adjacent surfaces. The temperature could be just a few hundred degrees in the case of volatile metals like indium or zinc or several thousand degrees in the case of metals like molybdenum or platinum.

1.2.2.1 Resistance Heating Method

The most common way of heating materials that vaporize below about 1500°C is by contact with a hot surface that is heated by passing a current through a material (resistively heated). The source materials (generally pelleted or even more finely divided to have a high surface area) can be placed directly on a refractory metal (tungsten, molybdenum, or tantalum) boat-like shaped resistance or in a ceramic crucible (quartz, graphite, alumina, beryllia, boron-nitride, and zirconia) enveloped by a refractory metal resistance (wire basket). Then, a large DC current is flowed through the tungsten boat to raise its temperature. The reason for tungsten or molybdenum is their high melting temperature and low vapor pressure so that they would not deform or evaporate. However, due to their low resistance, a considerable current has to be supplied to create the required heating power.

The main issue of resistance heating methods is related to the temperature profile that decreases in the following order: heating filament, the bulk of the evaporating species, and evaporating surface. Therefore evaporating

surface, which is what matters in the process, is the lowest in temperature. As a result, the process often runs too “hot,” creating outgassing and evaporation of unwanted species in the chamber. Nevertheless, because of its easiness, this method is widely used in producing thin films.

1.2.2.2 Electron Beam Evaporation

Refractory materials (ceramics, glasses, carbon, and refractory metals) cannot be evaporated at a reasonable rate by resistive heating. For such materials, the so-called “e-beams method” is needed. In e-beam heating, a hot tungsten filament generates a cloud of free electrons, like in an incandescent light bulb. The filament is held at a strong negative potential of about -10 kV in magnitude. Electrons, thus, are accelerated away from the filament. Several beam-forming plates near the filament redirect the electrons up and away from the filament, and a set of permanent magnets and electromagnets deflect the electron beam and focus them toward the center of the crucible. The electromagnets can make small adjustments or sweep the e-beam spot across a larger surface area. The background pressure in the chamber needs to be low enough to produce a sufficiently long mean-free path for these electrons to travel from the filament to the crucible without collisions. The energy is ultimately delivered to the evaporating surface by the bombardment of high-energy electrons.

E-beam heating is more expensive to install and operate than resistive heating. It requires a high-voltage DC source, separate filament and beam current control circuits, and the associated safety issues due to the high voltage. Special precautions must also be made inside the chamber to prevent charge build-ups and arcing. However, for applications where

material purity is essential, e-beam is often the best choice. What makes e-beam heating particularly useful is the high-power density that can be delivered at the evaporating surface. Electron beams can be focused down to a tiny spot, achieving very high melt temperatures at relatively low beam powers, i.e., the evaporation process is more efficient.

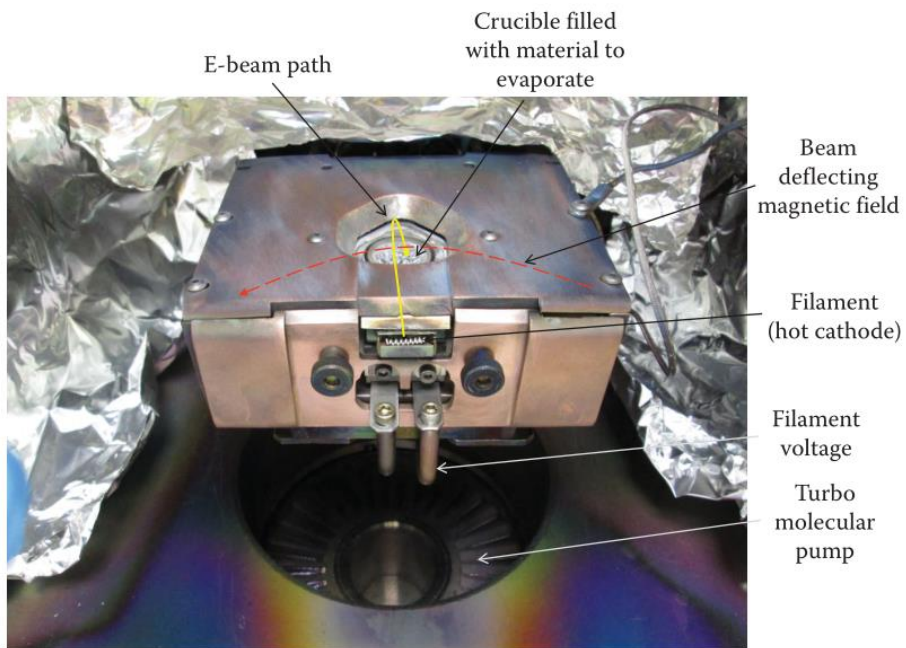


Figure 5 An electron-beam-heated evaporation assembly

1.2.2.3 Molecular Beam Epitaxy

Molecular beam epitaxy (MBE) is a PVD technique carried out under ultra-high vacuum (UHV, better than 10^{-9} mbar) where epitaxial deposition of thin film crystal on crystalline substrates can be obtained by using one or more vapor sources (effusion cells or sometimes called Knudsen cells). An effusion cell consists of a crucible (made of graphite, pyrolytic boron nitride,

quartz, or tungsten) where the solid source can be heated and evaporated by hot filaments (Figure 6).

The major advantage of MBE comes from its controllable deposition rate at the atomic or molecular scale. This can be achieved due to the use of effusion cells that enable the generation of a “molecular beam,” where the generated vapors have low interparticle collisions before reaching the substrate surface. Therefore, evaporated atoms escape from the orifice of the cells through effusion and have a long mean free path. As a result, they neither interact with each other nor with the gases in the vacuum chamber. Due to this capability, MBE was recently used for the growth of graphene, but the outcome is debatable. MBE is an advanced thermal evaporation technique with highly controllable deposition thickness (and thus with the drawback of slow deposition rate) thanks to effusion cells and high vacuum. However, if no specific requirements in the crystal structure are needed, there are no valid reasons to use such a complex method. By resistive evaporation (amorphous), thin films can also be obtained with a much simpler setup.

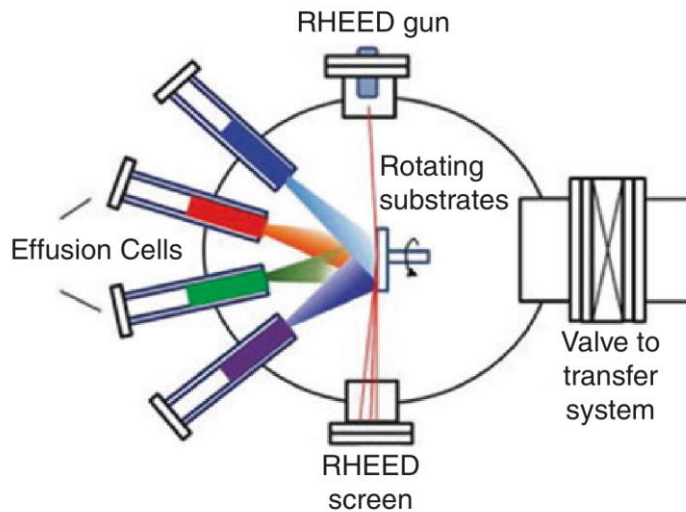


Figure 6 Schematic drawing of a typical molecular beam epitaxy system.

1.2.2.4 Pulsed Laser Deposition

Pulsed laser deposition (PLD) is a physical vapor deposition (PVD) process that employs a high-power pulsed laser to produce vapors (i.e., laser ablation) from a solid target, followed by condensation on substrates. Compared to many PVD techniques, the experimental setup for PLD is relatively straightforward, even though the laser ablation working principle is quite sophisticated. A PLD system consists of a pulsed laser, a vacuum chamber with a spinning target holder, and a substrate holder with a heater, as seen in Figure 7. PLD can be conducted at different substrate temperatures in a vacuum. During film deposition, laser pulses are focused on the target through a chamber's viewport using a tiny lens, producing a laser spot with very high irradiance (I , power per unit area) and a local electric field:

$$I = \frac{1}{2} \epsilon_0 c E_0^2 \quad (5)$$

Where:

- E_0 is the laser's electric field amplitude, c is the speed of light in vacuum.
- ϵ_0 is the vacuum permittivity.

The local electric field is sufficient to cause atomic bond breaking and dielectric breakdown of the target materials to initiate vaporization of the target materials. This vapor will absorb the remaining portion of the laser pulse, and the electric field of the pulse itself will accelerate electrons and ions inside the vapor to create rapid heating and form laser plasma. Continued laser pulse absorption will cause a highly directional expansion of the laser plasma perpendicular to the target surface. This expanding vapor, i.e., the laser plume, propagates toward the substrate placed several centimeters opposite to the target.

PLD can be conducted in vacuum or in a low-pressured gas ambient. When PLD is conducted in reactive gas ambient (e.g., oxygen or nitrogen), the technique is called reactive PLD. In this case, the expanding laser plume will form shock waves, inducing a chemical reaction between the target vapor and the gas molecules. PLD can also be modified into various configurations. Among these, one of the most interesting is the so-called plasma-enhanced or plasma-assisted PLD (PE-PLD), in which plasma is applied to enhance the interaction of the vapors with the working gas. In addition, the integration of ion beams is also implemented. In this variation, called ion beam-assisted

PLD, an auxiliary ion beam is irradiated on the surface of the substrates during thin film deposition (Figure 7).

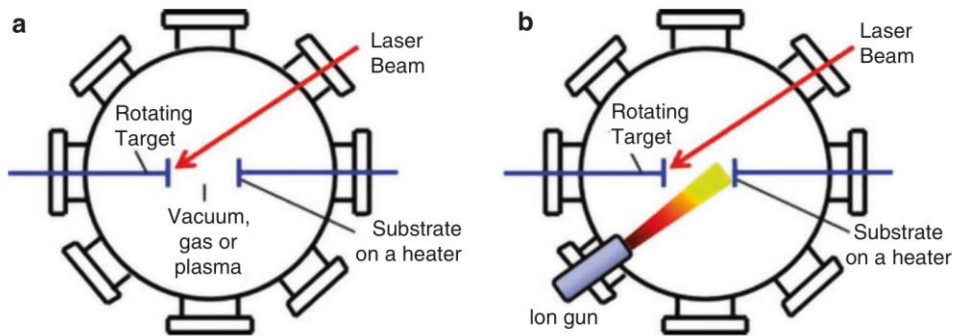


Figure 7 Schematic drawings of a typical pulsed laser deposition (PLD) system operated (a) in vacuum or with auxiliary plasma or (b) with auxiliary ion beam

In general, the quality of PLD-deposited coatings strongly depends on the laser ablation mechanism and, therefore, on the pulsed laser wavelength and energy. If the target ablation threshold is too low (ablation threshold is the minimum energy density required for laser removal of a given material), it is likely to incur unwanted plasma heating. Plasma will be created at a high temperature, i.e., a large amount of laser energy is available to heat the plasma after ablation. It also means that even though you can ablate more material with a higher irradiance, the plasma that is formed will have a higher temperature. As a result, the deposition behavior change, complicating the control of the process. Plasma heating will lead to the so-called photothermal ablation. For example, photothermal ablation of the hexagonal-BN target will transfer the hexagonal-BN target to the substrates and prevent the formation of cubic phase (c-BN). Photothermal ablation of graphite target at longer laser wavelength will also prevent the formation of diamond-like carbon film (DLC) as the sp^2 species from the graphite are transferred to the

substrates. Plasma heating can be avoided by keeping the laser energy or irradiance low. As a general rule, shorter wavelengths reduce the chances of such a plasma heating effect.

1.2.3 *Sputtering*

1.2.3.1 Introduction

Sputtering is a process where atoms are released from a solid target material due to the bombardment of energetic particles (i.e., ions and atoms). By PVD sputtering, coatings ranging from nanometers to micrometers in thickness can be obtained on virtually any substrate materials. The physics driving the process is the collisional transfer of momentum from the incident ions/atoms to the target materials. Sputter removal can be considered a sublimation process since the material is instantly transformed into a vapor without melting. It can also be considered a “cold” evaporation process since energy is transferred via exterior projectiles instead of internal phonons (heat).

Sputter yield refers to the average number of atoms ejected from the target per impinging particle. Yield depends on the ion’s incident angle, the ion’s energy, the masses of the ion and target atoms, the surface binding energy of target atoms, and the crystallographic orientation of the target when crystalline materials are employed as targets. Different methods for generating sputter are used, such as using DC, AC, and RF plasmas or external ion beams. Sputtering has many advantages over conventional PVD processes, including (1) greater deposition area compared to PLD, (2) convenience for thin film deposition of alloy/composite and materials with

high melting temperatures, and (3) prevention of device damage from X-rays produced by electron beam evaporation. However, sputtering has the following disadvantages: (1) a more complicated setup than PLD, (2) a higher chance of contamination due to the use of plasma as well as a relatively lower vacuum level, and (3) a film morphology that may be rougher and even damaged due to the bombardment of energetic growth species and clustering of growth species in the relatively high deposition pressures.

PVD can be obtained by applying plasma in various configurations. The simplest one is a DC diode-like system; a DC potential is applied across the substrate (anode) and target (cathode), with an inert plasma forming gas (e.g., argon) in between. In the DC diode glow discharge, the electric field strength is high near the cathode, and most of the applied voltage is dropped across a region near the surface called the cathode dark space. This region is the primary region of ionization. The rest of the space between the cathode and anode, which is often grounded, is filled with a plasma where there is little potential gradient. In the cathode dark space region, ions are accelerated from the plasma to impinge on the target surface with high kinetic energy. This ion bombardment causes the ejection of secondary electrons, which are accelerated away from the cathode, causing additional ionization and atomic excitation by electron-atom collision, so the ionization appears as an avalanche process. At equilibrium enough electrons are created to cause enough ions to create the electron flux needed for plasma sustainment.

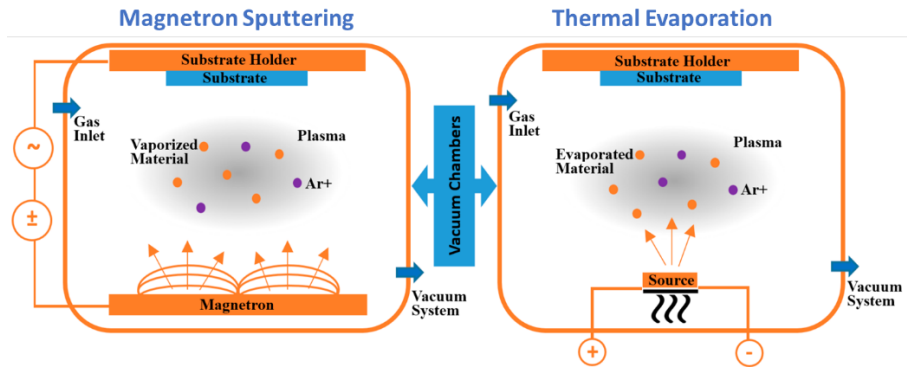


Figure 8 Schematic diagram representing Sputtering (Magnetron) and Thermal Evaporation

Despite its simplicity, the DC configuration will have the following issues: (1) positive charges will build up on the target surface and cause sparking within the plasma, and (2) it is unsuitable for insulating targets. AC and RF configurations allow overcoming these issues. In these cases, the potential between the target and substrate is alternating, so the target will be negative in potential more often (to generate sputtering) than positive potential. These configurations also allow lower operation pressure (~10–30 mTorr). However, other major limitations remain unsolved, such as substrate surface heating (due to the acceleration of electrons away from the target) and, most importantly, the low sputtering rate. Therefore, since most materials suitable for DC diode sputtering (i.e., relatively unreactive metals such as gold, copper, and silver) can also be deposited by thermal evaporation, this type of DC sputter deposition has not been widely used.

1.2.3.2 Magnetron Sputtering

A renewed interest in sputtering techniques has emerged relating to developing magnetron devices that increase ionization - thus, it is possible to operate at much lower pressures than a simple cathode plate - and sputtering rate, resulting in higher coating quality.

Magnetron sputtering configurations use a magnetic field (~200 Gauss), usually from permanent magnets near the target (cathode) surface, to confine the electrons near the surface, enhance the deposition rate at even lower pressures by the use of DC, AC, or RF electric fields.

1.2.3.2.1 Direct Current (DC) Magnetron Sputtering

When an electron is ejected from the target surface, it is accelerated away from the surface by the electric field, but it is forced to spiral around the magnetic field lines. The $E \times B$ force also causes the electron to move perpendicularly to the $E \times B$ plane. If the magnetic field is arranged appropriately, the electrons will form a closed-path circulating current near the surface. This closed circulating path can be easily produced on a planar surface or any surface of revolution, such as a cylinder, cone, hemisphere, etc.

The placement of two magnets on a circular (planar) magnetron cathode is shown in Figure 9. Magnets configuration creates a radially symmetric magnetic field on the target surface.

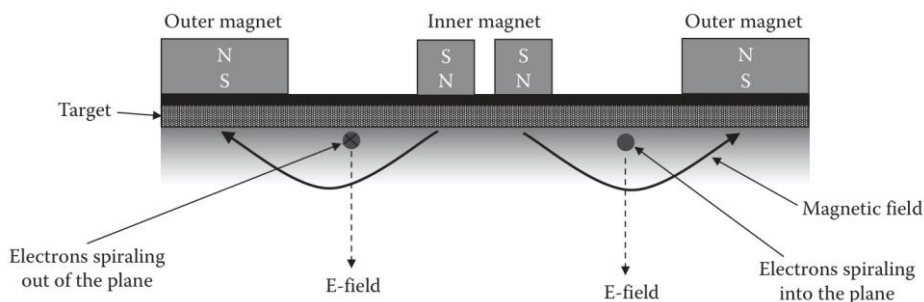


Figure 9 Circular magnetron cathode with two concentric magnets. As indicated in the figure, the electrons will move in a spiraling path away from the cathode instead of moving parallel to the E-field.

Between the two magnets where the magnetic field is parallel to the cathode plate, the plasma density will be significantly increased, resulting in a corresponding increased sputter rate in those areas, hence the major problem of this technique. The non-uniform target erosion (see the characteristic “racetrack” in figure 10) results in a more directional material flux. As a result, the deposition pattern is non-uniform as well, and substrate movement is needed to reduce the thickness spread of the coating. Moreover, uneven erosion reduces target utilization (typically not exceeding 20-40%) and can be troublesome in production environments due to its economic consequence.

Ferromagnetic targets such as iron and nickel do not work well with magnetron cathodes because the magnetic field is impeded in passing through the target. However, deposition of these materials is still possible by using a target of reduced thickness and stronger magnets.

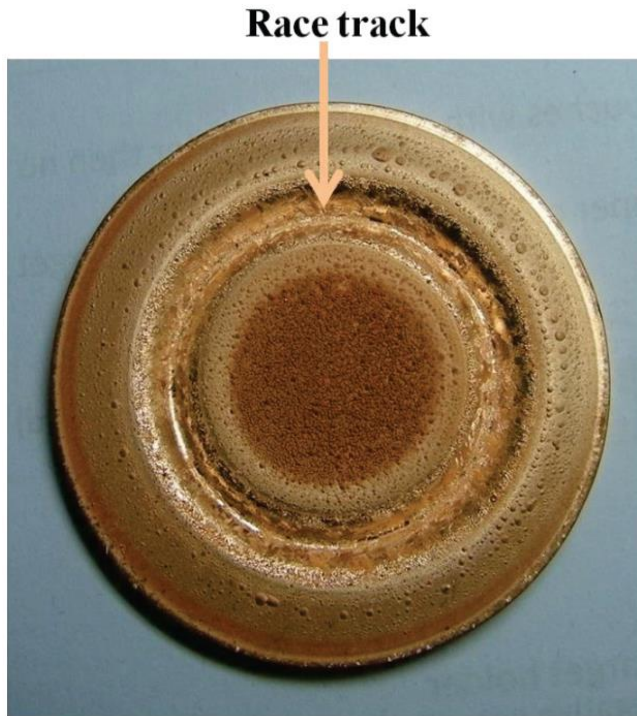


Figure 10 Copper target showing evident signs of racetrack-like erosion

1.2.3.2.2 Radio Frequency (RF) Magnetron Sputtering

Direct current (DC) sputtering is a cost-effective method for thin layer deposition of electrically conductive metallic targets. However, this method does not apply to non-conductive dielectric target materials. This is because ions impinging on an insulating target remain trapped on the surface, repelling further incoming bombarding ions. This results in the cessation of the sputtering process and arcing into the plasma.

In order to overcome DC sputtering shortcomings, RF sputtering is widely used for electrically non-conductive target materials deposition.

In RF sputtering, the polarity of electrodes is inverted at a given frequency. Discharging an insulating target requires frequencies above 1 MHz; 13.56

MHz is an established standard to avoid electromagnetic interference (EMI). As can be seen in figure 11, electrons reaching the target in the positive half-cycle neutralize the positive ions collected on the target surface; in the other half-cycle, atoms are sputtered away from the target surface by positive ions and reach the substrate forming a layer.

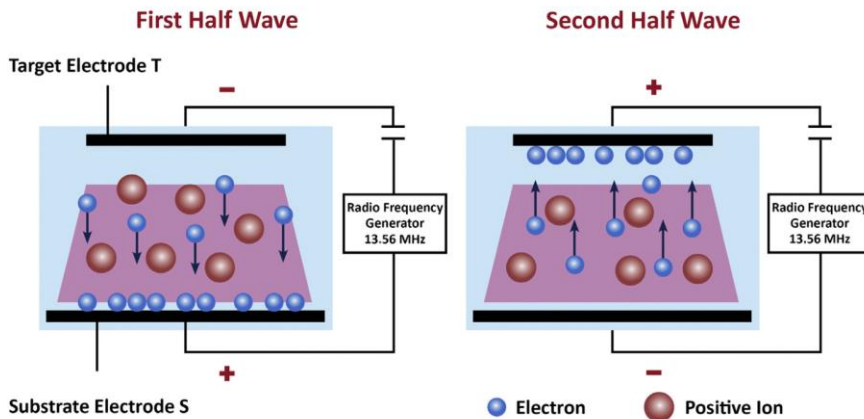


Figure 11 Operating principle of RF sputtering

Since the target is capacitively coupled to the plasma, RF sputtering can be used to deposit conductive or non-conductive materials. However, RF sputtering is scarcely used in metallic coatings manufacturing processes because of its higher equipment costs and lower deposition rate. Instead, RF diode sputtering is most commonly used for sputtering insulating materials such as oxides (silicon dioxide, titanium dioxide, aluminum oxide, etc.) and for sputtering polymers. In this regard, it must be taken into account that most electrically insulating materials have poor thermal conductivity and are usually brittle. Since most of the bombarding energy produces heat, not efficient heat dissipation may result in target fracturing. Therefore it is

necessary to operate at low power levels, which further reduces deposition rates.

1.2.3.2.3 Reactive Sputter Deposition

An elemental target can be sputtered with a mixture of argon and another reactive gas (such as oxygen or nitrogen) to create compounds. This is a distinguishing feature of reactive (magnetron) sputtering and a major advantage over other deposition techniques because it allows obtaining coatings (e.g., ceramics, dielectrics, hard coatings, etc.) with unique properties from both functional and aesthetical points of view. Moreover, sputtering a metallic target to produce a ceramic or dielectric film has several attractive qualities; dielectrics generally have very low sputter yields and poor thermal conductivity compared to metals, characteristics associated, respectively, with low deposition rate and higher chances of target cracking. In addition, metallic targets can be sputtered with a simpler and less expensive DC apparatus instead of RF and are easier to obtain in greater purity and at a lower cost than dielectric ones.

Typically, reactive sputtering is affected by the so-called “poisoning effect,” which is the formation of a compound layer on the target’s surface. Poisoning significantly reduces the sputtering rate and its efficiency. However, this problem can be limited by operating at high sputtering regimes in appropriate sputtering configuration (dual cathode, pulse power, etc.) and by a fine adjustment in reactive gas feeding; such that there will be enough reactive species to react with the film surface to deposit the desired compound, but not so much that it will unduly poison the target surface.

Among the several coatings that can be obtained by reactive sputtering, refractory metal nitride is one of the most noteworthy. Compounds like TiN, ZrN, TaN, and HfN have wide ranges of decorative, as well as tribological, applications. Titanium nitride (TiN) has the reflective properties of gold and has decorative, tribological, and optical applications. TiN coatings give jewelry a gold color and protect it from corrosion and wear. Tantalum nitride (TiN) and zirconium nitride (ZrN) have reflective properties of silver and brass.

1.2.3.2.4 Ion Beam Sputtering

Ion beam sputtering (IBS) is a PVD technique in which the target is evaporated by an external ion source (ion beam). In a typical ion source, ions are generated by collisions of neutral gas atoms/molecules with electrons. The electric field then accelerates them by a grid electrode toward the target. Before ions leave the source, they are neutralized by electrons from a second external filament. The major advantage of PVD by IBS is that the energy and flux of ions can be controlled independently. In addition, the IBS approach applies to insulating and conducting targets since the flux of ions (which are neutralized as they are emitted from the ion beam) that strikes the target is composed of neutral atoms/molecules.

1.2.4 Arc Discharge

In the arc discharge process, a low-voltage high-current DC arc in a low-pressure gaseous atmosphere is used to vaporize material from an anode or a cathode. In cathodic arc vaporization, which is the most common PVD arc vaporization process, a high-voltage “trigger arc” will be ignited between the

cathode and a sharp auxiliary anode. The high current density arc gives rise to a small (a few micrometers wide), highly energetic emitting area on the cathode surface known as a “cathode spot.” The localized temperature at the cathode spot is exceptionally high (around 15000 °C), which results in a high velocity (10 km/s) jet of vapourised cathode material, leaving a crater behind on the cathode surface. The cathode spot is only active for a short time, then it self-extinguishes and re-ignites in a new area. The arc movement may be random or “steered” using a magnetic field. In many cathodic arc vapor deposition systems, multiple cathodic arc sources are used to allow depositing over large areas.

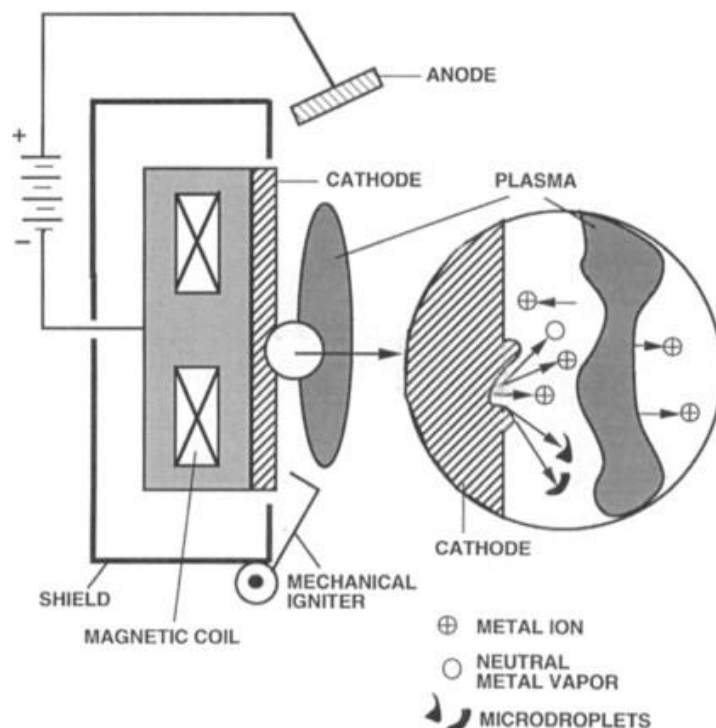


Figure 12 Schematic diagram of cathodic-arc deposition system with a model of activity at a cathode spot.

One of the main advantages of arc discharge over sputtering is the higher deposition rate and the low operation voltage. On the other hand, if the cathode spot stays at an evaporative point for too long, many macro-particles or droplets can be ejected. These droplets are detrimental to the performance of the coating as they are poorly adhered and can extend through the coating. Worse still, if the cathode target material has a low melting point, such as aluminum, the cathode spot can evaporate through the target resulting in either the target backing plate material being evaporated or cooling water entering the chamber. Therefore, as previously mentioned, magnetic fields control the arc's motion. If cylindrical cathodes are used, the cathodes can also be rotated during deposition. By not allowing the cathode spot to remain in one position too long, aluminum targets can be used, reducing the number of droplets. Some companies also use filtered arcs that use magnetic fields to separate the droplets from the coating flux.



Figure 13 Aluminium Titanium Nitride (AlTiN) coated endmills using Cathodic arc deposition technique

1.2.5 Common features of PVD processes

Below are reported some distinctive features of PVD processes as a whole, listed as pros and cons.

1.2.5.1 Advantages

- Line-of-sight deposition allows the use of masks to define areas of deposition.
- Vaporization source material can be in many forms, such as chunks, powder, wire, chips, etc.
- Since deposition is carried out in a vacuum environment, contaminations are limited; therefore, starting from high-purity materials, coatings of corresponding purity can be easily obtained.

1.2.5.2 Disadvantages

- Line-of-sight material flux can be troublesome in covering complex-shaped workpieces. To avoid poor surface coverage, elaborate tooling and fixturing are often needed, and, despite all efforts, it is sometimes impossible avoiding shadow effects.
- Poor utilization of vaporized material. Ejected atoms/molecules have poor directionality causing the spreading of depositing materials over the chamber. In some cases (i.e., magnetron sputtering) can be even worse because of unevenness in target consumption.
- Film properties are strictly dependent on operating parameters, and the effects of their variations are often unpredictable. Therefore,

obtaining the required properties can be a time-consuming trial-and-error process.

1.3 Metallic coating characterization

1.3.1 Corrosion

1.3.1.1 Introduction

Corrosion can be defined as the deterioration of a material's properties due to its interaction with its environment.

More precisely, as per ISO 8044:2015, corrosion is a “Physicochemical interaction between a metal and its environment that results in changes in the properties of the metal, and which may lead to significant impairment of the function of the metal, the environment, or the technical system, of which these form a part.”

Metal corrosion pervades many aspects of everyday life as industry, safety, and technology, just to name a few, with a huge economic impact. For example, it is reported that the cost of metal corrosion in the USA was approximately \$ 170 billion in 2012, which raised to \$ 2.5 trillion in 2016, equivalent to 16 times the economic loss caused by natural disasters. Roughly speaking, losses caused by steel corrosion could account for 3% ~ 4% of the global gross domestic product (GDP).

1.3.1.2 Forms of Corrosion

Corrosion can be divided into two distinct types: generalized and localized. As the name suggests, generalized corrosion proceeds uniformly over the entire surface of an asset in contact with liquid (chemical solution, liquid metal), gaseous (air, CO₂, SO₂⁻, etc.), or hybrid electrolytes. Atmospheric,

triggered by moisture, and galvanic, occurring when dissimilar metals are in contact, are the most noteworthy forms of generalized corrosion.

Conversely, localized corrosion involves specific sites. It is the more insidious form of corrosion because it usually originates in not visible areas, so objects could be already compromised when signs of degradation become detectable. The two most important forms of localized corrosion are:

1. *Pitting corrosion*: is a highly localized form of corrosion that manifests as holes on a metal surface. Cavities known as pits appear at anodic sites due to an electrochemical dissolution process. In a water-based electrolyte containing chlorine Cl^- ions and oxygen molecules, the formers migrate toward the bottom of the pits, while the latter react with water molecules on the metal surface. Therefore, metal chloride $\text{M}^{z+} \text{Cl}^-$ and hydroxyl ions OH^- are produced (see figure 14). This form of corrosion can be found on aluminum and its alloys as well as chromium-plated and painted items due to protective coating breakdown at isolated surface sites.

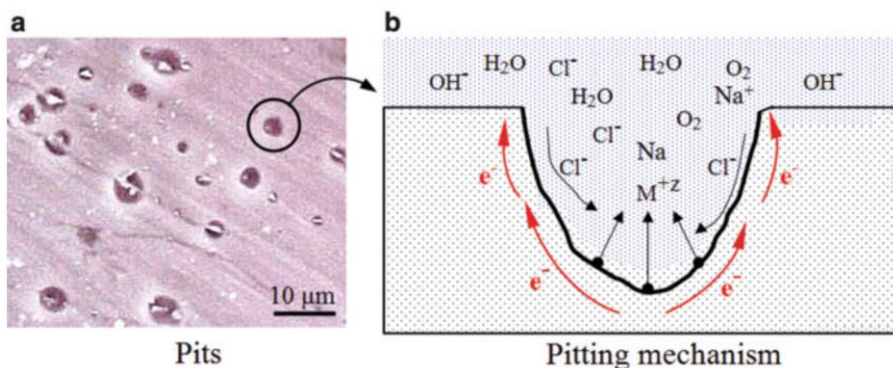


Figure 14 Illustration of localized corrosion mechanism in an Al-Li alloy.

2. *Crevice corrosion*: is associated with a stagnant electrolyte such as dirt, corrosion product, sand, etc. It occurs on metal/alloy surface holes, underneath a gasket, lap joints, under bolts, and rivet heads. In crevice corrosion, local anode surface areas change local chemistry (depletion of oxygen, build-up of aggressive chloride ionic content, etc.), resulting in irregular or pit-like cavities formation. It is often difficult to observe because of the small diameters of the pits and because they are often covered with corrosion products. Two types of pitting corrosion can be distinguished, namely (a) pitting caused by halides (generally chloride pitting of stainless steel) and (b) pitting of carbon steel caused by oxygen attack.

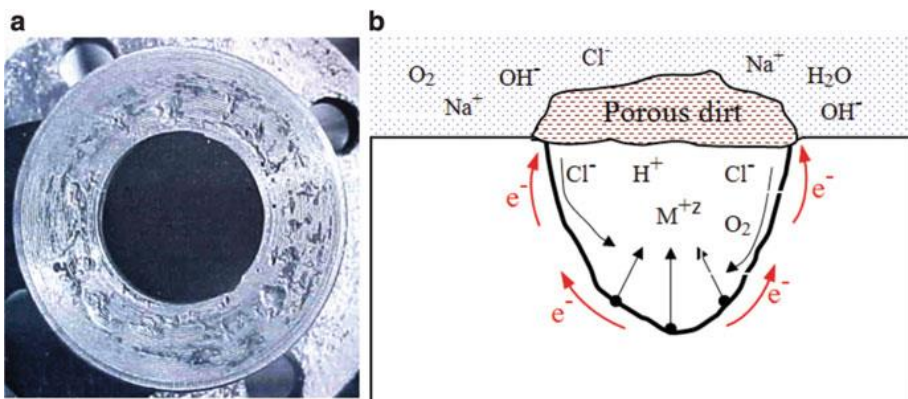


Figure 15 (a) Stainless steel flange exhibiting crevice corrosion-related deterioration signs. (b) Crevice corrosion mechanism.

3. *Galvanic corrosion*: refers to corrosion damage induced when two dissimilar materials are coupled in a corrosive electrolyte. For example, it occurs when two (or more) dissimilar metals are brought into electrical contact under water. When a galvanic couple forms, one of the metals in the couple becomes the anode and corrodes

faster than it would all by itself, while the other becomes the cathode and corrodes slower than it would alone. Either metal in the couple may corrode when in seawater.



Figure 16 Galvanic corrosion of a (a) steel alloy chain and (b) carbon steel bolt-nut coupling

4. *Intergranular corrosion*: is a form of corrosion affecting metal's grain boundaries. Under certain conditions, small areas at grain boundaries can become more anodic than the bulk of the grains, triggering the corrosion process. The corrosion propagates into the metal via the grain boundaries up to causing their disappearance. Therefore, it is commonly associated with a reduction in strength. A well-known example is the occurrence of weld decay in stainless steel, in which the attack arises from welded zones.

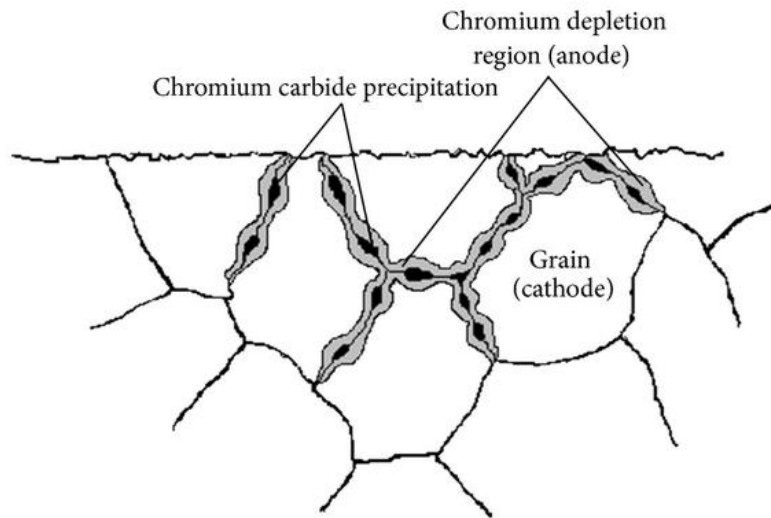


Figure 17 Schematic representation of intergranular corrosion triggered by carbide precipitation at grain boundaries in austenitic stainless steel

5. *Microbiologically induced corrosion*: refers to corrosion caused by biological organisms or microbes. These microbes are categorized by common characteristics such as their by-products (i.e., sludge producing) or compounds they affect (i.e., sulfur-oxidizing). They all fall into one of two groups based on their oxygen requirements: (a) aerobic (requires oxygen), such as sulfur-oxidizing bacteria, and (b) anaerobic (requires little or no oxygen), such as sulfate-reducing bacteria.



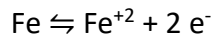
Figure 18 Effects of microbiologically induced corrosion in stainless steel pipe carrying chlorinated potable city water

1.3.1.3 Corrosion Thermodynamics

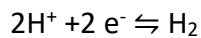
Metallic corrosion is an electrochemical oxidation process in which the metal transfers electrons to its surroundings (which may be a liquid, gas, or hybrid solid-liquid), known as electrolytes due to their inherent conductivity for ionic transport. The oxidation reaction of the metal is referred to as the anodic half-reaction, and the site where oxidation occurs is referred to as the anodes. On the other side, the reduction of electrolyte electrochemically active species is referred to as the cathodic half-reaction, and areas on the metal's surface where it occurs are referred to as cathodes. Anodes and cathodes can be separated by finite distances as long as negative and positive ions move in the electrolyte toward the anodes and cathodes, respectively, to maintain the metal's and electrolyte's electrical charge neutrality. Both

anodic and cathodic reactions must be present to initiate and sustain metallic corrosion.

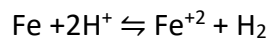
A common oxidation reaction (anodic) in corrosion processes is metal dissolution:



While a typical reduction reaction (cathodic) is hydrogen evolution:



The overall corrosion reaction is a combination of the anodic and cathodic half-reactions:



A complex interfacial layer forms when a metal is submerged in an environment such as water. Water molecules are attracted by the negative charge around metal surface atoms and adsorb on the metal surface. Water adsorption disturbs the balance of the surface atoms, causing some of the metal surface atoms to leave the metal lattice as ions.

A corrosion reaction can proceed in both the forward and reverse directions (i.e., both oxidation and reduction can occur), and equilibrium is achieved when forward and reverse reaction rates are equal. Thus, the metal ions remain close to the metal surface, creating an equilibrium layer known as the electrical double layer (EDL).

Fig. X depicts an example of a layer of water molecules (represented by open circles) adsorbed on the surface of a metal, with hydrated metal ions (represented by encircled Me^{+n}) adjacent to the water layer. The column of minus signs represents the surface metal's valence electrons. The water layer

adsorbed on the metal surface and the water hydration sheath encircling the metal ions prevent them from coming into contact with excess surface electrons, resulting in separated positive and negative charge planes. When an EDL reaches equilibrium, thus, there is no net metal loss.

The charge separation in an EDL produces an electrical potential that can be measured as the difference between two metal electrodes or metal and a reference electrode (an electrode with a fixed and well-known potential).

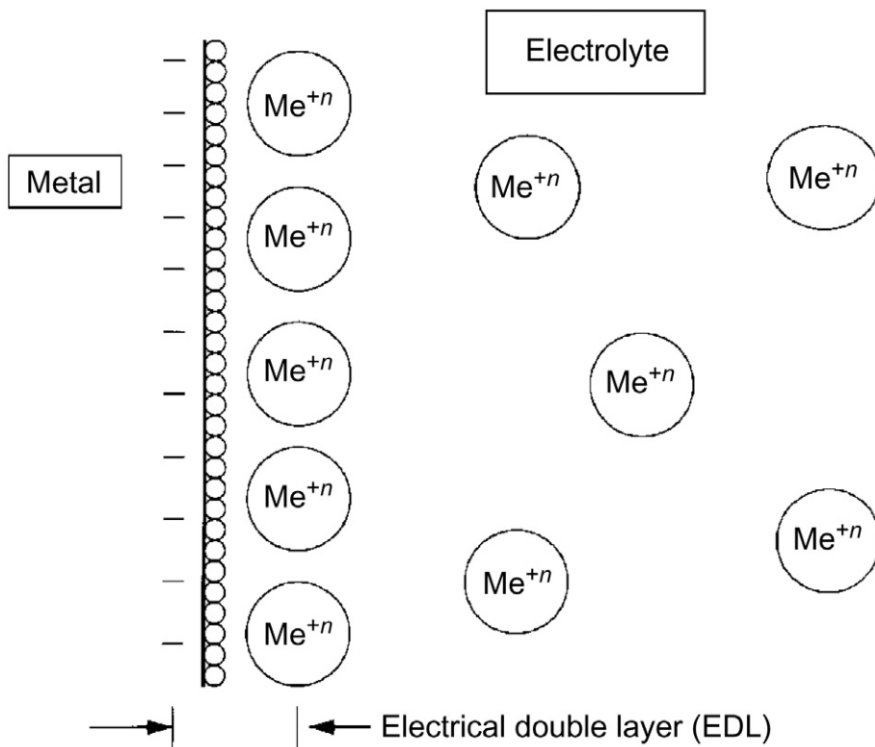


Figure 19 An equilibrium model for the electrical double layer.

The thermodynamic tendency for an electrochemical reaction to occur, such as metal oxidation, is determined by the free energy change associated with that reaction. The Gibbs equation expresses Gibbs free energy as a function of corrosion potential as:

$$\Delta G = - nFE \quad (6)$$

Where:

- ΔG is the Gibbs free energy;
- n is the number of electrons in the anodic corrosion reaction;
- F is Faraday's constant in 96,500 C/equivalent;
- E is the OCP (corrosion).

OCP value is determined by the chemical composition of the EDL, i.e., by the metal and the surroundings. In other words, OCP is not an intrinsic property of metal and changes depending on EDL composition. In addition, an applied voltage will change the composition of the EDL. The mathematical relationship between the EDL composition and the electrical potential is expressed by the well-known Nernst equation:

$$E = E^{\circ} - (RT/nF) \ln \{(a_{\text{products}})/(a_{\text{reactants}})\} \quad (7)$$

Where:

- a is the chemical activity of products and reactants.
- E is the measured potential in volts or millivolts.
- E_o is the OCP when all activities in Eq. 2 is equal to 1
- R is the ideal gas constant which is equal to 1.986 cal/mole K
- T is the temperature in degrees Kelvin (K).
- n is the number of electrons in the anodic half-reaction.
- F is Faraday's constant, equal to 96,500 C/equivalent or 23,060 kcal/V.
- The quantity RT/F is equal to 25.6 mV-equivalents at 298K (25°C).

Eq. 7 shows how the magnitude of a measured potential will vary as a function of the electrolyte's bulk composition, as it determines the EDL.

The Nernst equilibrium potential, i.e., the OCP, is a measure of the electrochemical reaction's thermodynamic tendency to occur, predicting the possibility of corrosion. Specifically, spontaneous corrosion is expected when the OCP has a negative value, and the higher its magnitude, the greater the proneness of the metal to oxidize.

On the other hand, Nernst's potential does not provide any information on the rate at which the corrosion process occurs, which is pivotal because

kinetic limitations, as well as for chemical reactions, can prevent corrosion from occurring.

1.3.1.4 Corrosion Kinetics and Polarization Curves

Electrochemical kinetics (the kinetics of the charge-transfer process) of a corroding metal can be characterized by determining the corrosion current density (i_{corr}) and the corresponding corrosion potential, i.e., the OCP.

Polarization refers to the deviation of the electrode's potential from its equilibrium value (i.e., OCP) due to a driving force causing a current flow. The driving force may derive from electrode reactions, contact with other metals, or, as in polarization experiments, imposed by a potentiostat.

The difference between the actual potential E and the equilibrium value e_{eq} is called overpotential and, therefore, represents the extent to which the electrode solution interface departs from the equilibrium:

$$\eta = E - e_{\text{eq}} \quad (8)$$

Overpotential can be accounted for as the sum of two major contributions, which prevail over the other depending on the current density range:

$$\eta = \eta_{\text{conc}} + \eta_a \quad (9)$$

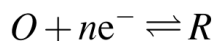
Where:

- η_{conc} , the *activation overpotential* is the driving force required to overcome the activation energy barrier of charge-transfer processes. The electrochemical process is a heterogeneous reaction consisting

of consecutive steps (adsorption of reactant species to the electrode surface, electron transfer at the electrode surface, insertion/exit of metal cations into/from the crystal lattice, etc.) with the slowest one – the rate-determining step (RDS) – controlling the kinetics of the whole electrode reaction, which in corrosion is the rate of electron flow from the metal surface undergoing oxidation. Its contribution to overpotential might be large at low current densities.

- η_a , the *concentration overpotential* reflects the resistance to diffusive transport. As the current density increases, transport becomes more critical due to the increasing magnitude of the concentration gradient between the bulk and cathode's surface, where the electroactive species (e.g., H^+) are fast depleted. At this stage, the reaction rate is controlled by mass transfer through the electrolyte and electrode's surface.

Considering first-order electrode reaction:



The net flux of "O" at the electrode surface (conversion rate of O to R) is the difference between the cathodic and the anodic rates, which, as stated by Faraday's law, is proportional to the net current, I , that passes through the circuit.

At equilibrium, the forward (cathodic) and the reverse (anodic) reaction rate are exactly the same; therefore, there is no net current flow. On the contrary, as the system shifts from its equilibrium potential (Nernst potential), an overpotential develops, resulting in a net current flow.

When mass transport is fast, as in a well-stirred solution, the concentration of electroactive species at the electrode interface can be assumed as in bulk. Therefore, the concentration overpotential can be neglected. In this case, the current, I , flowing to or from an electrode because of an applied potential can be expressed as:

$$i = i_o \left\{ \exp \left[\frac{\alpha z F \eta}{RT} \right]_f - \exp \left[-\frac{(1 - \alpha) z F \eta}{RT} \right]_r \right\} \quad (10)$$

Where:

- η is the overpotential, i.e., the difference between the actual and the equilibrium potential;
- i_o is the exchange current density (A/cm²);
- α is the charge transfer coefficient.

The eq. 10 is the well-known Butler-Volmer (B-V) equation that relates the current density and potential of anodic and cathodic electrode reactions under charge transfer control, providing the most general kinetic description of the electrode reaction under charge transfer control.

It is worth noticing that the B-V equation agrees with the Nernst one for very high-speed kinetics ($i_o \rightarrow \infty$), corresponding to $i = 0$.

Eq. 10 shows how overpotential depends on the applied current density, i.e., $\eta = f(i)$. The transfer coefficient reflects the shape of the charge-transfer energy barrier accounting, for a given applied potential, for the reaction's tendency to proceed in the anodic or cathodic direction. In addition, the

exchange current density (i_0) represents the oxidation and reduction rates at equilibrium, that is:

$$i_0 = i_a = -i_c \quad (11)$$

Specifically, i_0 is the current density at which the rate of oxidation and reduction are equal in a state of equilibrium. It is a kinetic parameter reflecting the intrinsic rates of electron transfer of an electrode reaction; the higher the exchange current, the faster the electrode reaction.

When η is large (anodically or cathodically), one of the exponential terms of the eq. 3 will be negligible compared to the other. In this case, B-V can be approximated by what is known as the Tafel equation, an experimental relationship between the current and the activation overpotential describing the kinetics of electrochemical processes, established in 1905 by Swiss chemist Julius Tafel:

$$\eta = a \pm b \log i \quad (12)$$

Where a is the overpotential at the unit current density, and b is the Tafel slope, which reflects the change rate of the overpotential as a function of the logarithm of the current density.

According to eq. 5, therefore, Tafel plots (η vs. $\log i$) at high overpotentials would be straight lines, from which the constants a_c and b_c could be evaluated. Tafel plots have been long known to fit activation overpotential experimental data for numerous cathodic and anodic reactions.

The Tafel equation has been confirmed for numerous cathodic and anodic reactions, and its use for the calculation of corrosion currents will be illustrated in the *Electrochemical Tests* section.

1.3.1.5 Corrosion Testing

Countless procedures have been developed over time to evaluate corrosion properties depending on application and reliability requirements to test the effectiveness of surface treatments in mitigating corrosion processes. For instance, it is essential to evaluate how well coatings protect the basis material against degradation processes. The underlying concept shared by most methods is accelerating degradation processes in a reproducible synthetic environment to mimic long real-life service periods in an acceptable time frame.

The following paragraphs will describe methods regarded as the most reliable in industry settings.

1.3.1.5.1 Salt Spray Test

The salt spray test (SST) has gained worldwide popularity due to its low cost and quickness in response. Moreover, it is well standardized and not requires skilled personnel. As a result, it is a de-facto industry standard in coatings quality assessment. Results are related to the coating's properties (e.g., porosity) and can reveal the presence of defects (e.g., cracks, pits, or incomplete coverage), giving helpful insight for manufacturing process improvements.

On the other hand, salt spray performance is weakly correlated to the coating's durability in real-life service conditions. Therefore, it is more often used in assessing coatings' protective capabilities on a comparative basis. Moreover, Salt Spray Test is destructive, could give very scattered results, and its evaluation is, to some extent, person-dependent and could lead to misinterpretation.

Salt spray testing (SST) is typically performed in accordance with the ISO 9227 or ASTM B117 testing procedure, which are nearly identical. In a typical salt spray test, samples are placed in a salt fog chamber at 35°C and exposed to dense fog and a highly corrosive atmosphere created from atomizing a 5% sodium chloride solution. Relative Humidity must be 95% minimum. The temperature is maintained at 35 ° C ± 2°C, and the pH is around neutrality (Neutral Salt Spray Test). The duration of the exposure will vary by product and application. Most testing is conducted in 24-hour increments. The most common test durations range from 24 to 1,000 hours.

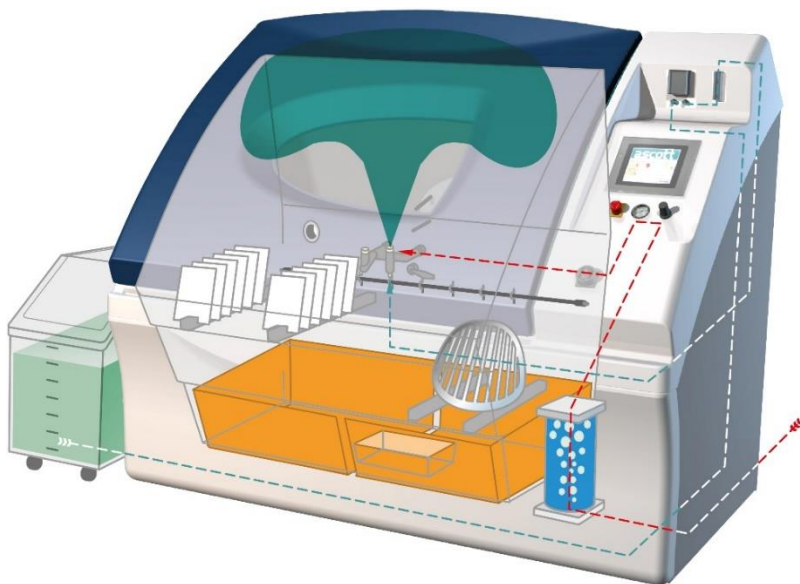


Figure 20 Illustration of a chamber undergoing Salt Spray Test.

1.3.1.5.2 Weight-Loss Measurements

In this technique, the sample is placed into a solution containing aggressive ions, e.g., Cl⁻. The weight of the samples is measured at regular intervals over a long period, such as a year. It can be converted to mol/(cm² s) or a corrosion current in A/cm² using Faraday's equation, presuming that only a loss of metal to the solution is the cause of the weight change, corrosion in the simplest case. The corrosion rate from weight loss, P_w (mm per year), can be determined using the following expression:

$$P_w = 2.10 \frac{\Delta W}{At} \quad (13)$$

Where ΔW (mg) is the metallic weight loss of the sample, A (cm²) is the exposed surface area of the sample, and t (days) is the total time of immersion. The weight-loss rate is not only an average corrosion rate over the immersion duration but also an average rate over the sample area.

1.3.1.5.3 Electrochemical Tests

As aforementioned, the corrosion mechanism in an aqueous phase is essentially of electrochemical nature. Therefore, the electrochemical signal is one of the primary sources of information regarding a corroding electrode's potential, current, and electrical charge. It arises from processes that cause corrosion and other electrochemical reactions.

Electrochemical techniques have, over all other corrosion test methods, the advantage of giving "numbers" as to the performance of a surface protective treatment and, therefore, are not subjective in nature.

1.3.1.5.3.1 Open Circuit Potential Measurement

OCP, also known as zero-current potential, corrosion potential, equilibrium potential, or rest potential, is generally the first step in most electrochemical corrosion experiments.

OCP is the equilibrium potential developed between the metallic sample (working electrode) and the electrolyte. The OCP is measured as the potential difference between the working (WE) electrodes and a reference (RE). As the name suggests, the measure is made while the circuit is open, meaning no current is flowing, and no external voltage is applied. Therefore, a high input impedance voltmeter is necessary.

Measuring an OCP can help determine if a metal, a metal alloy, or a coating will not corrode when exposed to a given environment. As already stated, a negative value indicates spontaneous corrosion. Therefore, simply monitoring OCP changes over time (several hours) for an electrochemical cell where the test sample is submerged in a suitable corroding media (e.g., 3.5 wt% NaCl water solution) can provide valuable insights into materials' corrosion resistance or the effectiveness of protective treatments. It is, in fact, well known that OCP may vary with the time of immersion in a corrosion environment because of changes occurring at the sample's surface (oxidation, formation of the passive layer, etc.).

All in all, the open circuit potential vs. time is a static, qualitative method suitable for evaluating sacrificial coating stability.

1.3.1.5.3.2 Polarization Techniques

The polarization resistance method, based on electrochemical concepts, enables the determination of instantaneous interfacial reaction rates such as corrosion rates (i_{corr}) and exchange current densities (i_0) from a single experiment. In contrast, other methods like electrical resistance change, gravimetric mass loss, or solution analysis for metallic cations, just to name a few, provide historical or integrated mass loss information from corrosion that has occurred over some period of time.

As already stated, corrosion current density (i_{corr}) and corrosion potential (E_{corr}) are essential to characterize the electrochemical kinetics of corroding metal.

i_{corr} is not directly accessible because it is related to an equilibrium condition with no net current flowing across the electrochemical cell and, therefore, neither through an external current-measuring device. However, it can be estimated from the current-voltage characteristics, the so-called polarization curve, obtained experimentally by plotting applied voltage against the measured current.

1.3.1.5.3.2.1 Tafel Extrapolation

Tafel extrapolation is a mathematical technique used to estimate the corrosion current (i_{corr}) or the corrosion potential (E_{corr}) in an electrochemical cell and, thereby, the corrosion rate.

The current density is usually a nonlinear function of the applied potential. However, as previously seen, the Tafel equation for irreversible processes predicts a straight line for the variation of the logarithm of current density with potential. The regions in which such relationships exist are known as

Tafel regions and are related to what is known as the Butler-Volmer high field approximation.

At sufficiently large values of η (typically between 100 and 500 mV) in the anodic direction, the eq. 14, becomes eq. 15. This is also true for cathodic overpotential so that the eq. 14, becomes eq. 16.

$$I = I_{corr} \left[\exp \left\{ \frac{2.303 (E - E_{corr})}{\beta_a} \right\} \right] - \left[\exp \left\{ - \frac{2.303 (E - E_{corr})}{\beta_c} \right\} \right] \quad (14)$$

$$\eta_a = \beta_a \log \frac{I}{I_{corr}} \quad (15)$$

$$\eta_c = -\beta_c \log \frac{I}{I_{corr}} \quad (16)$$

As reported in figure 21, linear extrapolation is performed by extending both the anodic and cathodic Tafel linear branches back to their intersection. These two lines eventually meet at a point whose coordinates are the corrosion potential (E_{corr}) and the corrosion current (I_{corr}). The Anodic Tafel Slope (β_a) and the Cathodic Tafel Slope (β_c) are also defined.

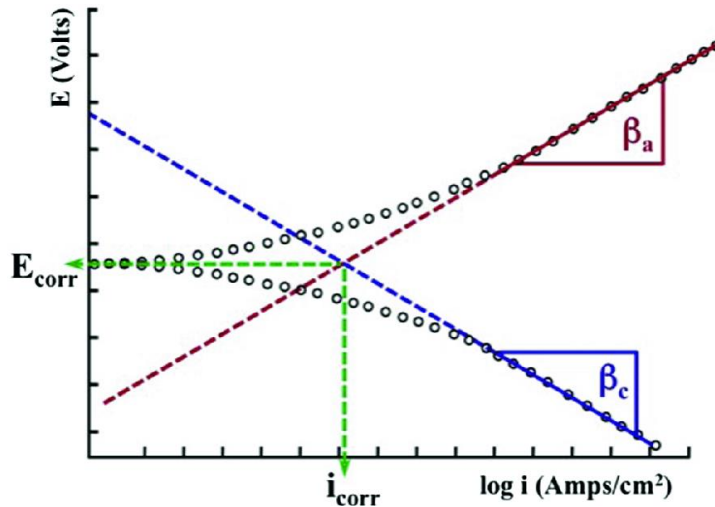


Figure 21 Schematic polarization curve showing Tafel extrapolation.

For a reliable extrapolation, the linear behavior over a few decades is ideal and at least for one decade necessary. The longer the linear behavior, the better the extrapolation. Unfortunately, many real-world corrosion systems do not provide a sufficient linear region to permit accurate extrapolation. Modern corrosion test software performs a more sophisticated numerical fit. Specifically, measured data are fitted to the Butler-Volmer equation by adjusting the values of E_{corr} , i_{corr} , β_a , and β_c . The curve-fitting method has the advantage that it does not require a fully developed linear portion of the curve.

A typical three-electrode electrochemical cell containing a working, counter, and reference electrode can be used to obtain polarization data.

Tafel extrapolation measurements can be performed either by potentiodynamic or by step-wise potentiostatic polarization method.

Corrosion potential is first measured, typically for one hour (during which time corrosion potentials of most electrodes are stabilized) or until it is

stabilized. The working electrode's potential is then varied by predetermined potential step increments (potential-step method) or scanned at a constant rate, typically 0.6 V/h, as for ASTM G 5 (potentiodynamic method), registering the corresponding change in current. In both methods, the experiment is started at corrosion potential, and the cathodic polarization is first conducted by applying an overpotential of approximately 500 mV or until gas (e.g., hydrogen) evolution occurs at the electrode. After that, corrosion potential is measured again (typically for an hour), and then anodic polarization is conducted by applying an overpotential so that the potential at the end of the anodic polarization is +1.6 V vs. SCE. Finally, the measured potential vs. log current values are plotted in the semi-logarithmic plot, obtaining two diverging logarithmic lines representing anodic and cathodic currents.

This method applies large overpotential to the metal surface and, therefore, is considered as destructive. This is particularly true during anodic polarization, when the metal surface may be permanently damaged. For this reason, it is not suitable as a corrosion monitoring technique. Nonetheless, it provides a straightforward method to determine i_{corr} and Tafel slopes.

The correlation of electrochemical measurements to as many varied measurements as possible is good practice. Electrochemical measurements may be the most rapid, but they are also the most susceptible to variations in conditions. Therefore, corrosion rate estimations based on Tafel extrapolation should be compared to weight loss measurements whenever possible.

1.3.1.5.3.2.2 Polarization Resistance Methods

The Tafel extrapolation technique allows determining the corrosion rate and the Tafel parameters. However, in most cases, it is unsuitable for instantaneous corrosion rate measurements because the system is polarized over a wide potential range, so the measurement is time-consuming. In addition, the electrode surface is affected during the measurement. The polarization resistance method, instead, based on electrochemical concepts, enables the determination of instantaneous interfacial reaction rates such as corrosion rates (i_{corr}) and exchange current densities (i_0) from a single experiment. Moreover, corrosion rate measurement is rapid, and due to the limited extent of the polarization, surface changes on an electrode and diffusion effects can be neglected. On the other hand, they do not provide Tafel slopes, which must be known to obtain i_{corr} from the Stern-Geary equation (eq. 11).

1.3.1.5.3.2.2.1 Linear Polarization Resistance (LPR)

About 60 years ago, Stern and Geary found that the current-potential plot around corrosion potential is essentially linear and defined its slope as polarization resistance (R_p or R_{ct}) because it has the unit of resistance (Ω). Mathematically:

$$R_p = \left(\frac{\Delta V}{\Delta I} \right)_{E_{corr}} \quad (17)$$

Therefore, R_p behaves like a resistor and reflects the kinetic facility of the cell reaction to occur.

At sufficiently small activation overpotentials, close to corrosion potential (low-field approximation), the Butler-Volmer equation can be reduced to one form of the Stern-Geary equation:

$$I_{corr} = \frac{1}{R_p} \left(\frac{\beta_a \cdot \beta_c}{2.303(\beta_a + \beta_c)} \right) \quad (18)$$

If β_a and β_c values are known, the corrosion rate can be calculated from R_p . Eq. 11, also reveals that the polarization resistance is inversely proportional to the corrosion rate.

In a linear polarization resistance experiment, a current versus voltage is recorded as the cell voltage is swept over a small range near E_{corr} (generally ± 10 mV). A numerical fit of the curve yields a value for the polarization resistance, R_p (see figure 22). Polarization resistance data do not provide any information about the values for the β coefficients. Therefore β values must be known to obtain corrosion current from eq. 11. Tafel constants can be obtained from a Tafel plot. Otherwise, both β_a and β_c could be assumed since, in most cases, their values fall between a fixed range (from 60 to 120 mV). It provides a rapid method of determining corrosion current even though it may lead to inaccurate results. Even if Tafel slopes are unknown, the R_p value can still be used as a quantitative parameter to compare the corrosion resistance of metals under various conditions. High R_p implies high corrosion resistance, while low R_p implies a lower one.

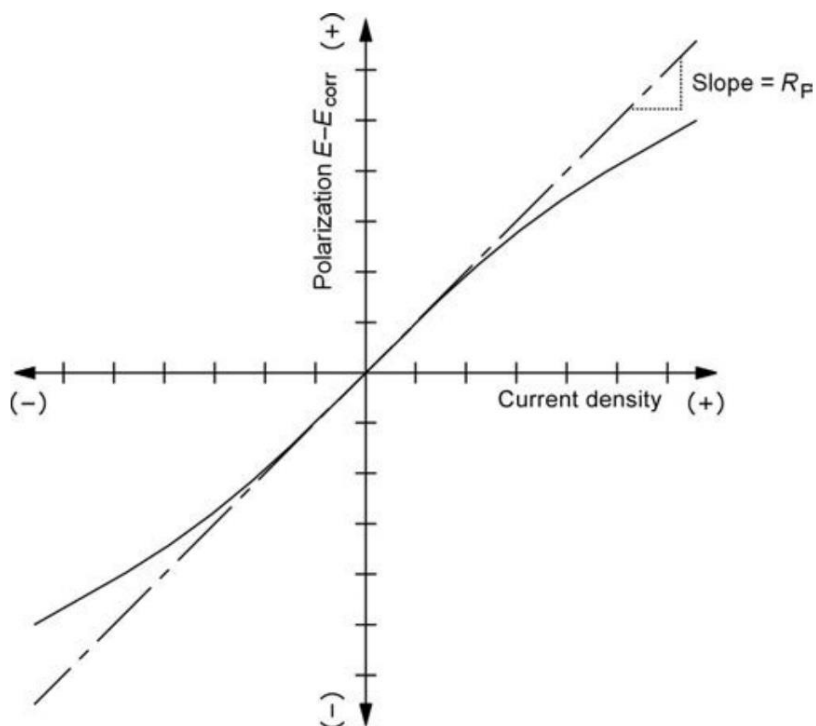


Figure 22 Example of a linear polarization resistance plot.

1.3.1.5.3.2.2.2 Electrochemical Impedance Spectroscopy (EIS)

Electrochemical impedance spectroscopy (EIS) is a non-destructive technique widely used in anticorrosive coatings characterization, enabling the study of various electrochemical phenomena occurring at a corroding metallic surface.

In the previously discussed polarization techniques (Tafel extrapolation or Linear Polarization), a voltage signal is applied to a system at a steady state, and the resulting current response is recorded in the time domain. In EIS, however, a small AC perturbation, i.e., a sine wave voltage $V(\omega)$ signal of less than 20 mV in amplitude to the corrosion potential, is applied over a wide range of frequency (from 10^5 down to 10^{-3} Hz) and the alternating current

response, $i(\omega)$, is measured at each frequency, ω (i.e., the ac polarization or angular frequency, $\omega = 2\pi f$). For a linear (ohmic) system, the current response signal will be a sine wave of the same frequency as the excitation signal (voltage) but shifted in phase. Therefore, the system's impedance and the phase shift are obtained using a frequency response analyzer (FRA). Full frequency sweeps provide phase-shift information that can be used in combination with equivalent circuit models to gain valuable information from the complex interface of the corrosion system. The frequency-dependent impedance is determined by the relation:

$$Z(\omega) = \frac{V(\omega)}{i(\omega)} \quad (19)$$

In most cases, the impedance corresponding to a simple corrosion process, under activation control, can be represented by the well-known Randles equivalent circuit (RC circuit), reported in figure 23, which describes the behavior of many electrochemical electrode/electrolyte interfaces:

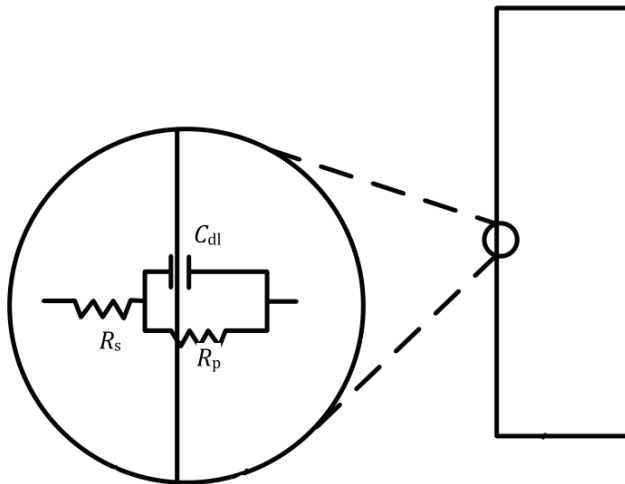


Figure 23 Simple Randles equivalent circuit

Where:

- R_s represents the solution resistance
- R_p is the Faradaic charge transfer resistance. If the signal amplitude is small enough (e.g., less than 20 mV), R_{CT} can be considered equivalent to the linear polarization resistance R_p .
- C_{dl} is the double-layer capacitance

The behavior of such an electrochemical interface can be described by the following equation:

$$Z(\omega) = R_s + \frac{R_p}{1 + (j\omega R_p C_{DL})^\beta} \quad (20)$$

R_p can be determined in several ways. A convenient way is to use the Nyquist diagram. For the simple Randles-type equivalent circuit depicted in Figure 23,

the corresponding Nyquist diagram depicting a perfect semicircle is shown in Figure 24. The high-frequency response is used to determine the component of R_S involved in the measurement. When the angular frequency ω ($\omega = 2\pi f$) tends toward infinity (f_{\max} or $f \rightarrow \infty$), R_S can be read directly from the abscissa. The total resistance ($R_P + R_S$) can also be read from the abscissa where ω approaches zero (f_{\min} or $f \rightarrow 0$).

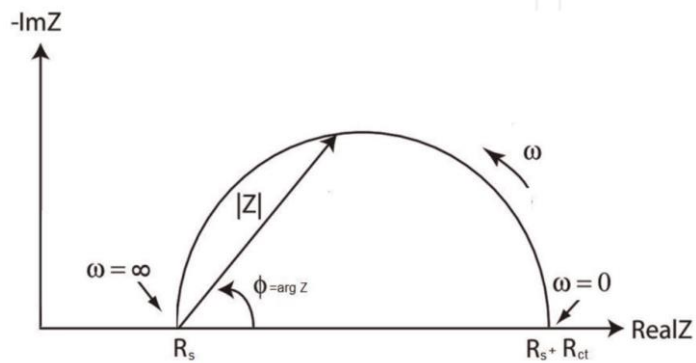


Figure 24 The Nyquist diagram responding to the simple Randels-type equivalent circuit.

Subtracting the R_S value from the low-frequency measurement yields the R_P value. The conversion of polarization resistance to corrosion rate necessitates an independent empirical measurement of the Tafel slopes utilizing the potentiodynamic polarization method.

Another essential parameter for corrosion study, the double-layer capacitance, C_{DL} , can also be determined for a system exhibiting behavior similar to a perfect RC circuit from the values of R_P and the maximum frequency, f_{\max} , that corresponds to the frequency of the point at which the imaginary component has a maximum value:

$$C_{DL} = \frac{1}{2\tau f_{max} R_p} \quad (21)$$

An alternative to the impedance model in the Nyquist diagram involves the conversion of the impedance into a complex number. Thus, the impedance can be denoted by its amplitude, $|Z|$, and its phase shift, φ , or by the sum of its real (Z') and imaginary (Z'') components, that is:

$$Z(\omega) = Z'(\omega) + jZ''(\omega) \quad (22)$$

In the so-called Bode Plot, the logarithm of the total impedance ($\log|Z|$) and the phase angle φ are plotted against the excitation signal's angular frequency, $\log \omega$. The advantage is that the frequency dependence is clearly visible. Conversely, the Bode plot is not very sensitive, i.e., it does not show significant variations until the system under investigation completely changes its behavior.

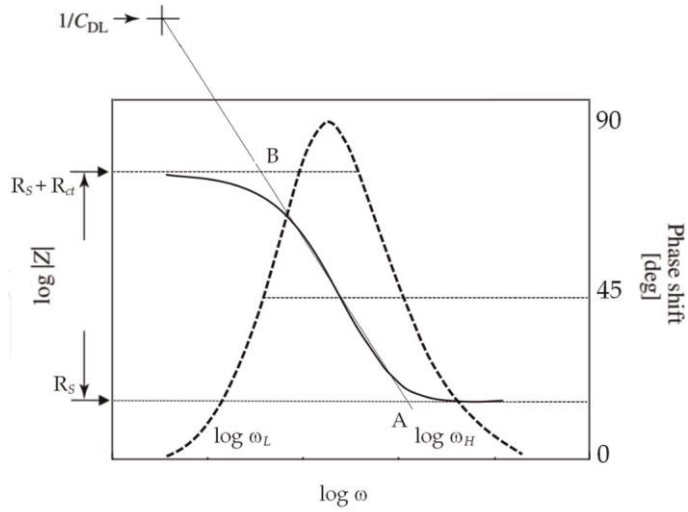


Figure 25 Example of Bode diagram for a Randles equivalent circuit.

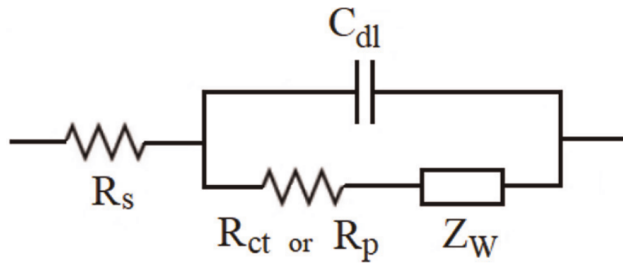


Figure 26 A Randles-type equivalent circuit including Warburg impedance component, Z_w .

Figure 25 shows how the same data (Nyquist plot) appears in a Bode plot format concerning the equivalent circuit of Figure 23. Highest (ω_H), and lowest frequencies (ω_L) can be readily determined. Figure 25 shows that Z is independent of frequency at ω_H and ω_L , with limit values represented by horizontal lines. The R_S and $(R_S + R_p)$ values can be calculated from these lines. This analysis forms the basis of the corrosion monitoring allowing the

determination of $|Z|$ at each frequency in the horizontal portions of the Bode diagram.

EIS can be a very time-consuming technique. The testing time is determined mainly by low-frequency measurements as the measurement time increases as the frequency decreases. For example, a single-frequency cycle at 10⁻³ Hz needs about 15 min and a full high-to-low-frequency scan likely requires more than 2 hours. Sometimes, performing impedance measurements at very low frequencies could be inconvenient. However, it is still possible to extrapolate the polarization resistance, R_p , from the Bode diagram.

In Figure 25, the low- and high-frequency breakpoints (i.e., ω_L and ω_H , respectively) can be determined from the 45° phase angle Bode diagram (see the pseudo- Gaussian curve). The intersection point A can be determined from the log ω_H and R_S . A linear line can be determined by extrapolating from A toward the central linear portion of the $|Z|$ curve. On this line, point B is obtained at log ω_L . With the projection of point B to the log $|Z|$ axis, the total resistance ($R_S + R_{CT}$) can be measured. In this way, R_p can be determined. At intermediate frequencies, the capacitor affects the response of the overall RC circuit. The situation struggles when diffusion processes govern the corrosion behavior. A convenient way to deal with this complication is to add a Warburg impedance. The latter describes the impedance of the concentration and diffusion processes in the equivalent circuit, as shown in Figure 26. The Warburg impedance, Z_w , is given by the equation:

$$Z_W = \frac{\sigma_w}{\sqrt{\omega}} - j \frac{\sigma_w}{\sqrt{\omega}} \quad (23)$$

where σ_w is the Warburg coefficient.

Eq. Y implies that whatever the frequency, the real and imaginary parts of the Warburg impedance are equal and inversely proportional to $\sigma\omega^{1/2}$. In the Nyquist plot, this impedance will result in a straight line at a constant phase angle at 45° , as shown in Figure 26. However, the effect of the Warburg impedance can complicate the correct estimate of the R_p value in some instances. Therefore, the impedance data must be numerically adjusted to fit with the correct model to facilitate the extraction of the total resistance ($R_s + R_p$) from the abscissa or by using appropriate modeling software. In this regard, it is worth noting that an appropriate equivalent circuit model is understood not only as a good fit for the impedance data but also to be consistent with the underlying processes occurring at the electrode-electrolyte interface.

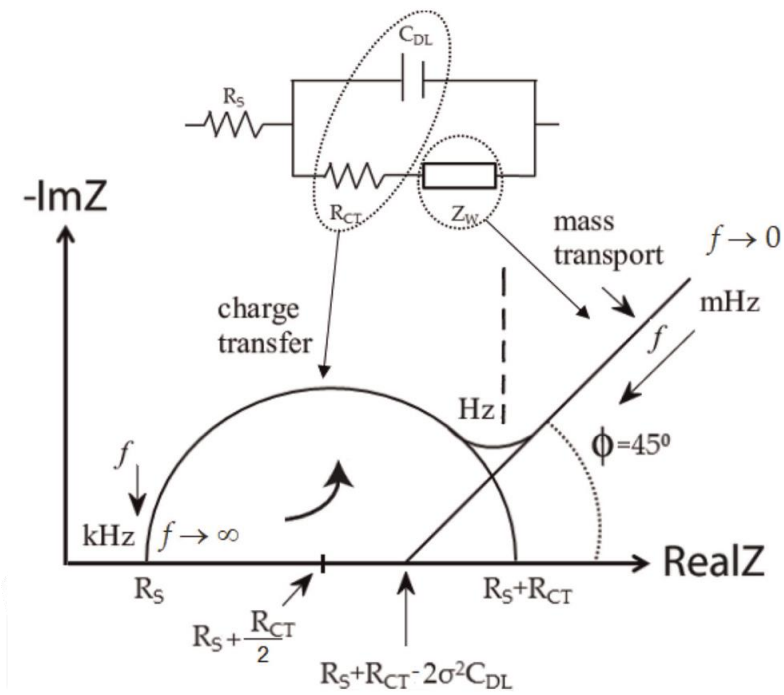


Figure 27 The Nyquist diagram corresponding to the equivalent circuit of Figure 26.

As mentioned above, the time required to perform EIS characterization represents a shortcoming. The requirement of a sophisticated AC frequency generator and analyzer and the time needed to acquire the complete impedance diagram could pose a severe limitation in using EIS for real-time corrosion monitoring applications. Other disadvantages include a priori knowledge of the Tafel parameters to convert the polarization resistance into a corrosion rate and the complexity of equivalent circuit modeling.

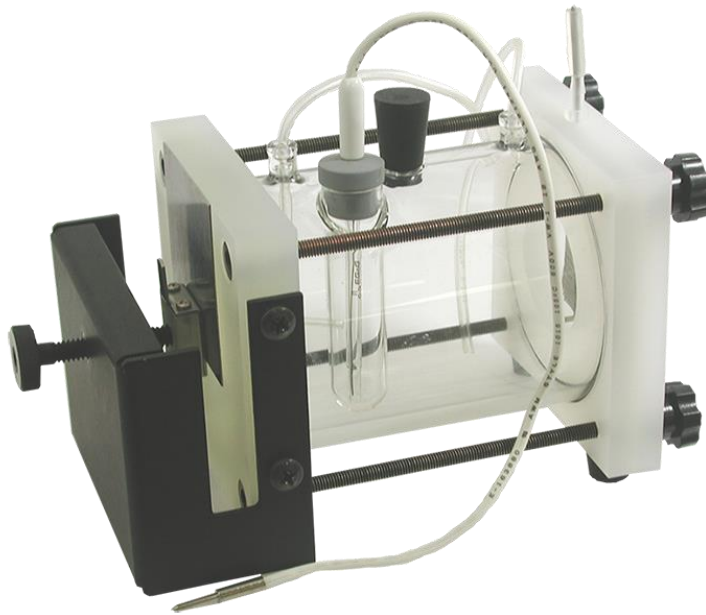


Figure 28 Flat cell equipment for corrosion measurements

1.3.1.5.3.2.3 Calculation of corrosion rates

Corrosion current values obtained from polarization resistance and Tafel extrapolation methods should be converted into corrosion rate. For this reason, it should be assumed that the current distribution is uniform across the area used in the calculation.

According to Faraday's law, then corrosion rate (CR) or mass loss rate (MR) can be calculated as:

$$CR = K_1 \left(\frac{i_{corr}}{d} \right) EW \quad (24)$$

$$MR = K_2 \cdot i_{corr} \cdot EW \quad (25)$$

Where:

- CR is given in mm/yr
- i_{corr} in $\mu\text{A}/\text{cm}^2$
- K_1 is $3.27 \text{ e-}03$ in $(\text{mm g})/(\mu\text{A cm y})$
- MR is in g/m^2
- K_2 is $8.954 \text{ e-}03$ in $(\text{g cm}^2)/(\mu\text{A m}^2)$
- d is the density in g/cm^3
- EW is the equivalent weight

Equivalent weight, EW, is the mass in grams that will be oxidized by the passage of one Faraday (96,489C (amp-sec)) of electric charge, and EW of pure elements is calculated as:

$$EW = \frac{W}{n} \tag{26}$$

Where W is the element's atomic weight, and n is the number of electrons required to oxidize an atom of the element in the corrosion process, that is, the element's valence. ASTM G102 details corrosion rate calculation from corrosion current determined by polarization techniques. This standard also provides the EW values for selected metals.

1.4 Metal Coatings Thickness Measurement Techniques

1.4.1 Introduction

Deposit thickness and its homogeneity are among the most critical parameters of both functional and decorative coatings. As per other surface finishing treatments, plating has the purpose of nobilitating a substrate, i.e., imparting desired characteristics like improving aesthetic appeal, mechanical properties, corrosion and wear resistance, etc.

For a given coating material to achieve specific quality requirements, the thickness range is well-defined and often very narrow, even though it is indeed true that the required value may vary depending on the deposition method. Reliable thickness measurement methods are, therefore, needed to ensure suitable characteristics in the final workpiece.

Different techniques can be employed to investigate films' thickness, even though each method has its limitations with respect to the measurement range, which can span from atomic monolayer to millimeters, and the physicochemical properties of both the coating and the substrate.

Thickness measurement methods can be divided into destructive and non-destructive, depending on the effect the gauging process produces on tested items. Destructive methods are based upon direct measurement; they generally involve microscopic techniques, requiring no mathematical derivation. The price to pay is a sample-specific preparation, often costly and time-consuming; moreover, the analyzed sample cannot be used for further characterizations and must be disposed of.

On the other hand, non-destructive methods are based on the measurements of other variables related to the thickness by some known relation, entailing some a priori assumptions. Nevertheless, the virtue is a faster, non-destructive, and, in most cases, non-contact analysis, making it suitable for in-line and QC analysis.

The methods commonly used take advantage of the coating-substrate combination's electrical, magnetic and chemical properties, including the effect of irradiating the specimens with X-rays or beta-rays. However, all methods have in common, regardless of the physical nature of the measurand (i.e., the working principle), that they must be calibrated against known thickness standards. The accuracy of a measurement, therefore, is dependent upon the reliability of the calibration standards. In addition, calibration standards should correspond to the coating-substrate combination being measured.

1.4.2 Destructive Methods

1.4.2.1 Microscopical Methods: Light and Electron Microscopy

In microscopical methods, the thickness is measured in a magnified image of a coating cross-section. Light or electron microscopy can be used depending on the degree of accuracy and expected thickness magnitude. Regardless of the technique being used, mechanical cross-sectioning is a mandatory step. Sample preparation usually requires a specific sequence of operations, including sectioning, mounting, grinding, polishing, and cleaning. Each of these steps can be carried out in different ways and may vary according to the specific material properties. Great care must be taken in performing each

step because carelessness at any stage may affect the later steps and introduce artifacts that reduce accuracy, even compromising the analytical process. For example, if the plane of the cross-section is not perpendicular to the plane of the coating, the measured thickness will be greater than the actual thickness (an inclination of 10° to the perpendicular will contribute a 1,5 % error).

For what concern light microscopy, an appreciable chromatic contrast between substrate and coating(s) is needed in order to perceive their boundaries, although image processing softwares can be used to enhance the contrast. The accuracy and reliability of results can be traced back to the stage micrometer used in calibrating the vernier divisions on the filar eyepiece and the alignment and focus of the mount. However, with careful specimen preparation and suitable instruments, the light microscope method can provide a measurement uncertainty of $0,4 \mu\text{m}$ under reproducible conditions, and for thicknesses greater than $25 \mu\text{m}$, a reasonable error is of the order of 5 % or better.

The minimum lateral resolution of visible light-based microscopy techniques is around 200 nm, which corresponds to Abbe's diffraction limit. Electron microscopy can be used if the coating's thickness is lower than this value. Some requirements are needed for a sample to be analyzed by SEM. It must be stable in high vacuum (about 10^{-7} bar), under irradiation by an electron beam, and conductive (it has to be made conductive if it is not).

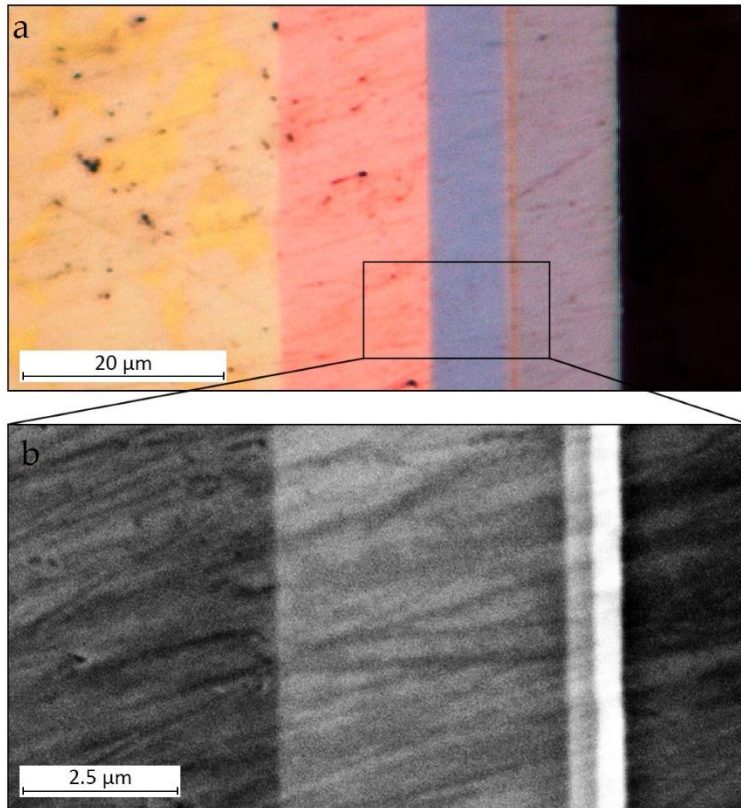


Figure 29 Multilayered coating's cross-sectional view obtained by (a) optical microscope and (b) SEM

The lateral resolution of a modern thermionic emission-based SEM (the lower expensive one) is about 2-20 nm, depending on operating parameters. SEM images can be acquired using different signals: (a) secondary electrons (SE), (b) backscattered electrons (BSE), or through a (c) microanalysis map, each with its resolution, depending on the interaction volume size (i.e., the lower is the interaction volume, the better is the resolution, see fig. X). SE obtains the best resolution; therefore, it is usually used to measure coating thicknesses. Using BSE instead of SE can help distinguish metal layers with atomic numbers as close together as 1.0 but at a cost of lower resolution

(about 0.1 μm). Many SEMs are also equipped with energy-dispersive X-ray spectroscopy (EDS), which can help identify the metal-coating layers. However, at best, the resolution of EDS is about 1 μm , and often it is poorer.

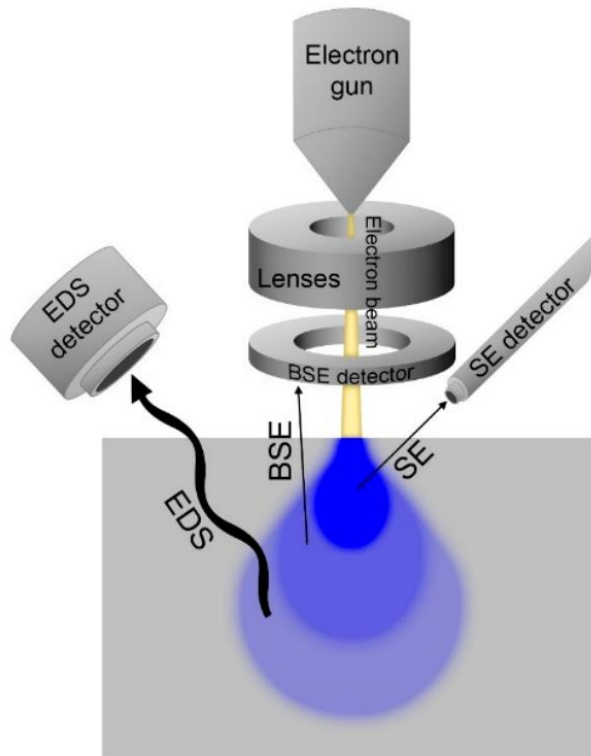


Figure 30 Scheme of a SEM with SE, BSE, and EDS volume of interaction and the corresponding detectors.

1.4.2.2 Profilometric stylus method

This mechanical method requires the presence of a groove or a step from the surface of the substrate to that of the coating. Such grooves or steps can be produced by suitable masking portions of the substrate during the coating process or by removing parts of the film after deposition. Then the stylus is drawn across this step, and its height is determined by electronically measuring and recording the stylus displacement in the so-called step-height profile method (see figure 31).

The surface roughness can be a source of noise that may reflect measurement accuracy; this inconvenience can be partially eliminated using averaging algorithms implemented by manufacturers in the control software. Commercial instruments allow measurements over the range of 0,01 mm to 0,000 02 mm (20 nm), with adequate measurement uncertainty (less than 10% of the thickness).

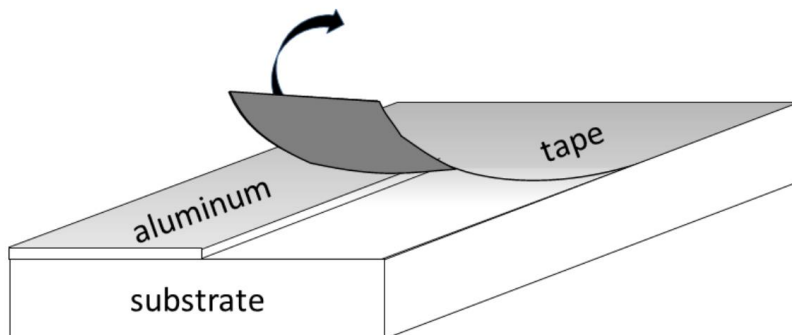


Figure 31 Coating masking method for measuring the thickness of an evaporated aluminum film

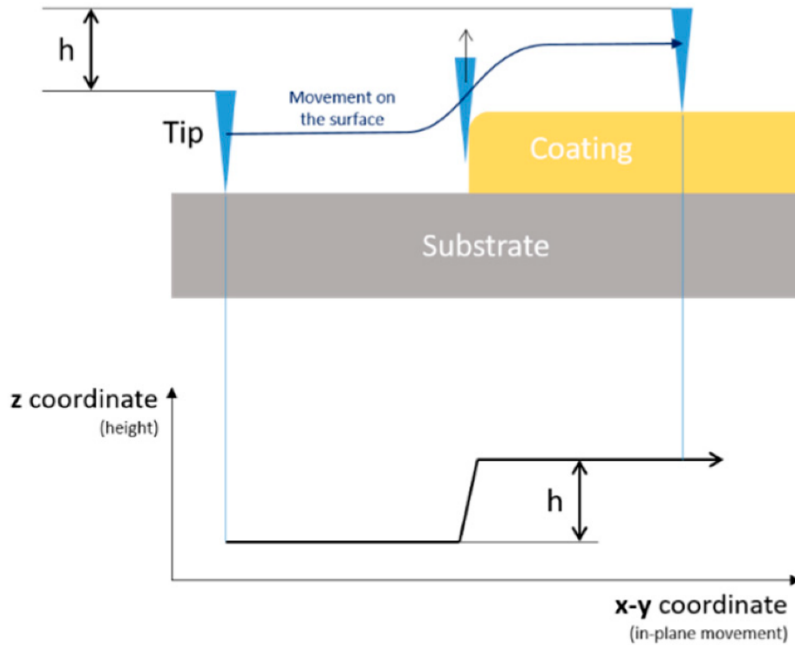


Figure 32 Schematic diagram of thickness measurement by step-height profile analysis.

1.4.2.3 Gravimetric Methods

Gravimetric methods are undoubtedly the most straightforward, but their feasibility can be limited by manufacturing processes' constraints. Specific calibration standards are recommended for quality control because of deposit densities inherent in various coating processes. The main limitation is that only the average thickness of the entire specimen is obtained or, at most, over the measuring areas. Therefore, the presence of bare spots or sites with thicknesses lower than the specified minimum cannot be assessed, and density inhomogeneity affects the reliability of results.

1.4.2.4 Weight Gain Method

The weight gain method is essentially based on differential weighting: the samples are weighed before and after the coating process. A calculation for thickness can be made from the difference in weight, area, and density.

1.4.2.5 Strip and weigh method

This method determines the coating weight by weighing the sample before and after the chemical dissolution of the coating without attacking the substrate. The weight of the coating divided by its density gives the average coating thickness.

1.4.2.6 Coulometric method

The coulometric method is based on Faraday's Law. Coating thickness is determined by measuring the electricity consumed by its anodic dissolution from an accurately defined area in a suitable electrolyte. The change in potential occurring when the substrate is exposed indicates the end point of the dissolution.

The anodic dissolution-based method is considered an accurate means for determining thickness, as an uncertainty of less than 10% is generally obtained. However, assuming a 100% current efficiency could be a source of error. Moreover, the coating densities value is taken as reported in literature for bulk metals. However, this is seldom true because coating density depends on the manufacturing process and may vary by as much as 10 to 20% from tabulated ones.

Finally, it is worth noting how thickness values obtained by the coulometric method, as per gravimetric methods (i.e., those based on mass per unit area measurement), are averaged over the all stripped area.

1.4.2.7 Ball crater test

The ball crater test also known as crater grinding method, calotte grinding method, spherical abrasion wear test, and Calotest, is a simple and inexpensive method used to measure the thickness of coatings. Coatings with thicknesses typically between 0.1 to 50 micrometers, such as those obtained from Physical Vapor Deposition (PVD) or Chemical Vapor Deposition (CVD).

The Calo tester consists of a holder for the surface to be tested and a steel sphere of known diameter that is rotated against the surface by a rotating shaft connected to a motor whilst diamond paste is applied to the contact area. The sphere is rotated for a certain amount of time (less than 20 seconds for a 0.1 to 5 micrometer thickness) sufficient to wear a tiny crater through the coating. An optical microscope is used to measure crater size, and the coating thickness is calculated using a simple geometrical equation:

$$t = \frac{x \cdot y}{2r} \quad (27)$$

As can be seen in figures 33, x and y refer to the calotte dimensions, and r is the radius of excavating sphere.

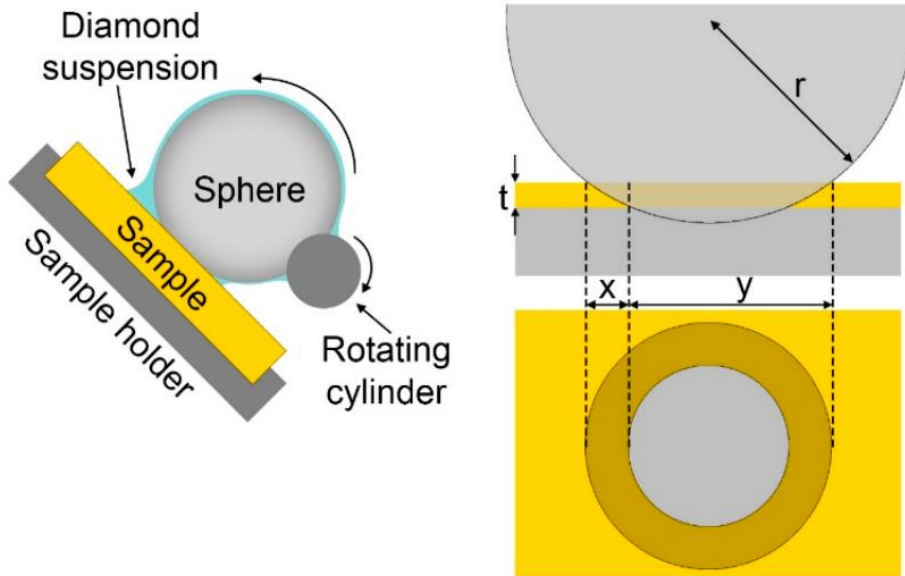


Figure 33 Schematic representation of Calotest working principle

1.4.3 Non-destructive Methods

1.4.3.1 Magnetic methods

Magnetic methods measure either the magnetic attraction between a magnet and the basis metal, as influenced by the presence of the coating, or the hampering of magnetic flux paths in passing through the coating and the basis metal.

Because they are based on magnetic interactions, these methods are limited in practice to non-magnetic coatings on a magnetic substrate and electroplated nickel coatings on a magnetic or non-magnetic substrate.

1.4.3.2 X-ray Fluorescence Spectroscopy

X-ray fluorescence spectroscopy (XRF) is widely used for materials' elemental and chemical analysis. XRF is the most common instrument used by industries for film thickness investigations since it is fast, non-destructive, and relatively simple to use, making it perfect for the quality control of products. For this reason, there are also technical standard procedures to accomplish measurements ISO 3497 and ASTM B568 regulations.

In the XRF technique, thickness is obtained by measuring the fluorescent (or secondary) x-ray emitted from a sample when it is excited by a primary x-ray source. The intensity of the emitted secondary x-ray radiation depends, in general, upon the excitation energy, the atomic numbers of the coating and substrate, the power of the X-ray tube, and the mass per unit area of the coating. Assuming that all other variables are fixed, the strength of the secondary radiation signal depends upon the mass per unit area of the coating (and thus the linear coating thickness if the density is known). The relationship between these parameters is first established by calibrating instruments using reference standards having coatings of known mass per unit area. Then, if the coating material density is known, such standards can have coatings given in linear thickness units, provided that the actual density value is also given.

The measurable thickness range depends on the atomic numbers and densities of the materials involved. The thickness of the coating layers does not exceed a critical value called "infinite thickness," which is the maximum thickness value that can be measured. This threshold is reached when the signal from the substrate or a layer is totally extinguished by an intermediate layer or the layer itself, i.e., secondary x-ray emission reaches a plateau.

Therefore, beyond this point, an increase in thickness does not produce a further change in the secondary emission signals. For metals, thickness up to 15-20 μm can be generally measured.

Depending on the characteristic x-ray emission being measured (that of coating or the substrate), emission and absorption techniques can be distinguished. In the emission method, the intensity of the characteristic radiation from the coating is measured. When the X-ray emission method is used, the equipment is adjusted to receive a selected band of energies characteristic of the coating material. Hence thin coatings produce low intensities, and thick coatings produce high intensities. In the absorption method, thickness is obtained by measuring characteristic radiation from the substrate; therefore, the intensity decreases with an increase in thickness (see figure 34).

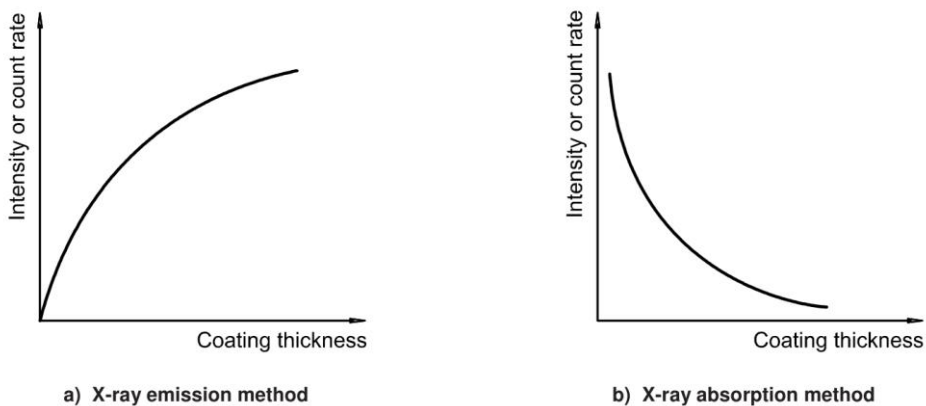


Figure 34 Schematic illustrations of the relationship between intensity or count rate and coating

The substrate's composition is typically not a driving force for accurate analysis. However, a less dense substrate material creates a larger background, originating from the primary x-rays scattered by the sample into

the detector. Lighter elements are a major source of x-ray scattering (rather than providing characteristic fluoresced X-rays). The background radiation increases the noise in the system and may result in underreports for coating thicknesses. Therefore its subtraction is generally helpful in improving the accuracy of quantitative analysis.

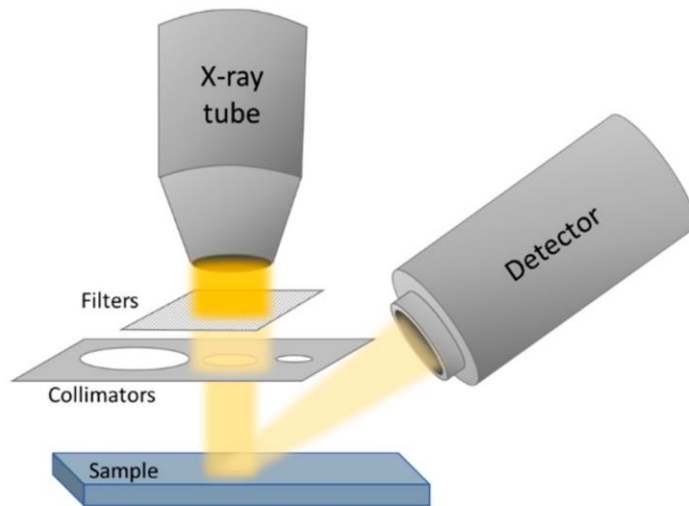


Figure 35 Schematic diagram of an XRF instrument

Section 2

2 A robust and cost-effective protocol to fabricate calibration standards for the thickness determination of metal coatings by XRF

2.1 Introduction

Electroplating is a process of applying a metallic coating onto a conductive surface through electrochemical deposition. As industrial process is one of the most widespread, representing around 37% of the total market share within the metal finishing sector [1], with applications ranging from automotive and aerospace to jewelry. Electroplating is considered one of the easiest and cost-effective surface engineering processes that improve materials properties from both functional and aesthetical points of view.

The primary purpose of decorative plating is to enhance the appearance of the articles. However, the coatings may also be required to meet stringent performance criteria, including adhesion, ductility, corrosion resistance, etc., depending on the application and service conditions.

Thickness, microstructure, and surface morphology are among the most critical factors determining the final properties of the coatings. Corrosion resistance has often been shown to be intimately related to the thickness of the deposit [2]. Thus, there are minimums and maximums in plating thickness specifications that must be adhered to for the item to perform as designed. Moreover, the rising of precious metals stock prices and the increasing quality requirements from leading luxury brands have constrained the

electroplating industry to improve the reliability of manufacturing processes and achieve more precise control of metallic film thickness [3].

The thickness of plated objects should be as uniform as possible. In this regard, edge effects (i.e., increased coating thickness near the edges resulting from higher current densities) can be troublesome [4].

It is well known that the deposit's thickness is directly related to the current distribution, pertaining to the specific conditions of the plating [5]. Current distribution depends, in turn, on the bath composition, which determines the conductivity in solution and, thus, affects the deposition kinetics. It also depends on the applied current density, the temperature, and the geometry of the plated items. Moreover, the relative position of anodes and cathodes and their area ratio can play a significant role, sometimes overcoming the plating bath's inherent limitations. Based on thickness data, it is possible to optimize plating process parameters improving quality and yield, either by trial-and-error approach or assisted by Finite Element Analysis simulation [6]. For such reasons, coating thickness determination plays a crucial role in electroplating applications.

There are several methods to determine the thickness of metallic coatings [7], which can be divided into two main categories: destructive and non-destructive. A destructive test is one where the specimen must be destroyed to obtain a reading; these are mostly based on the sample's cross-sectioning. Coating thickness is, thus, determined through microscopy observation. Light and scanning electron microscopy (SEM) are both appropriate [8,9], albeit the latter is most suited for thicknesses in the submicrometric range due to the higher resolving power. The main advantage of cross-sectional methods is that they do not require known thickness standards. Nevertheless, the

sample preparation process is a very time-consuming step and may produce artifacts that invalidate the subsequent analysis. Furthermore, it is a profile measurement and consequently may not be truly representative of the specimen. More sophisticated techniques like Focused Ion Beam Cross-Sectioning coupled with SEM (FIB-SEM) [10] or Secondary Ion Mass Spectrometry (SIMS) [11] mostly concern with R&D purposes due to high costs and the need for highly specialized personnel.

X-ray spectrometric methods, notably energy-dispersive X-ray fluorescence spectrometry (ED-XRF), are the most widespread in the electroplating industry sector thanks to their ease of use, robustness, and non-destructive nature. XRF quantitative analysis, the step in which the element concentrations or film thicknesses are computed from the intensities, can be performed either standardless or using standards to calibrate the analytical parameters. Both are based on the proportional relationships between the intensity (count rate) of the emitted X-ray fluorescence signal (emission method) and the coating thickness for a known structure and composition sample. With standardless analysis, all parameters are based on theoretical equations, the fundamental parameter database, precise detector modeling, X-ray tube, and spectrometer geometry (i.e., incidence and take-off angles). Fundamental Parameter (FP) uses theoretical intensity calculations to determine the composition from the measured intensities [12]. Recently, in addition to the FP method, thanks to the increasing power of conventional computers, computational procedures that exploit Monte Carlo simulations to generate calibration curves are rising [13–15] along with multivariate calibration procedure [16,17], nevertheless the FP method is still the only one present in commercial software.

Modern instruments are often sold with commercial precalibrated semiquantitative analysis programs in which FP methods are combined with a few empirical standards (at least one) for matrix effects corrections [14,18].

Thickness determination by FP method is affected by a significant error. Typical accuracy for single-layer samples is $\pm 5\%$ and is even greater for underlayer coatings in multi-layered samples [14,19,20]. More accurate thickness determination can be achieved by interpolating calibration curves built from known thickness standards.

Quantitative methods implemented by XRF systems require at least one known thickness standard to generate a second-order calibration curve, with the other points represented by zero and infinite thickness (a bulk form of the same material of the coating to be determined).

Measurement accuracy depends on the reliability of the calibration standards, commonly supplied with uncertainty (95% confidence interval) of $\pm 5\%$ from the stated value [21]. Certified Reference Materials (CRMs) are expensive and must be periodically replaced due to a limited shelf-life. A one-year recertification interval is a typical frequency suggested by many CRMs suppliers.

The coating properties are strongly affected by deposition techniques, not always specified in the calibration certificates. For XRF gauging, the thickness response depends, among others, upon specimen density and composition [22], which may vary as a function of the manufacturing process, e.g., differences in microstructure and surface roughness or the presence of voids [23]. Therefore, calibration standards and samples should be as similar as possible or independently characterized, avoiding the assumption of bulk

values. Moreover, primary standards should match the coating-substrate combination being determined, and it is not always possible to obtain calibrated standards for every conceivable coating architecture.

Therefore, measuring the thickness for various coating-substrate combinations can be a costly and time-consuming task. Thus, self-production of reproducible homogeneous metallic coatings with varying properties as needed represents an attractive opportunity for companies in the electroplating and metal finishing sector.

Despite recent environmental concerns, nickel is still one of the most suited metals in galvanic deposition processes due to its unique combination of excellent corrosion, wear resistance performance, and high hardness [24]. In multi-layered architecture coatings, nickel is generally suited as an interlayer [25], acting as a barrier between the substrate and coatings (metallic films), thus enhancing corrosion resistance and preventing diffusion of upper-layer materials in the inward direction.

In this context, this work aims to provide a cost-effective way to allow the platers to make up their own reference standards to achieve greater accuracy than standardless methods. Specifically, in this study, samples were prepared by coating a brass substrate with nickel of varying thickness to be used as references for XRF measurements.

As described by the flowchart in figure 36 we start conducting a feasibility assessment using current distribution simulations. Choosing appropriate nominal thicknesses, we performed Nickel electrodeposition over brass plates directly in the manufacturing line. After a thickness uniformity screening, performed by just comparing net X-ray peak intensities of

different points within the same plate, we measured absolute thickness values of the central slices by SEM and Light microscopy cross-sectional analysis. These data were used to construct a calibration curve that correlates radiation intensity and thickness in the next step. We have then compared these results with obtained from both certified reference materials and standardless Fundamental Parameters method.

2.2 Material and methods

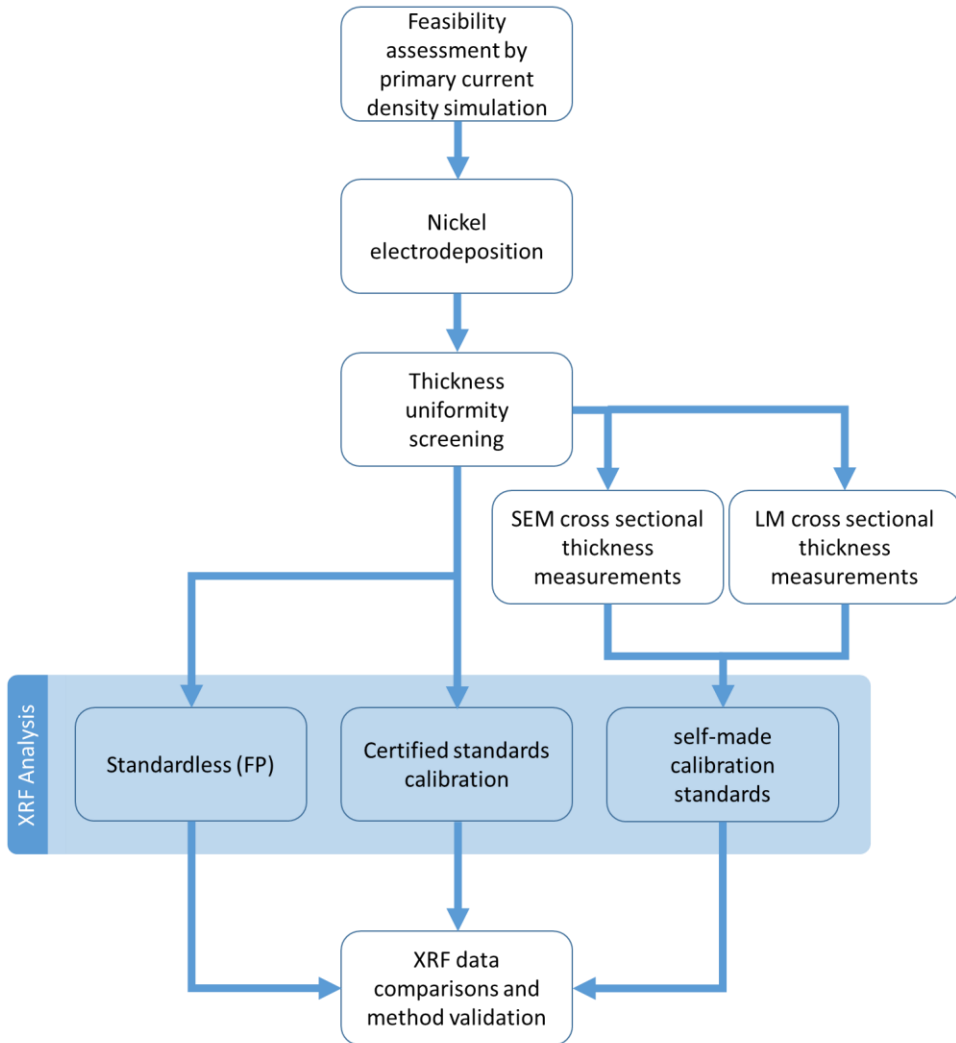


Figure 36: flowchart of research methodology

2.2.1 *Electroplating*

Nickel electrodeposition was performed through an industrial galvanic line using standard brass plates as substrates (10 cm x 7.5 cm x 0.25 mm). According to the electroplating production process before electroplating, the surfaces were prepared by 60 seconds of alkaline ultrasonic cleaning followed by 120 seconds of electrolytic cyanide degreasing.

Nickel electroplating was carried out in a commercial bright nickel bath for decorative applications in potentiostatic conditions, applying 2,8 Volts (DC) of potential difference between electrodes. The plating tank was rectangular shaped and equipped with two titanium baskets filled with electrolytic grade nickel pellets as anodes, arranged on both sides each at 23 dm from the cathode. Other operating parameters are listed below:

- pH: 4,5
- temperature: 60 °C
- plating solution conductivity: 91,3 mS/cm at 60°C
- anode-cathode distance: 23 cm
- agitation type: pumped flow eductor agitation and cathode reciprocation
- $\text{NiSO}_4 \cdot 6\text{H}_2\text{O}$ 230 g/L; $\text{NiCl}_2 \cdot 6\text{H}_2\text{O}$ 50 g/L; H_3BO_3 48 g/L

In order to obtain deposits of four different thicknesses, the plating time was varied from 2 minutes to 26 minutes. Times were calculated from deposition

speed reported on bath specifications. Each deposition was repeated three times. In total, 12 samples were produced and named as listed in the following table:

GROUP	1	2	3	4
SAMPLE	1A; 1B; 1C	2A; 2B; 2C	3A; 3B; 3C	4A; 4B; 4C
TIME OF DEPOSITION	2 minutes	6.5 minutes	13 minutes	26 minutes
NOMINAL THICKNESS	1.2 μm	3.9 μm	7.8 μm	15.6 μm

Table 1: nominal thickness of twelve samples by deposition time

2.2.2 *Current density simulation (IDC2D)*

Current density calculations were carried out to roughly evaluate the relationship between substrate dimension and thickness distribution by IDC2D [26], a bitmap-based 2D simulation software developed for PCB circuit design. As input, we used a 2500 px x 2500 px image to simulate 50 cm x 50 cm portion of the electroplating bath, corresponding to a resolution of 200 $\mu\text{m}/\text{px}$.

2.2.3 *XRF measurements*

XRF measurements were carried out using the Shimadzu EDX-7000 benchtop spectrometer (Shimadzu Co., Kyoto, Japan). The spectrometer was equipped with a rhodium anode (100 μA of tube current, 50 kV of tube voltage, and 50 W of power) and a silicon drift detector with an active area of 25 mm², 0.5 mm thickness. The energy resolution at the Mn-K α line was 135 eV. Spectra

were collected using the larger collimator (10 mm) to achieve better counting statistics since no restrictions were related to sample geometry; the acquisition time was set to 60 seconds, as a trade-off between accuracy and duration of the measurement session.

2.2.4 Cross-section analysis

To determine the thickness of the nickel deposits, selected plates were cut in half to expose their central portion. Samples were then prepared according to standard metallographic specimen preparation protocols [7]. A gold topcoat was applied by electroplating over metallic slabs obtained from samples. Overlapping with a contrasting color metal either facilitates cross-section observation by light microscopy technique and reduces artifacts from the subsequent mechanical preparation. The 1 cm central sections were first embedded in the phenolic resin by the hot-mounting process. They were then grinded and mechanically polished up to the mirror finish (the final step was carried out with 1 μm polycrystalline diamond suspension). Then the metallographic sections were examined using light microscopy (LM) and scanning electron microscopy coupled with energy dispersive X-ray detector (SEM-EDS) method. Light microscopy observation was made by a Nikon Eclipse L150 industrial microscope (Tokyo, Japan) in plane-polarized light and under crossed Nicols.

SEM micrographs were obtained with Variable Pressure Hitachi SU3800 SEM equipped with Ultim Max 40 Analytical Silicon Drift EDS Detector (energy resolution of 127eV at the Mn-K α line), X4 Pulse Processor, and AZtecLive software (Oxford Instruments NanoAnalysis, Abingdon, United Kingdom). Because of the poor visual contrast between the given coating (Ni) materials

and substrate (CuZn) in both secondary and backscattered imaging modes, thicknesses were measured in combination with the EDS technique. X-ray elemental mapping was carried out at 15 kV accelerating voltage and 10 mm of working distance.

2.3 Results and Discussion

2.3.1 *Current density simulation*

We performed preliminary tests using the primary current density simulator IDC2D to roughly evaluate the appropriate substrate size needed to achieve a sufficiently large area with a homogeneous deposit and minimal edge effect. Calculations were made only considering the electrical conductivity of the electroplating bath and cell geometry along the horizontal section. Results account exclusively for the primary current distribution; effects of overpotential (secondary current distribution) and concentration gradient (tertiary current distribution) are, therefore, neglected.

Multiple calculations were made to varying cathode sizes with fixed electrical conductivity values and anode-to-cathode distance. The simulated cathode dimensions were: 0.5 cm, 2.5 cm, 5.0 cm, 7.5 cm and 10.0 cm. The rationale was to check if the chosen substrate size was suitable for obtaining an adequate thickness homogeneity of at least 5%. The results of the simulation are reported in Figure 37.

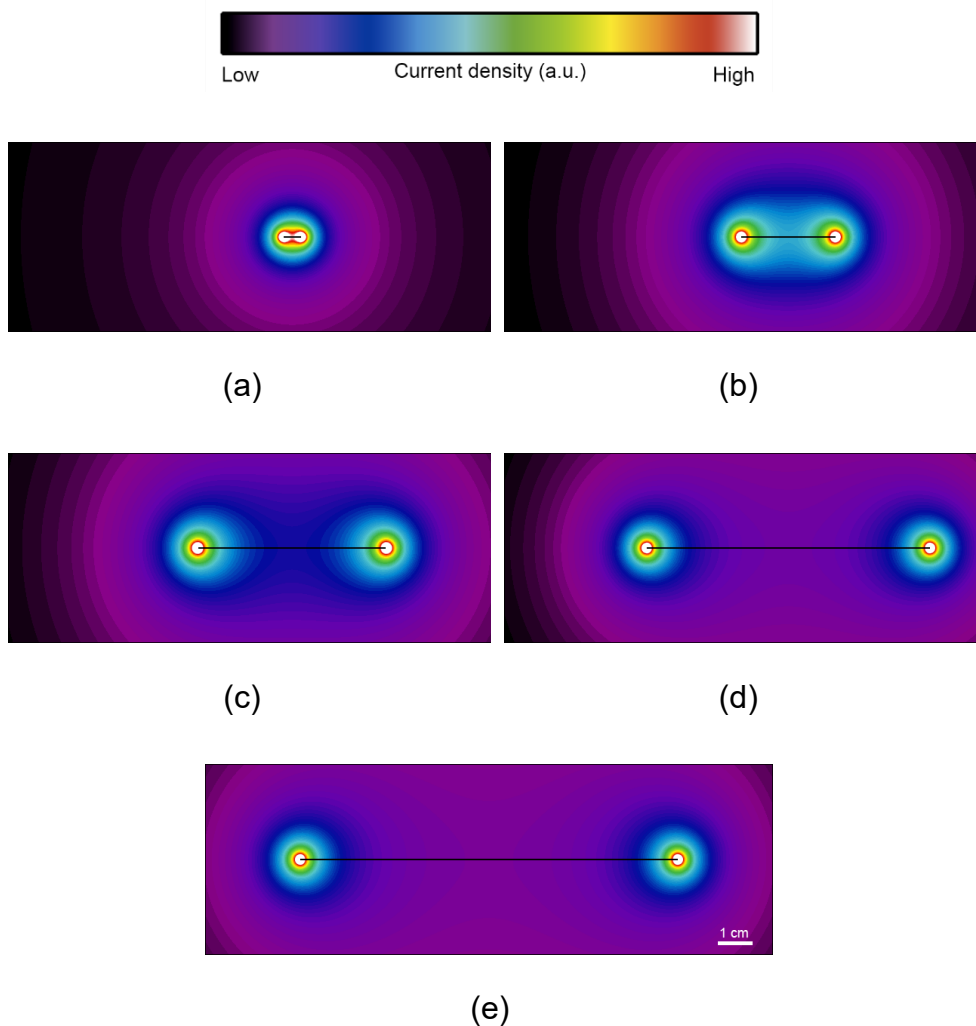


Figure 37: Results of current density simulations. A magnification of the cathode area ($15 \times 5 \text{ cm}^2$) of the $50 \times 50 \text{ cm}^2$ ($200 \mu\text{m}/\text{px}$) simulation is shown. Cathode length: a) 0.5 cm; b) 2.5 cm; c) 5.0 cm; d) 7.5 cm; e) 10.0 cm.

The current density profile near the cathode surface for the different cathode sizes is compared in Figure 38a, showing the exponential trend due to the edge effect. The values are normalized to 1 with respect to the minimum value. **Error! Reference source not found.** An enlarged view is shown in Figure 38b to compare the degree of uniformity achievable for different cathode

lengths. The horizontal line at 1.05 a.u. outlines a thickness variation of 5 % since certified reference standards are commonly supplied with thickness distribution not exceeding this value. Thickness profiles show that adequate homogeneity in the central region of the coatings, with an area of 1 cm², could be achieved for lengths starting from 5 cm. Therefore, using a 10 cm x 7.5 cm plate as a substrate in the center, we will most likely obtain a sufficiently uniform deposit to be analyzed with a spectrophotometer with a 1 cm diameter collimator.

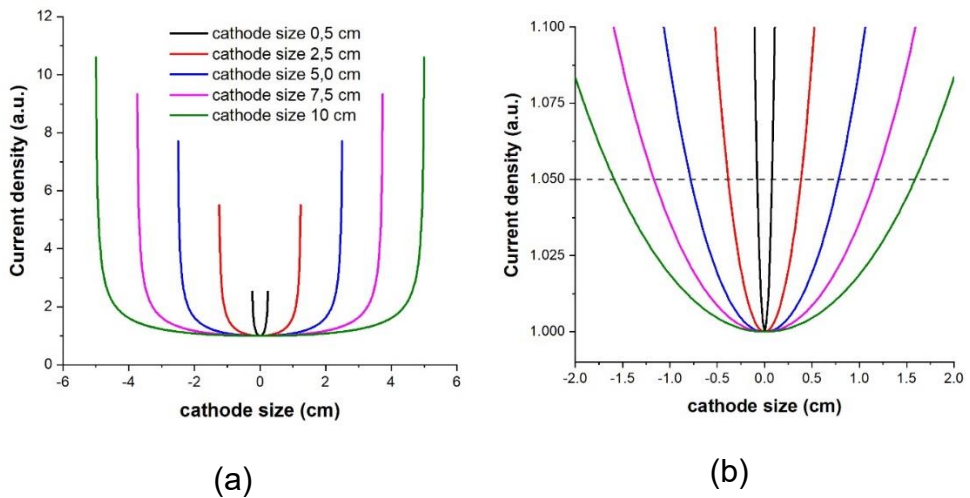


Figure 38: Normalized current density profiles near the cathode surface for different cathode size. In the inset an enlarged view.

2.3.2 XRF measurements

2.3.2.1 Deposit thickness distribution

Each plated sample's surface was divided into squares of side 10 mm with a permanent marker, obtaining a 7 x 10 matrix of points (Figure 39a). Ni K X-ray line net counts of spectra collected for each grid point were used to create surface plots representing thickness distributions. The uniformity map (Figure 39b) was plotted using the normalized net counts instead of the actual thickness since this is a directly measured quantity and is not influenced by the quantification algorithm. The measurements were not performed on the corners because of the presence of holes to secure the sample to the plating frame. From the maps, it is possible to notice that the deposit is not always perfectly centered. This is due to the binding of the sample, which is not completely orthogonal with respect to the anodes, and to the movement of the frame during the deposition.

Nevertheless, the data shows that for each coating can be identified, a central portion of at least 100 mm² where thickness variation falls within 5%.

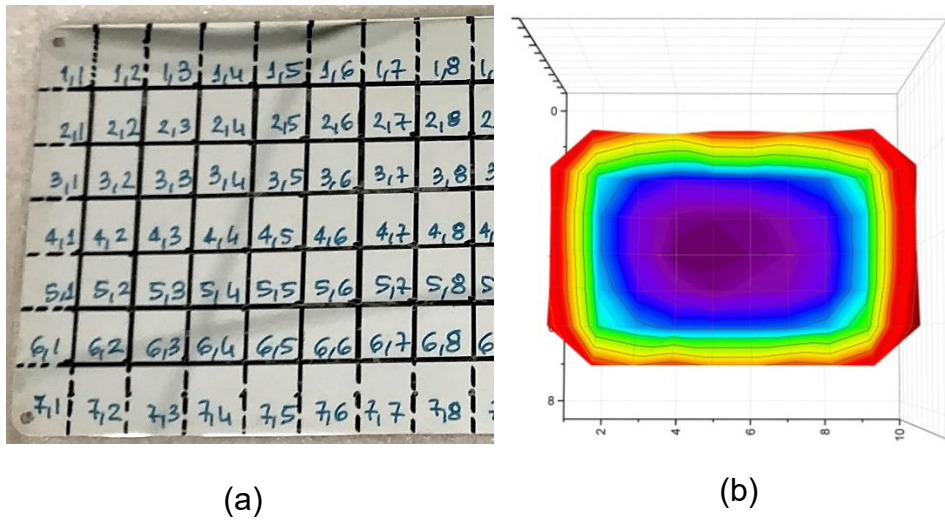


Figure 39: XRF mapping of sample 1A: a) The actual sample divided in the sector for XRF analysis; b) Contour plot of the normalized intensities obtained from the XRF measurement.

We compared the experimental data for sample 1C to those predicted from the current densities simulation, both normalized by their minimum values (Figure 40). Data of the shortest size (7.5 cm) in the center of the sample are reported. The XRF data were centered for a better comparison. The current density profile and XRF intensity are in satisfactory correlation. Thus, despite the simplified approach, ICD2D aids in the qualitative prediction of the 1-dimensional thickness distribution of electroplating processes.

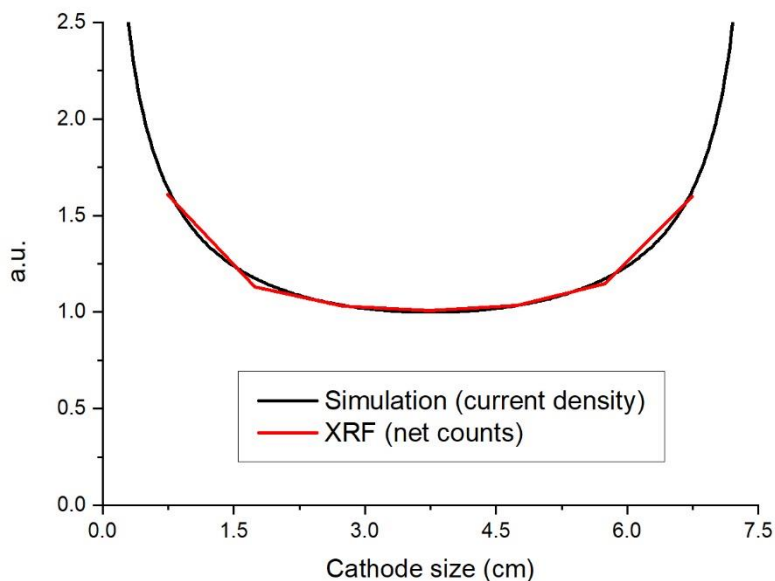


Figure 40: Comparison between simulated current density (normalized) for 7.5 cm cathode size and XRF net counts (normalized and centred) of sample 1C along the short size (7.5 cm).

2.3.2.2 Galvanic deposition reproducibility

After the thickness uniformity evaluation of each sample, coatings of correspondent plating times were compared to gain insights into manufacturing process reliability. Self-produced standards can be used with confidence only if the plating process demonstrates high reproducibility. This study was accomplished using FP with one-point empirical correction. Results obtained for central squares were reported in Figure 41. Thicknesses data agree with each other, with SD not exceeding 0.2, proving that electroplating has, at least, in this case, excellent reproducibility.

On the other hand, the obtained thickness values were far from the expected nominal ones. The deposition rate of the bath was attested to be approximately 0.3 $\mu\text{m}/\text{min}$ with respect to the presumed 0.6 $\mu\text{m}/\text{min}$. This

discrepancy can be caused by many factors: the electroplating bath was not fresh because part of an industrial process; the power supply was not well sized for such small samples being designed for industrial applications and delivering hundreds of amps. Nevertheless, most likely, the declared efficiency of the bath takes into account the average deposition thickness. At the same time, as demonstrated with simulations and XRF measurement, the edge effect has a significant impact on the coating distribution. For this reason, to use the samples as a standard it is necessary measuring the real thickness with a cross-section, as done in this study, or to perform an accurate evaluation of the bath efficiency in the area of interest by differential weight measurement.

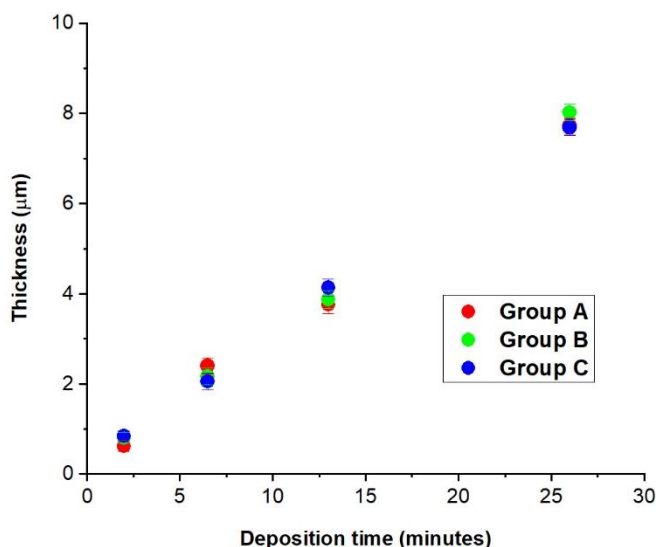


Figure 41: Comparison between thicknesses of different groups.

2.3.2.3 LM and SEM-EDS cross-sectional thickness measurement

Cross-sections obtained from A samples in the 1 cm central portion, according to standard protocols [7], were analyzed by reflected-light microscopy (Figure 42) and SEM-EDS (Figure 43). Regarding LM, thickness results are based on 15 readings taken from 5 fields of view for each sample.

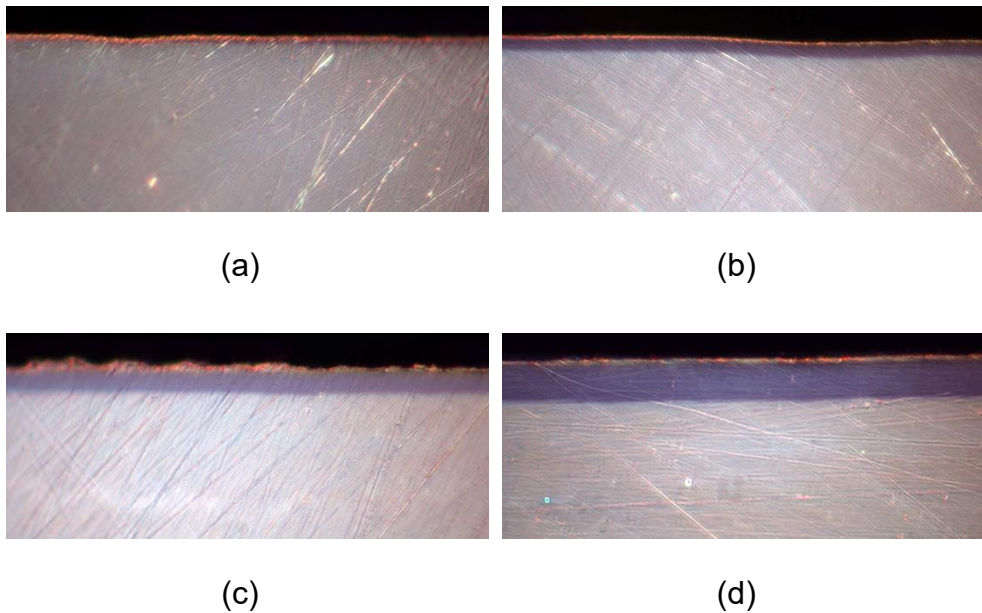
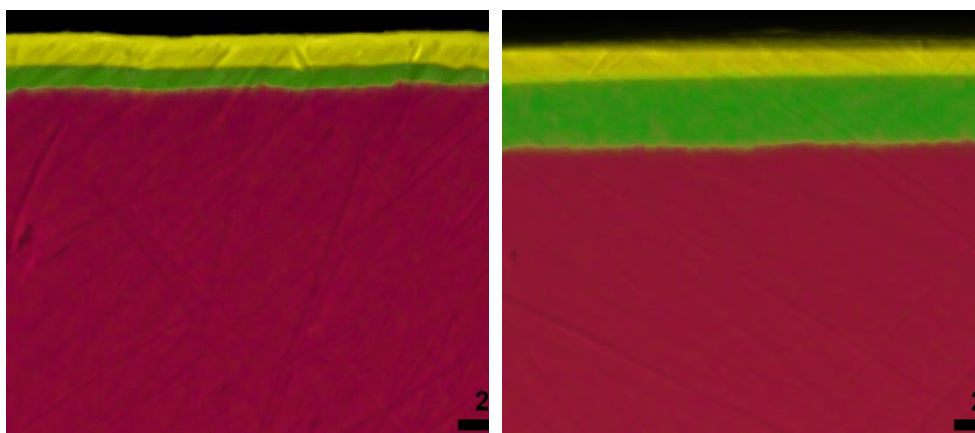


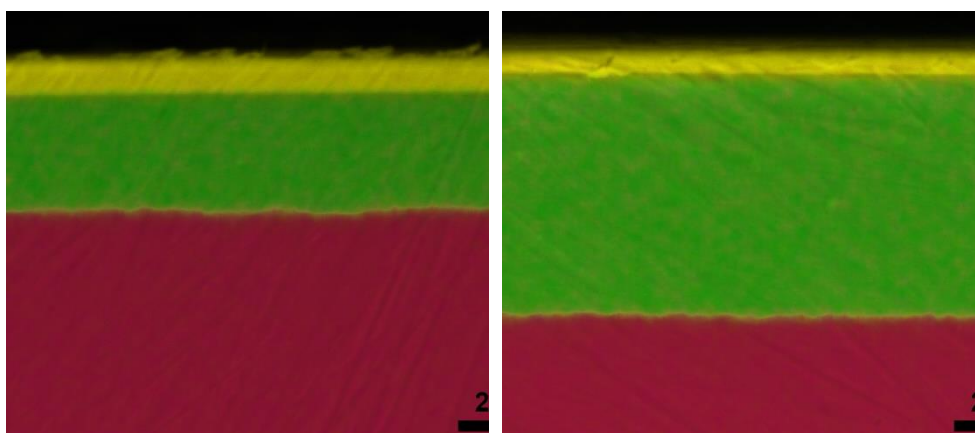
Figure 42: Cross section light microscopy analysis of samples a) 1A, b) 2A; c) 3A; d) 4A.

SEM thickness determination were performed as a combination of secondary electrons, backscattered electrons and EDS maps. By examining elemental distributions within cross-sections, thicknesses were calculated indirectly. Readings were repeated three times at different locations.



(a)

(b)



(c)

(d)

Figure 43: Cross section SEM-EDS analysis of samples a) 1A, b) 2A; c) 3A; d) 4A.

Thickness data for both the LM as well as the SEM-EDS methods are compared in Figure 44. The results obtained with the two techniques are in good accordance.

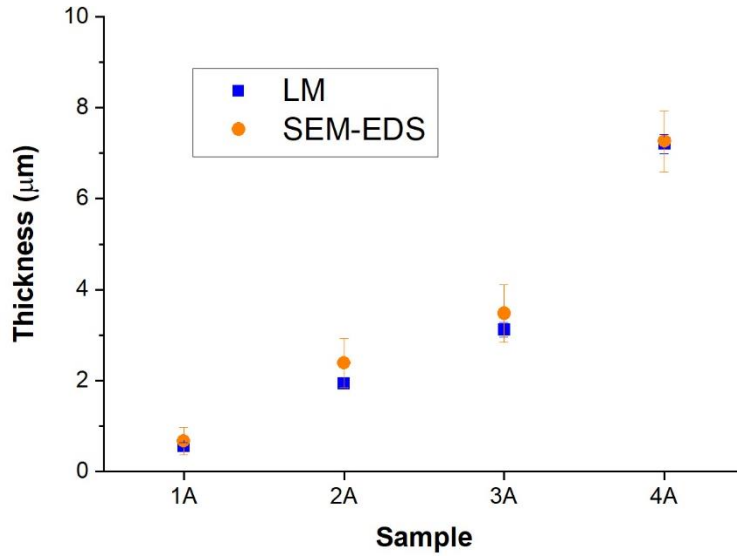


Figure 44: Comparison between LM and SEM-EDS analysis of the group A cross-section samples.

2.3.2.4 XRF Thickness measurement comparison

It is well known that electron microscopy techniques have higher lateral resolution than light microscopy. Therefore, thickness data obtained by SEM-EDS analysis of A series samples were chosen to build a 5-point calibration curve (Figure 45), expressed by the equation (21):

$$d = a * \log\left(\frac{b - I}{c}\right) \quad (28)$$

Where d is the film thickness, I is the XRF intensity and a , b and c are the fitting parameters.

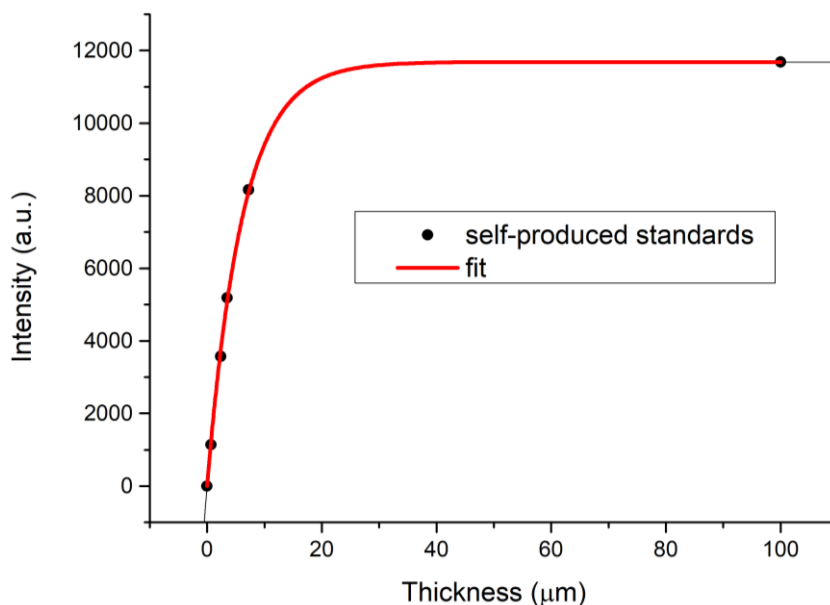


Figure 45: Calibration curve obtained with the self-produced standards.

Another calibration curve was built using a 10 μm certified thickness standard in a semi-fundamental parameter approach (FP with one-point empirical correction). The infinitely thick point was set arbitrarily to 100 microns in both cases since secondary X-ray emission saturation of nickel was reached for thicknesses over 30 microns [27]. Then, the results were compared with standardless FP, certified standard FP with one-point empirical correction, and the self-produced standards. Finally, coatings thickness in the central portion of B and C group samples were determined using the three different XRF quantification methods (Figure 46). As highlighted by the column chart, the thicknesses obtained from the methods with calibration curves agree with each other for all the samples. Conversely, the standardless method was much less precise revealing differences in thickness estimation that grew as thickness increased.

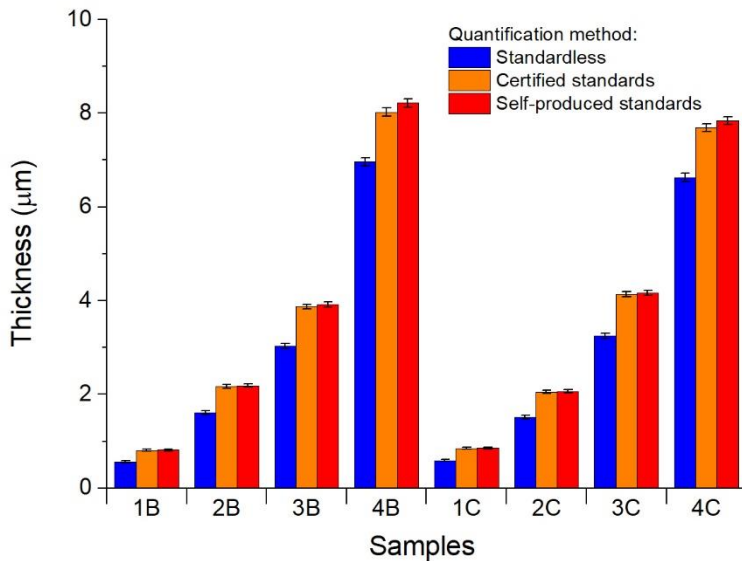


Figure 46: Comparison between different quantification methods of B and C group samples in the central region.

2.4 Conclusions

This paper presents a novel protocol for XRF thickness measurement of metallic films based on self-produced standards. Maps resulting from nickel Ka net counts show a thickness variation within 5% for the central portion of samples, consistent with certified standards specifications, and sufficiently homogeneous, compared to the typical sizes of X-ray beam collimators (ranging from 50 microns up to 10 mm). The approach was validated by comparisons with findings obtained for different quantitation methods. Notably, the proposed protocol was much more accurate than standardless FP and almost as effective as the certified standard-based method. Besides, it is also shown that considering only primary current distribution, it is

possible to predict almost qualitatively coatings thickness distribution for flat surfaces to obtain the dimensions that the substrate must have to give a sufficiently homogeneous measuring area.

Furthermore, we demonstrated that samples properly made following this procedure by choosing the proper substrate geometry can be successfully used as a standard. Furthermore, since the galvanic process is extremely cheap, it is possible to realize numerous standards with variable thickness, composition, and succession of layers, overcoming the limitation of using a few certified standards due to their high cost. Therefore, this protocol reduces costs associated with XRF instrument calibration without major drawbacks in measurement accuracy.

2.5 Addendum

Another approach to the self-production of XRF thickness calibration standards is based on the apparatus reported in the figures at the end of this section. The rationale is obtaining ready-to-use standards for XRF spectroscopy empirical calibrations directly in the plating line. The assembly is, therefore, equipped with a hook (not shown in the figures), which allows for being fixed on the cathode busbar. The system is designed to minimize edge effects; the circular symmetry along with an ideally flat and continuous conducting surface, should ensure a uniform thickness distribution within the central portion of the cathode, which can be removed and used as the XRF thickness standard.

The equipment has been designed for an industrial scale, direct current decorative nickel electrodeposition process. However, some minor adjustments allow its employment in different plating scenarios.

The apparatus has been designed relying on finite element simulations as described in the following paragraphs.

2.5.1 Introduction

2.5.1.1 Finite Element Method

The finite element method (FEM) is an umbrella term referring to a set of numerical techniques that give approximate solutions to complex space- and time-dependent phenomena. Physical laws describing such problems are generally expressed as partial differential equations (PDEs). Except for simple cases, these PDEs cannot be solved with analytical methods. Instead, the equations can be approximated, typically breaking the problem down into smaller regions, i.e., the finite elements. Over the so-called “mesh,” made up of such smaller domains, the unknown variables (e.g., temperature, velocity, etc.) are approximated using known functions; these functions are polynomials that can be linear or higher-order expansions based on the geometrical locations of a few points (nodes) used to define the elements shape. In other words, by FEM, the governing equations are integrated over each finite element, and contributions are summed over the entire problem domain; as a result, a set of finite linear equations is obtained. Solutions to these equations can be achieved by linear algebra techniques.

2.5.1.2 FEM in Electrochemistry

Electrochemical processes are governed by the coupling of the conservation of charge and current within the electrochemical system, as well as the conservation of mass for each chemical specie in the electrolyte. In addition, the conservation of momentum and the total mass are also required to predict the fluid flow. PDEs are typically used in the mathematical rationalization of these phenomena. Therefore, an electrochemical theory is developed by solving such PDEs on a suitable geometry and timescale. However, as already stated, these PDEs cannot be solved with analytical methods for most geometries and problems. Therefore a computational solution is required [28].

In the most general case, charge conservation obeys Gauss's law (Eq. 22), and mass transport obeys the Nernst–Planck equations (Eq. 23, for an ideal solution) subject to mass continuity (Eq. 24):

$$-\nabla \cdot (\varepsilon \nabla \varphi) = \rho \quad (29)$$

$$\mathbf{N}_i = -D_i \nabla c_i - z_i u_i c_i \nabla \varphi + c_i \mathbf{u} \quad (30)$$

$$\frac{\partial c_i}{\partial t} + \nabla \cdot \mathbf{N}_i = R_i \quad (31)$$

Where:

- ϵ is the permittivity (F m^{-1});
- φ is the potential (V);
- ρ is the charge density (C m^{-3});
- c_i is the concentration of species i (mol m^{-3});
- \mathbf{N}_i is the flux of species i ($\text{mol m}^{-2} \text{s}^{-1}$);
- D_i is the diffusion coefficient of species i ($\text{m}^2 \text{s}^{-1}$);
- z_i is the charge number of species i ;
- u_i is the mobility of species i ($\text{m}^2 \text{V}^{-1} \text{s}^{-1}$);
- u is the bulk velocity (m s^{-1});
- R_i is the mass source of species i ($\text{mol m}^{-3} \text{s}^{-1}$)

Together, these are the Nernst–Planck–Poisson equations: an entirely general description of an infinitely dilute electrolyte solution's charge and mass transport properties. In addition, boundary conditions can describe electrolysis occurring at the electrode's surface and the adsorption of chemical species. Finally, homogeneous reactions, and electrolysis in porous electrodes, contribute to the mass source.

The Nernst–Planck–Poisson equations are highly nonlinear and exhibit multiple lengths and time scales. Therefore, their complete solution for real systems is often unfeasible, and simplifications must be sought. Assuming

electroneutrality for the bulk solution, the electrolyte can be considered an Ohmic conductor.

The higher the supporting electrolyte's concentration (compared to the electroactive specie one), the higher the conductivity; therefore, the electric field tends towards zero for a given current. Above suitable values, the electrolyte concentration can be assumed as "infinite"; it follows that migration can be neglected and the mass transport is governed only by diffusion as expressed by Fick's 2nd law:

$$\frac{\partial c_i}{\partial t} = D_i \nabla^2 c_i - \mathbf{u} \cdot \nabla c_i \quad (32)$$

2.5.1.3 Electrodeposition simulation with COMSOL Multiphysics®

Despite the significant research progress in FEA of electrodeposition, the application of finite element simulations in industrial plating process design still needs to be widely accepted. Concerning that point, it is undoubtedly true that simulating electrodeposition processes is a complex and multi-disciplinary task. Furthermore, experimental parametric studies for improving understanding of a particular plating process are time-consuming and scarcely reproducible. The combined effect of parameters, such as plating time, current density, charge transfer coefficients, etc., has yet to be systematically analyzed and quantified for complex-shaped items.

As the name suggests, COMSOL Multiphysics® is designed for multiphysics, meaning developing a model that considers all involved physical phenomena expressed as PDEs. Metal electrodeposition is indeed an example of a "multiphysics" problem, incorporating diverse physical phenomena, such as fluid dynamics, mass transport, heat transfer, and charge transfer.

Simulations can provide physical insight and predict thickness distribution by accurately describing all relevant phenomena.

2.5.2 Numerical simulation

Several FEM simulations have been carried out before realizing the apparatus (see figures at the end of the section) to (a) dimension the cathode for obtaining a narrow thickness distribution in the removable component and (b) to evaluate its behavior on varying process parameters.

To simplify the calculation, the following basic assumptions has been made:

- The potential distribution on the metal electrode is constant (the metal anode and cathode have very high conductivity).
- The change of activation overpotential is caused by the electrolyte potential on the electrode surface, so the metal electrode is treated as the boundary.
- The solution is regarded as incompressible Newtonian fluid in an electroplating bath.
- The only electrode reactions on the cathode and anode are, respectively, nickel deposition and dissolution.

Moreover, all the cases are modeled by neglecting concentration overpotential.

To have the bulk electrical conductivity of the electrolyte as independent variable in the parametric study, secondary current distribution has been employed in lieu of the tertiary one, i.e., no concentration overpotentials

have been considered. Including electrolyte mass transport explicitly in the analysis is much more computationally demanding since Nernst–Planck equations become nonlinear. Nevertheless, considering the high metal concentration and agitation efficiency, it is reasonable to assume minor concentration gradients for electroplating baths. Therefore, electrolyte conductivity is set as constant, and neither convection nor diffusion has been modeled (electrolyte is considered at rest).

Concentration-independent Butler–Volmer equation is thus adopted to compute the local current density on the cathode. A value of $1 \text{ e-}2 \text{ A/m}^2$ has been set as exchange current density, i.e., both ohmic factors and charge transfer controlled overpotential kinetic effects are considered (Wagner number > 1).

Other parameters have been taken from the real-world experiment reported in the previous sections. For the reader’s convenience, are listed below:

- Rectangular shaped plating tank.
- Potentiostatic condition.
- Plating solution conductivity: 91,3 mS/cm.
- Diameter of removable part of the cathode: 20 mm.

A fine triangular mesh has been used as represented in figure 48.

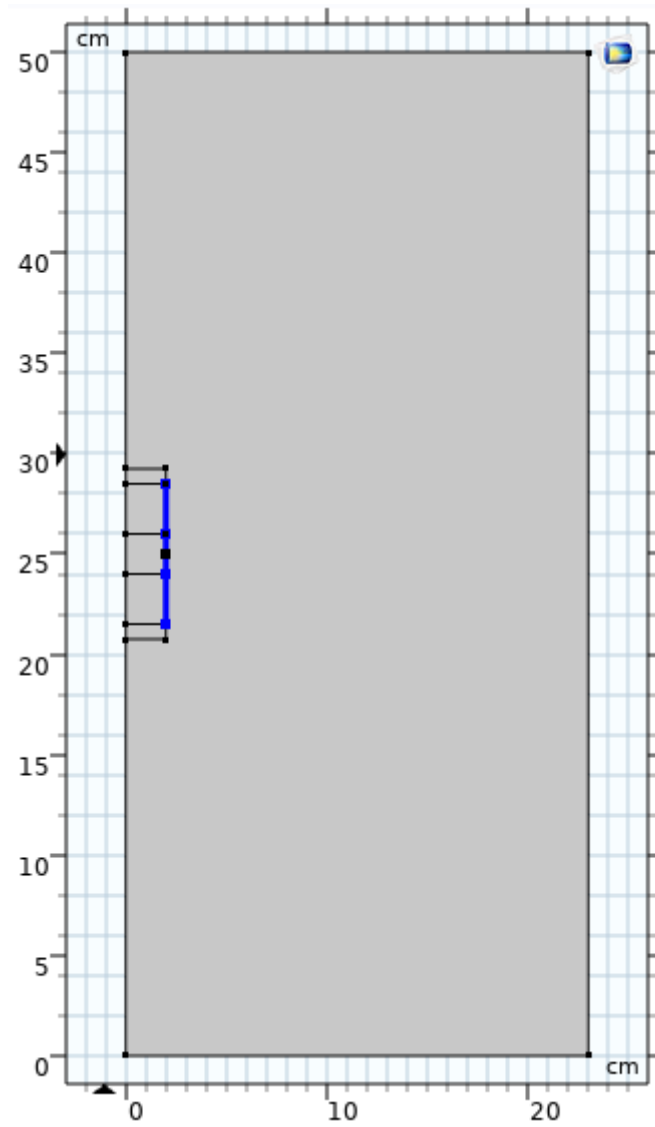


Figure 47 Two-dimensional geometrical model of electroplating cell. The blue line represents the cathode active surface area. The anode corresponds to the opposite side of the rectangle.

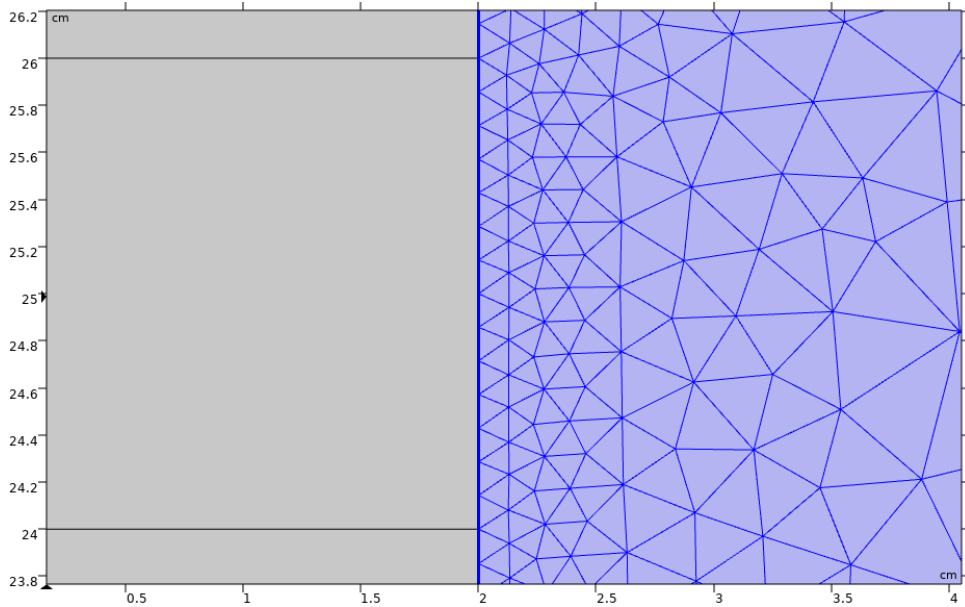


Figure 48 Detail of the two-dimensional mesh- Elements are triangle consisting of three vertex nodes.

2.5.3 Results and Discussion

Three cases were numerically solved, and the results are shown below.

Figure 49 shows results for five different cathode diameters: 35, 70, 130, 190, and 250 mm. As previously stated, values are referred to total cathode size, while the inner concentric portion, i.e., the removable one, is fixed to 20 mm in diameter. As seen from the graph, the green line corresponding to a 70 mm cathode shows a change in current density of less than 5-point percent with respect to the mean value of the current density. Therefore, this value is a good trade-off between usability and performance. Accordingly, the following simulations have been carried out considering only a cathode size of 70 mm.

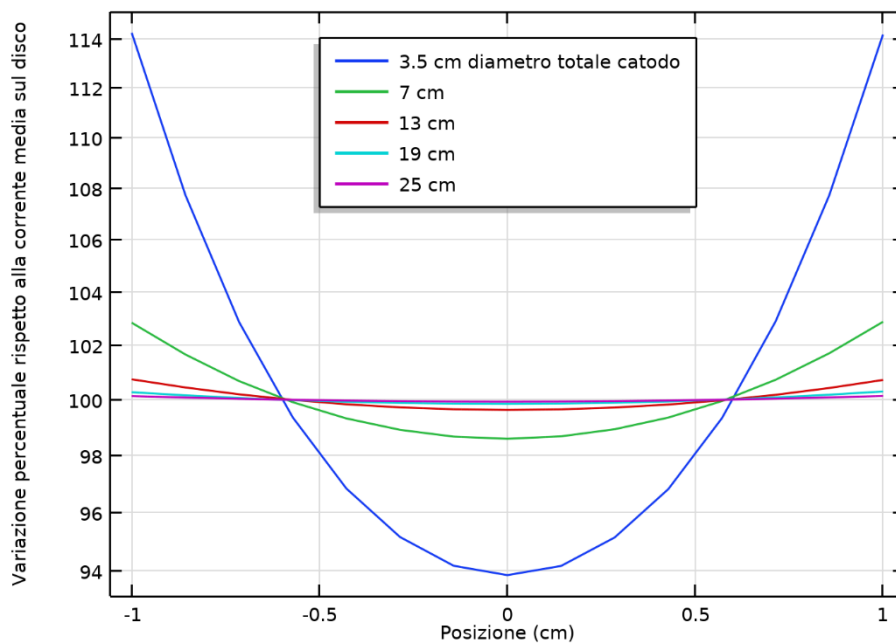


Figure 49

Figure 50 shows results for different anode sizes: 350-, 500-, and 650-mm values have been chosen to have at least a cathode-to-anode ratio of 1:5, fixing the distance to the cathode at 230 mm. Current densities are normalized with respect to the total current on the whole surface of the cathode (70 mm in diameter). As can be seen, the trend is almost the same. The shifting of the curves means that as the anode size decreases, the current lines tend towards the outer part of the cathode, diminishing the current on the central one.

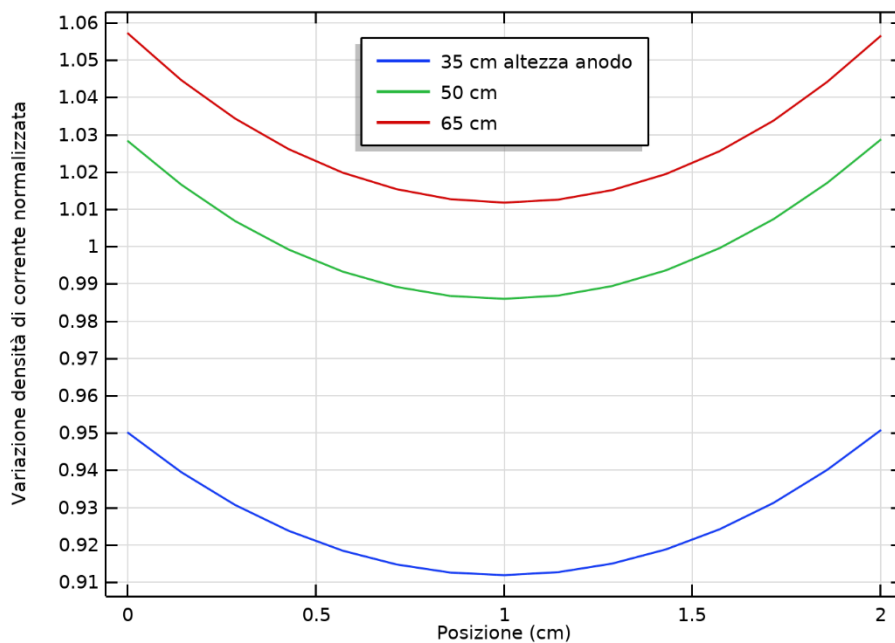


Figure 50

Finally, the effect of the cathode-to-anode distance has been studied. Also, in this case, current densities are normalized to the total current on the whole surface of the cathode (3850 mm ca.). Figure 51 shows that the higher the anode distance, the lower the current density; the ohmic loss within the electrolyte can account for this trend.

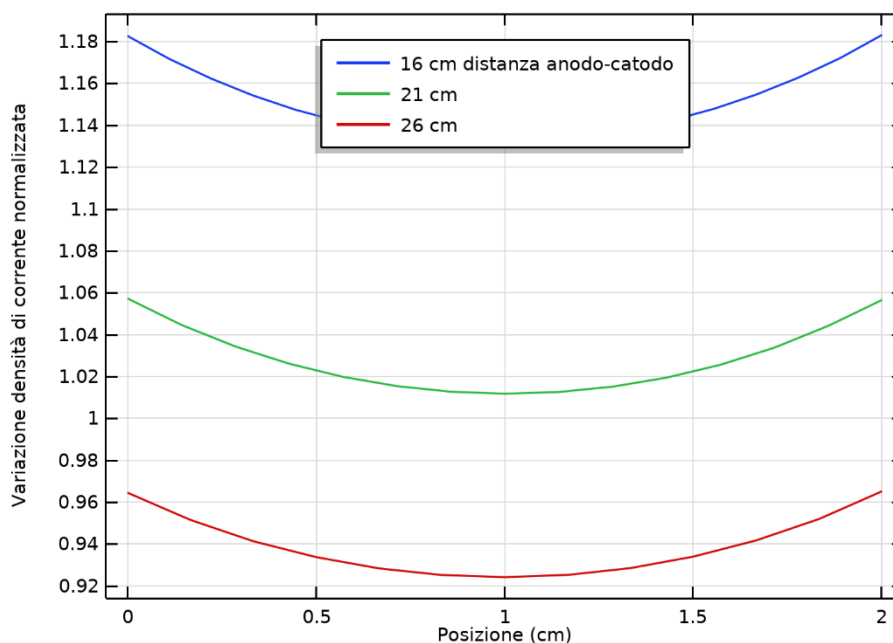


Figure 51

2.5.4 Conclusions

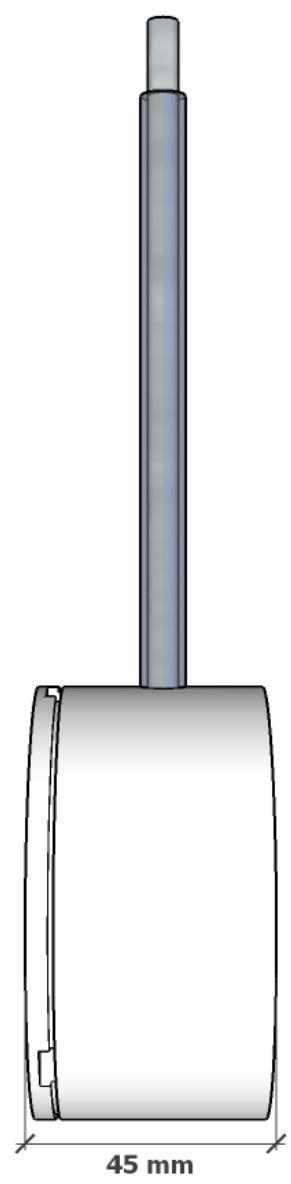
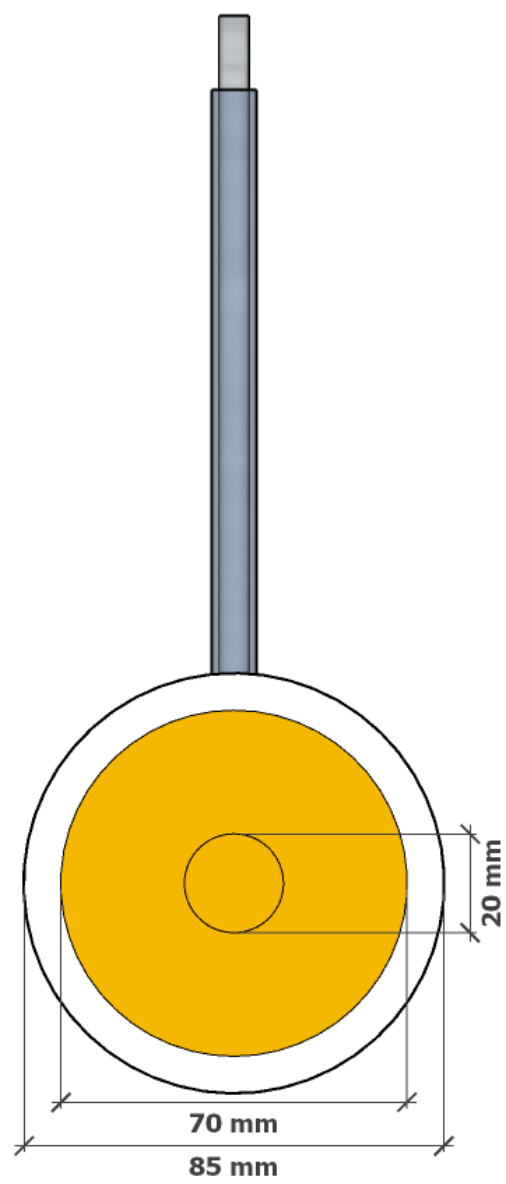
To conclude, simulations demonstrate that a cathode size of 70 mm in diameter with a central removable part is a suitable choice.

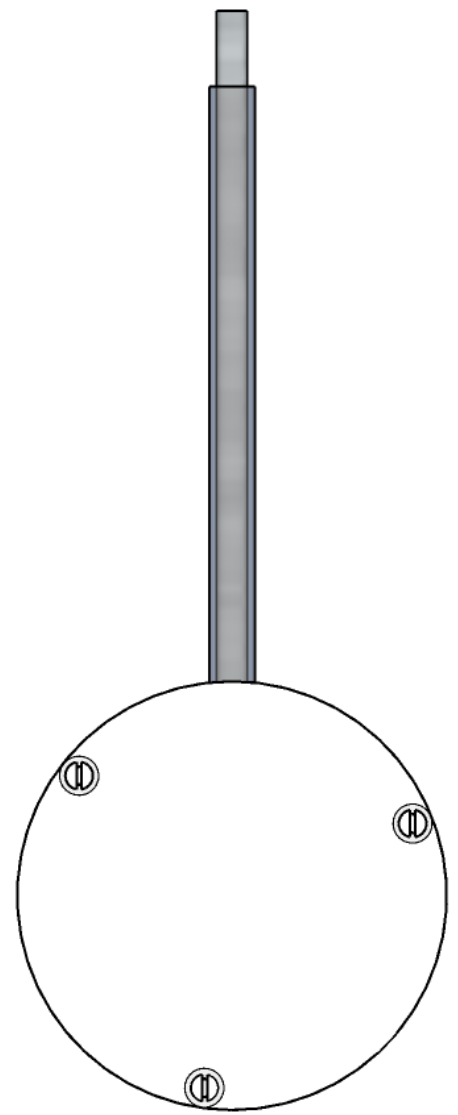
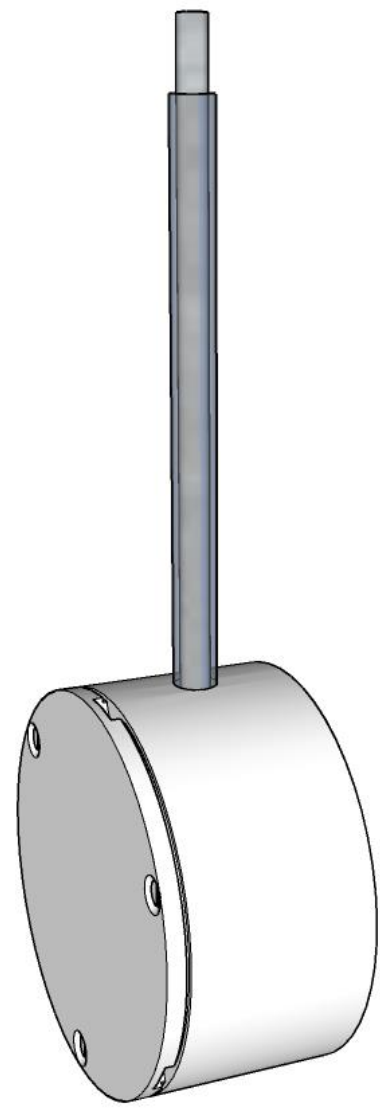
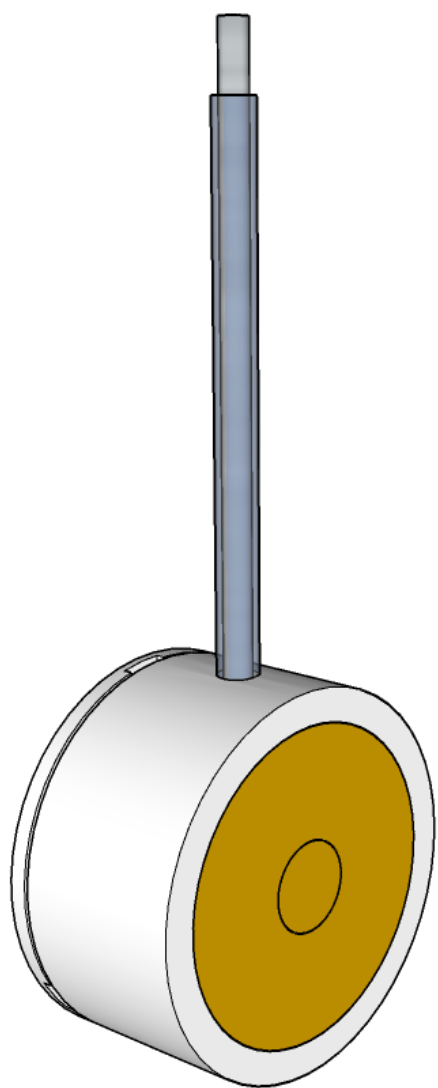
On this basis, the equipment has been realized, as shown in the following figures.

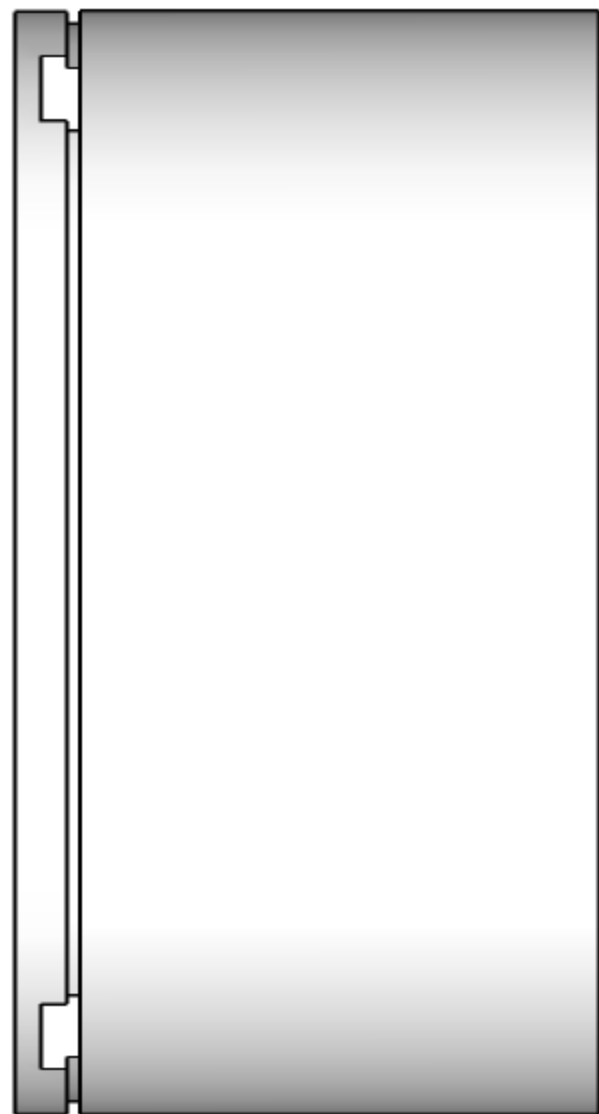
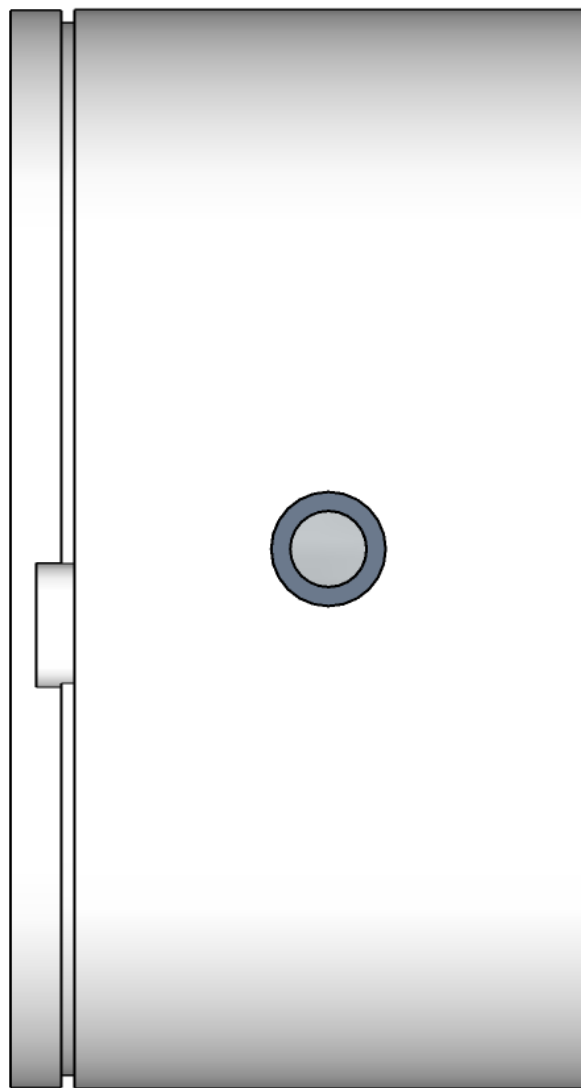
The cathode is made of brass, one of fashion accessories' most common starting materials. The cathode is inserted in a High-density polyethylene (HDPE) frame. HDPE is, in fact, an inexpensive, easy-to-work, and chemically-resistant material. Viton® O-rings are used to seal all fittings. A glass tube, finally, isolates the stainless-steel rod, by which all the assembly is fixed to the cathode's busbar.

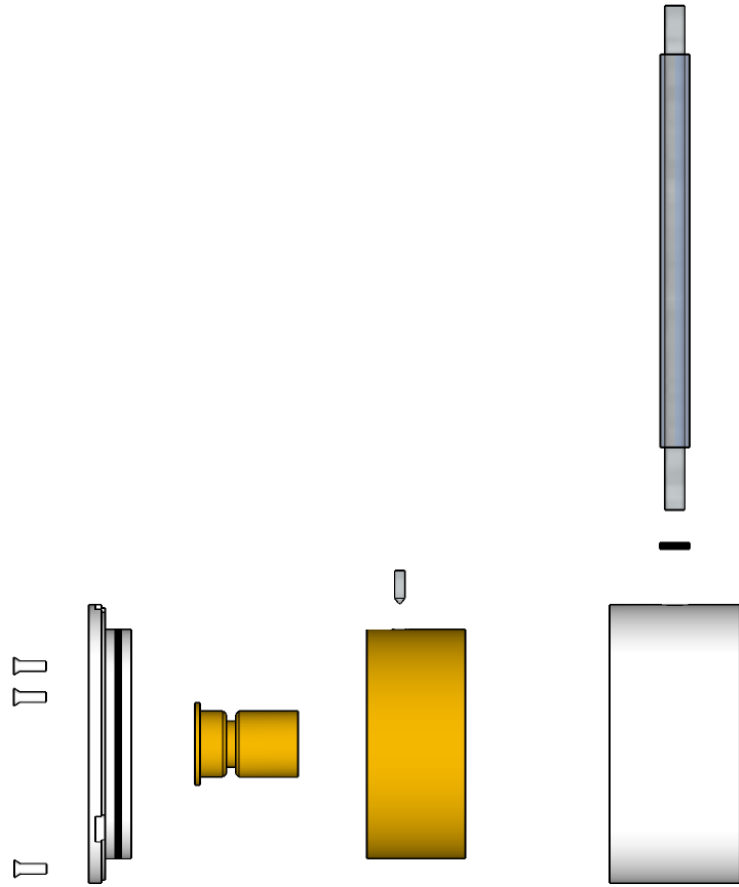
Technical drawings and images of the device are shown on the following pages.

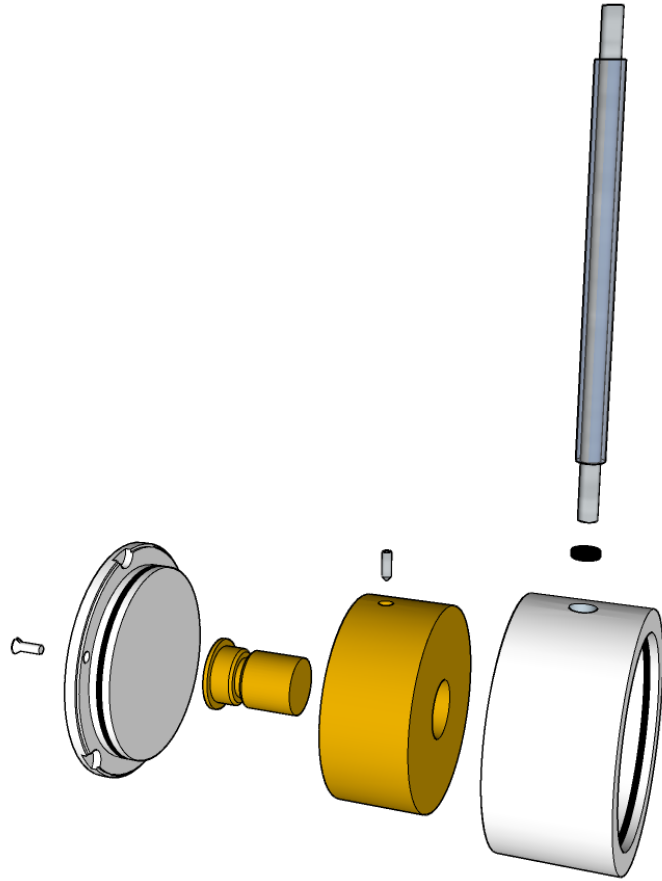
133

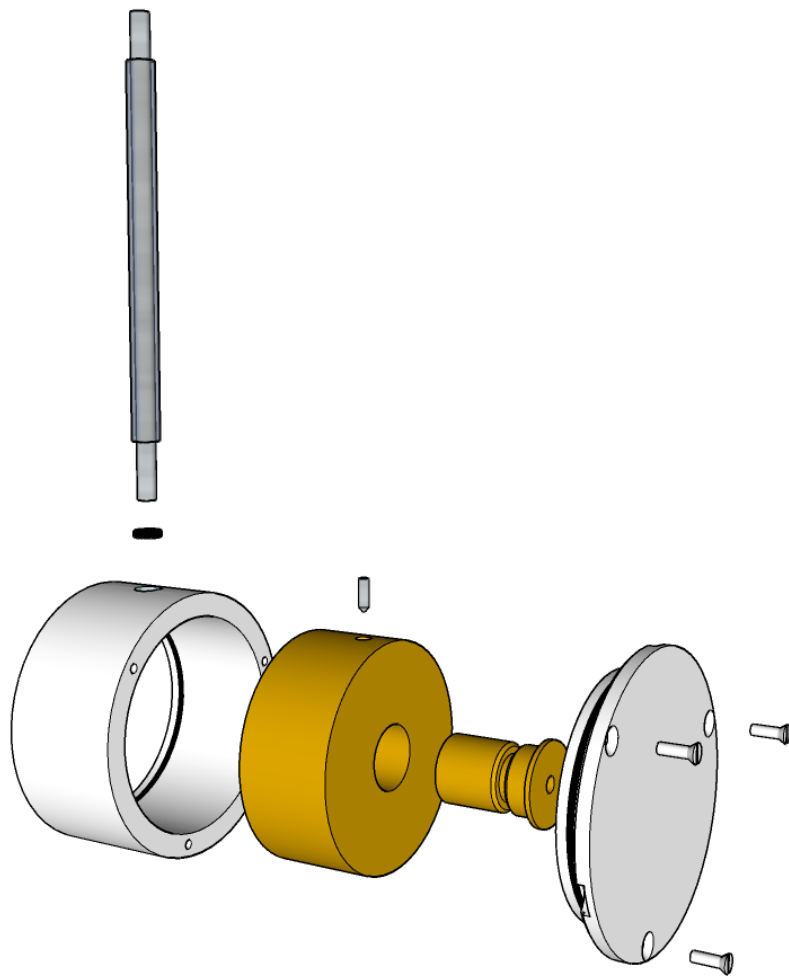


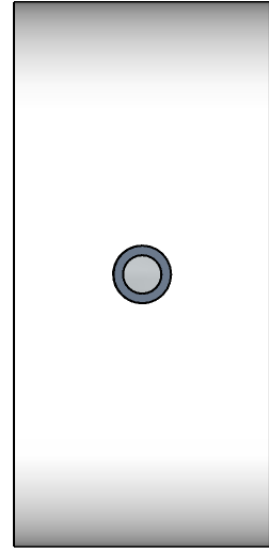
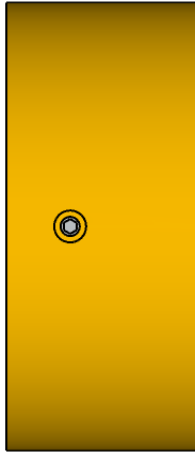
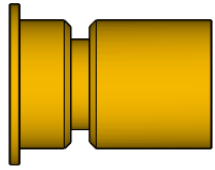
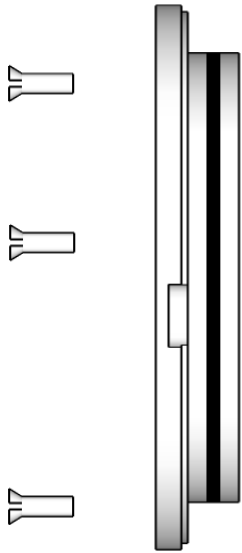
















Section 3

3 Electrodeposited white bronzes on brass: corrosion in 3.5% sodium chloride solution

3.1 Introduction

White bronzes are electrodeposited coatings consisting of Cu-Sn-(Zn). Recently, they have found an extensive application as an alternative to electroplated Nickel [29–33]. Together with Ni coatings, they share excellent corrosion and wear resistance. For this reason, white bronzes have been widely employed as intermediate layers in applications that require stability of appearance (long-lasting brightness and no change of color in time), e.g., in fashion goods. Furthermore, white bronze coatings are also good electric conductors that are hard to oxidize, even in an aggressive sulfuric environment [34,35]. For these properties, they have been proposed as a viable alternative to bare Cu or Zn coatings for the protection of electric and electronic components for automotive [36,37]. Moreover, a significant research effort on ternary white bronzes deposition has been recently deployed. These materials are valuable precursors for synthesizing kesterite (CZTS, $\text{Cu}_2\text{ZnSnS}_4$) semiconductors, enabling the fabrication of photovoltaic cells with only earth-abundant materials and more than 10% efficiency [34,35,38–41].

While kesterite precursors are usually deposited from acid electrolytes, the most popular solutions for white bronzes deposition are alkaline; in industrial processes, most galvanic bath employs cyanides as complexing agents [42–45]. With proper additives, cyanide electrolytes grow smooth and bright deposits with mirror-like surface finishing. Additionally, cyanide provides

performance stability and accurate control of the composition of the electrodeposited films under heavy-duty loads and long-term operations. However, cyanide's toxicity requires complex handling protocols and well-established and documented waste treatment procedures. [46,47]. This study focuses on white bronzes deposited from cyanide electrolytes.

Ternary white bronzes containing Cu, Zn, and Sn (Copper Zinc Tin, or CZT) are widely used in the electroplating industry for two main reasons: i) Zn containing bronzes have shiny surfaces even at a tin concentration significantly lower than 20% wt. [47–49] and ii) they deposit 40% faster than the corresponding Cu-Sn binary alloys [21]. Moreover, Zn-bearing coatings are usually less porous and brighter, with a nickel-like appearance that compares to the pewter-like color of binary Cu-Sn coatings [49,50]. On the other side, high tin binary bronze is harder than ternary alloys, making them a favorite choice in applications requiring scratch, wear, and erosion resistance.

Generally, CZT white bronzes show better corrosion resistance in an aqueous environment with respect to naval brasses. [31,51–53]. This behavior is due to the formation of a tin (IV) passivation layer consisting of insoluble tin oxo-hydroxides. These oxidized tin species limit the corrosion rate in non-complexing aqueous media [54]. When more than 10% of tin is incorporated, white bronzes are hard and exceed the corrosion resistance of brass. In practical applications, up to 20% and more tin is often added to improve corrosion resistance [55,56]. Electrodeposited white bronzes with 50 wt. % Cu, 25 wt. % Zn and 25 wt.% Sn still shows fast corrosion rates when in contact with the marine atmosphere [57,58], fastly uncovering the substrate materials.

This work focuses on the corrosion performance, the structure, and the morphology of two classes of white bronze deposited on brass, a CZT ternary alloy (ca. 55 %wt. Cu, 23% wt. Sn, and 22% wt. Zn) and a high tin zinc-free coating (ca. 63%wt. Cu, 36%wt. Sn, 1%wt. Pd). We selected brass as a substrate for its applications as a cheap alternative for fabricating DC and RF electronic connectors for the automotive industry and as a substrate for inexpensive accessories for the fashion industry. In both applications, the occasional contact with a NaCl-rich atmosphere may occur, generating oxidation phenomena detrimental to the functional properties. Moreover, despite the potential technical interest, limited information on the corrosion performance of electrodeposited white bronzes on brass with > 35% wt. Sn is reported in the literature. Brass protection with white bronze, especially with high-tin ones, can potentially limit degradation, preserving physical properties and extending the service life of the components.

3.2 Materials and Methods

3.2.1 *White Bronzes Electrodeposition*

Zn-bearing and Zn-free layers were deposited by galvanostatic electrodeposition (plating electronic GmbH with output 10V/10A power supply), using brass (67% Cu, 33% Zn) substrates as working electrodes (WE), and a mesh made of mixed conductive oxides as a counter electrode (CE). The CE was bent in a cylindrical shape to make contact with the cylindrical inner walls of a 1-liter beaker, while the WE was placed in the center of the vessel (distance between electrodes 5 cm, depth from the surface about 3 cm). Two different galvanic baths were used to produce the samples:

- The galvanic bath, commercialized by ITALFIMET (Monte San Savino, AR, Italy), for the production of Zn-bearing white bronze coatings. Deposits were grown using a current density of 2 A/dm² and a deposition time of 2, 4, and 6 minutes to obtain a deposit thickness of 0.5 mm, 1.0 mm, and 1.5 mm, respectively;
- A modified version of the previous bath, also produced in ITALFIMET's lab, to produce Zn-free white bronze layers. Deposits were produced using a current density of 2 A/dm² and a deposition time of 4, 8, and 10 minutes to grow the film to the thickness of 0.5 μm, 1.0 μm, and 1.5 μm, respectively.

3.2.2 FIB/SEM measurements

SEM image acquisition, ionic imaging, cross-sectioning, and EDX analysis were performed using a TESCAN GAIA 3 FIB/SEM microscope equipped with an EDAX Octane Elect Super EDX detector. The microscope hosts a 30 kV Triglav electron column and a Cobra Focused Gallium Ion Beam column. To measure the thickness of the coatings, we employed a FIB cross-section milling procedure. A protective (>1.5 μm thick) layer of Pt was applied before trench milling to avoid edge rounding (The topmost whitish layer visible in Figure 53). SEM images for morphology investigation were acquired using the in-beam secondary electron detector. In contrast, for the cross-sections, the image acquisition was performed by an in-beam backscattered electron detector to enhance the contrast between the substrate and the coatings, using both electron and ionic probes. SEM cross-section imaging was performed in immersion mode (UH Resolution mode), with an e-beam acceleration of 5 kV. EDS data acquisition was performed using a 12 kV beam

to sample only the electrodeposited layer and to permit X-ray characteristic emission of all its constituent elements (Pd, Zn, Cu, and Sn). Ionic images were acquired using a five pA Ga⁺ current accelerated at 30 kV. FIB and SEM images were collected using a 55° sample tilt. To correct the thickness of the deposited film, the real thickness was achieved by multiplying by 1/cos (35°).

3.2.3 XPS Measurements

XPS measurements were carried out on a Kratos AXIS Ultra DLD with an Al Ka monochromatic source to produce X-Rays (15 kV, 20 mA). Preliminary complete surveys of the samples were performed at 160 eV pass energy, while the high-resolution spectra acquisition was performed at pass energy of 20eV. Sputtering cycles were performed by the in-built Ar ion gun, adopting two 120 seconds cycles with an accelerating potential of 3 kV. These sputtering cycles were needed to uncover the metallic surface of the coatings, which was initially enfolded by a carbonous layer hindering the metals' determination. Data were analyzed using the dedicated software CasaXPS. Spectra were calibrated, shifting the aliphatic component of carbon to 285 eV, and mixed Gaussian-Lorentzian components were used for fitting the peaks.

3.2.4 XRD experiments

X-ray powder diffraction (PXRD) scans were acquired at room temperature with a PANalytical X'PERT PRO diffractometer, employing CuK α radiation ($\lambda=1.54187$ Å) and a PW3088/60-graded multilayer parabolic X-ray mirror for Cu radiation. The produced coatings were used directly as samples for the acquisition. The diffractograms were acquired in the 2θ range from 5.0 to 120.08, using a continuous scan mode with an acquisition step size of $2\theta=0.02638$ and a counting time of 49.5 s. The qualitative assignment of the peaks has been performed using the QualX2 software and the COD database [59]. The peak fit of the diffractograms has been carried out employing the GSAS2 software [60], holding the positions of the peaks to the ones expected from the assigned phases.

3.2.5 Color Measurements

The coated substrates' UV–vis–NIR diffuse reflectance spectrum was measured using an Agilent Cary 300 spectrophotometer equipped with a Labsphere PELA-1050 integration sphere. Diffuse Reflectance Spectroscopy (DRS) spectra were recorded in the range 340–830 nm, at a step of 10 nm, counting 0.2 s per step. The relative reflectance was calculated employing a reference sample with a standard white diffuse reflectance spectrum (Spectralon [61]). We converted the relative DRS spectra to Lab color coordinates using the “Multispectra” [62] software developed by our group and based on the color match library [63]. This procedure implements the Lab 1976 recommendation defined by CIE [64] and allows for calculating the color distances. According to Lab 1976, the difference in color “sensation” (dE) is reported in the text.

3.2.6 Corrosion Measurements

1 μm thick coatings were subjected to Open Circuit Potential (OCP) measurements using a benchtop voltmeter by periodically recording the potential between the coating surface and a Metrohm Ag/AgCl electrode. A 0.62M NaCl (3.5 wt.% aqueous solution) was used as the electrolyte for all the corrosion measurements. The pH of the solution was adjusted between 8.1 and 8.4, using NaOH to closely match seawater's pH conditions [30]. The samples were held inside a custom-made cell, exposing about 0.2 cm^2 surface to the electrolytic solution.

Polarization tests were performed using a Gamry PCI-4 300 potentiostat/galvanostat, exposing a circular surface of the sample (3.5 mm diameter) as working electrode (WE), a Pt mesh as the counter electrode (CE) and a standard calomel electrode (SCE) as a reference electrode (RE). Potentiodynamic cycles were performed using the same potentiostat/galvanostat, starting from -0.05 V vs OCP, ending at +1 V vs OCP (anodic direction), and back to -0.3 V vs OCP (cathodic direction), at a scan rate of 0.5 mV/sec. Initial OCP values were collected after 60 s.

EIS was performed on the 1 μm thick samples (Zn-free, Zn-bearing) and the brass substrate using a Parstat 2273 potentiostat. The electrochemical set-up was composed of a PAR G0097 electrode holder for the WE (exposed sample surface 1 cm^2), a Metrohm Ag/AgCl electrode as RE, and a graphite rod as CE. Tests were performed on Parstat K0047 Corrosion cell. EIS data were acquired after 1 hour equilibration in the electrolyte.

All the sample surfaces were cleaned before their use by a three-step cycle consisting in a) a first rinsing with acetone, b) a second rinsing with

isopropanol, c) a third rinsing using ultra-pure water, and d) a final drying using a nitrogen flux.

3.3 Results and Discussion

3.3.1 SEM investigation

3.3.1.1 Surface Morphology

Figure 52 reports the SEM images of representative samples investigated in this study at high magnification. Zn-free images show features with sizes of less than 50 nm. Such nanostructures result from the addition of polyalcohol brightener that inhibits crystal growth, favoring small crystallite size and resulting in a surface roughness much smaller than the wavelength of light. [47,65–67]. The Zn-bearing bronze films, in contrast, show much less evident nanostructures. In particular, the surface appears covered by an incoherent layer that, if kept under the electron beam, quickly changes shape, suggesting high carbon contamination that cannot be removed from the surface (the topic will be explored in detail in the XPS section). This is due to the different chemical nature of the brightening agents used in the two electrolytes, which lead to more surface impurities in the Zn-bearing bronzes, partially hiding the metal surface at high magnification.

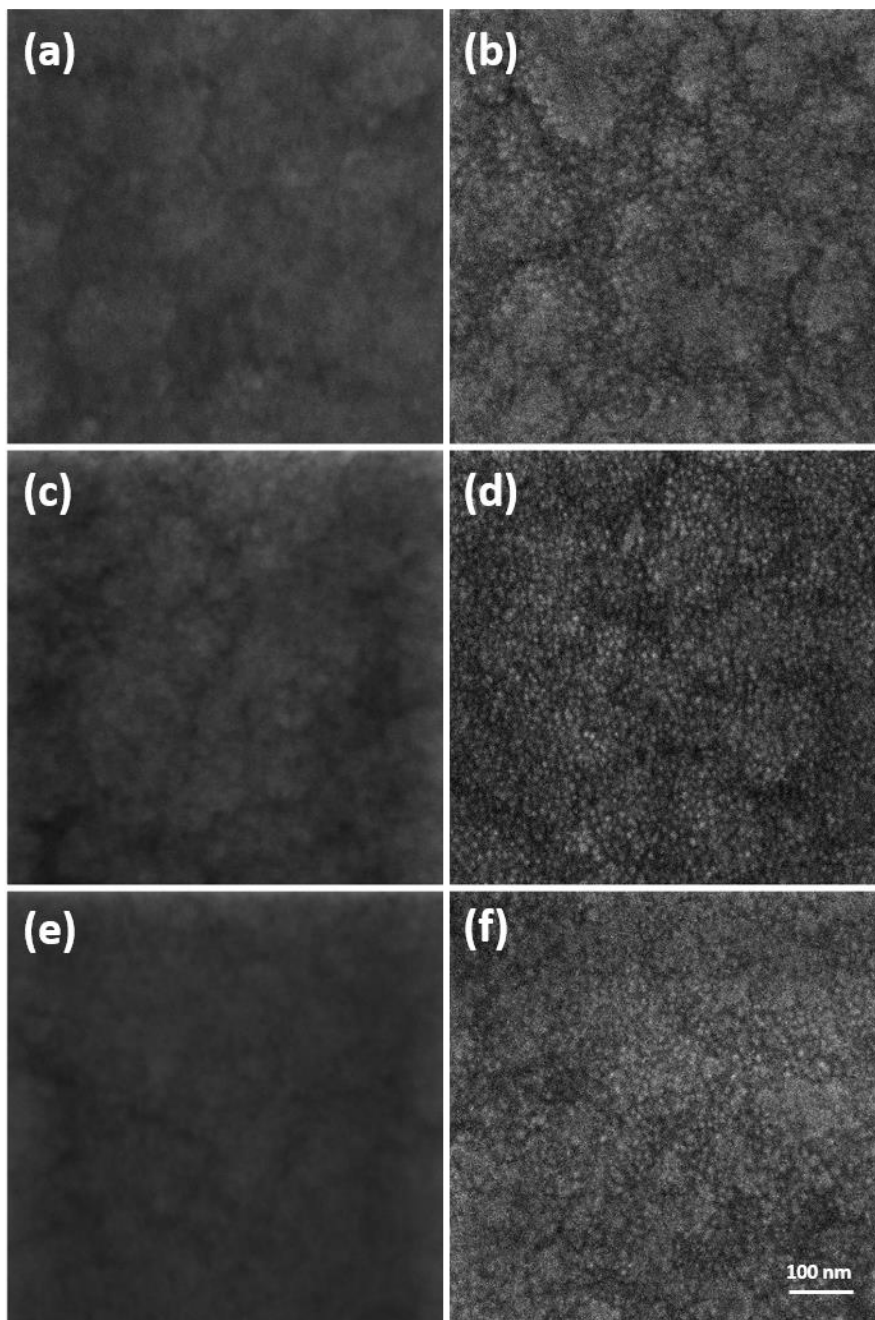


Figure 52 - 400kx SEM images of the surface morphology of Zn-bearing white bronze (a,c,e, left column, respectively 0.5, 1.0 and 1.5 μm thick), and Zn-free white bronze (b, d, f, right column, respectively 0.5, 1.0 and 1.5 μm thick).

3.3.1.2 Coating Thickness

The coating thickness was measured by cross-sectioning with a Ga⁺ ion beam in the FIB-SEM and imaging the cross-sections with primary electrons for optimal phase contrast. Pictures taken from the samples with a nominal thickness of 1.5 μm for both the Zn-free and Zn bronzes are reported in Figure 53; the topmost coating visible in both images is the deposited Pt protective layer, usually adopted to prevent edge rounding during FIB machining.

The measured thickness was in good agreement with what was expected from the settings of the electrodeposition experiments for the Zn-free series. Minor variations between nominal and experimental thicknesses were observed for Zn-bearing white bronze coatings, especially for thicker deposits. Additionally, slight differences in thickness and morphology were observed between the Zn-free and Zn-bearing samples (*Table 2*). This was essential for comparing the corrosion resistance of the two coatings.

<i>Nominal thickness (μm)</i>	<i>Zn-bearing White Bronze measured thickness (μm)</i>	<i>Zn-free White Bronze measured thickness (μm)</i>
0,5	0,47	0,48
1	1,13	1,02
1,5	1,70	1,47

Table 2 - thickness of the Zn-free and Zn-bearing bronze films determined by FIB/SEM cross-sections

A comparative analysis of the cross-sections (e.g., Figure 53) was performed for each sample. All the coatings were compact throughout the cross-section, well adherent to the substrate, and no voids or inhomogeneities in the morphology were observed.

Ionic images were collected after the cross-sectioning to acquire information on the microstructure and faceting. Ionic imaging contrast is, in fact, able to quickly highlight crystal shapes by channeling effect without the need for previous metallographic treatments. Figure 54 compares the cross-sections of the Zn-free (a) and Zn-bearing (b) white bronzes; the images show similar columnar growth.

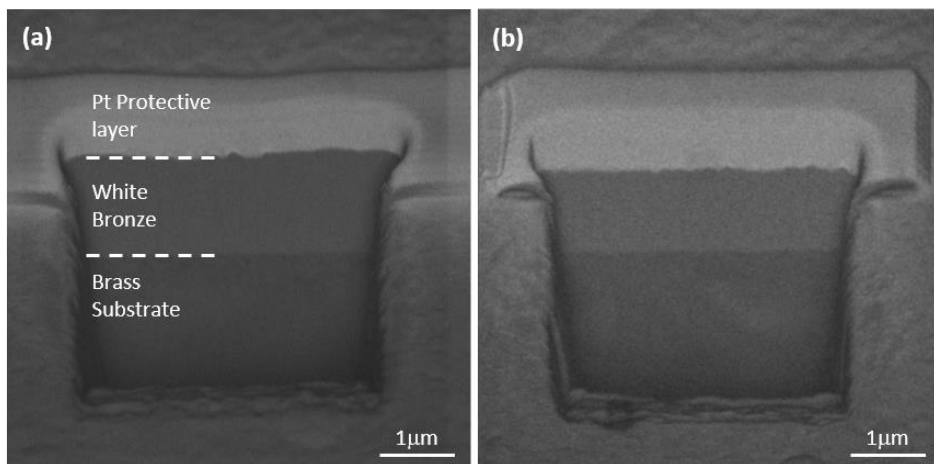
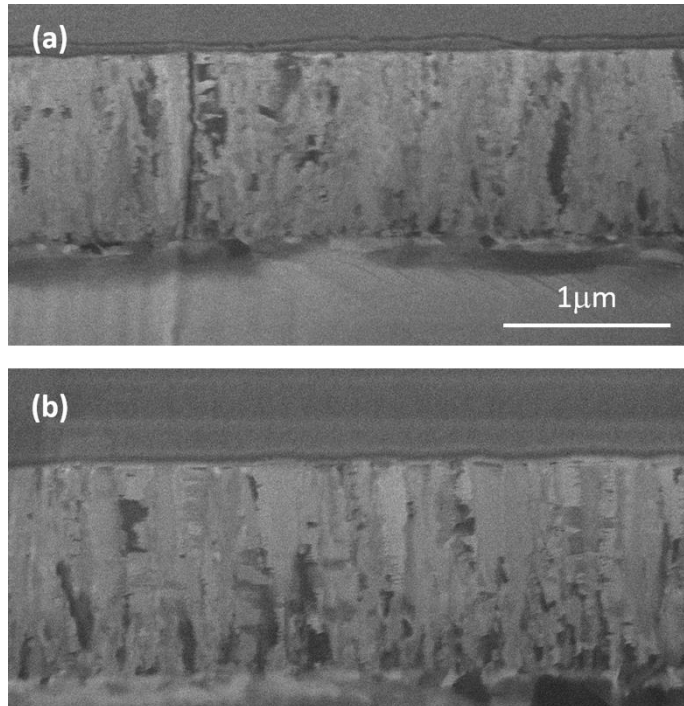


Figure 53 - FIB cross-sections of (a) the 1.5 μm thick Zn-bearing white bronze and (b) the 1.5 μm Zn-free white bronze acquired by the in-beam backscattered electron detector



*Figure 54 – Ionic pictures of two 1.5 μm coatings:
(a) Zn-bearing white bronze and (b) Zn-free white bronze, same scalebar for both images.
The central columnal layer refers to white bronze deposits, while the topmost darker and bottom whiter layers are the Pt protection layer and the substrate.*

3.3.1.3 Bulk composition of the coatings

Brass substrates are commonly used in mass industrial production due to their low cost, easy machining, and corrosion resistance. However, due to the similar composition of the substrate and coating, the determination of the film composition is not straightforward. Furthermore, the presence of copper and zinc in the substrate (brass) and the coating (bronze) hampers liquid phase methods, as no chemical attack can stop at the interface between the coating and the substrate. This also prevents from using X-ray fluorescence. Indeed, minor variations in the substrate composition generate significant errors in estimating the coating composition.

Oppositely, Energy-Dispersive X-ray Microanalysis can measure such composition, even if its application needs special care. However, for small thicknesses like the ones investigated in this study, there is the need to fine-tune the analysis condition to ensure that the interaction volume does not include the substrate. Therefore, we performed Monte Carlo simulations to find conditions that maximize the coatings' signal while ensuring that no X-ray comes from the substrate. Nowadays, these simulations can be readily implemented with software like DTSA II [68], PENEPMA [69], or WinXray [70]. Recently, we have shown that this approach can be applied to the simultaneous estimation of coating thickness and composition in thin films [71]. This approach has been applied here to determine the energy conditions that give the best compromise between the excitation of the Cu and Zn K-lines (energy between 8 and 9 KeV) and the need to avoid the thickness of the interaction volume exceeding the thickness of the investigated layer. Simulations were carried out with CASINO [72].

Calculations showed that at an excitation energy of 12 kV, the interaction volume depth is less than 300 nm. This energy excites Cu and Zn K transitions significantly. s 2 and 3 report the composition of the layer obtained by EDS by applying the ZAF quantification algorithm [73] along with the relative error estimation. The measurements were repeated at ten different points on the surface. Samples with different thicknesses showed a difference in composition for Sn, Cu, and Zn within 1-2 wt% (*Table 3*). No significant composition dependence on the thickness has been observed. In the case of the Zn-Free bronze, the Pd content showed considerable variation. However, the Pd content is in the 1% wt. range, easy to detect but hard to quantify for the low peak-to-background and signal-to-noise ratios. *Table 4* shows that

both the classes of coatings are high tin bronzes, as the tin wt. % resulted in 25-26 wt.% for the Zn bearing and 36 wt. % for the Zn free.

Sample	Element	Weight %			Atomic %			Error %		
		0.5 μm	1.0 μm	1.5 μm	0.5 μm	1.0 μm	1.5 μm	0.5 μm	1.0 μm	1.5 μm
Zn-bearing Bronze	C	4.80	5.10	3.10	22.80	23.55	15.68	10.21	10.19	10.56
	O	1.33	1.60	1.36	4.74	5.56	5.16	8.49	8.34	8.36
	Cu	46.11	47.61	48.23	41.36	41.59	46.04	4.15	4.00	4.06
	Zn	20.87	20.82	21.47	18.19	17.68	19.92	7.33	7.32	7.39
	Sn	26.89	24.87	25.84	12.91	11.63	13.21	3.12	3.09	2.98
Zn-free Bronze	C	1.84	1.29	2.10	10.47	7.40	11.60	43.13	12.28	11.02
	O	0.70	1.26	1.25	3.01	5.47	5.20	9.86	8.38	8.39
	Cu	60.74	59.70	59.85	65.34	65.01	62.55	4.94	5.01	4.96
	Pd	0.61	1.66	1.12	0.39	1.08	0.70	30.00	7.60	9.13
	Sn	36.10	36.09	35.68	20.79	21.04	19.96	3.06	2.76	2.77

Table 3 - Compositional results (all elements) of the EDX analysis on both Zn and Zn-free white bronzes. EDX measurements performed at 12 kV.

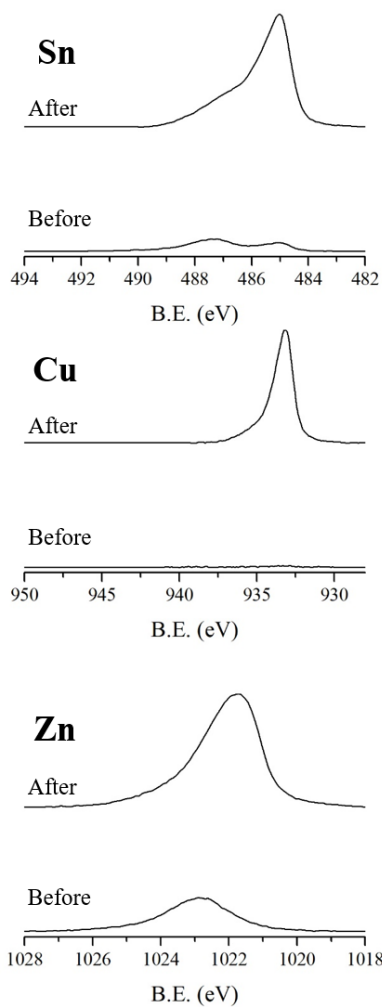
Sample	Element	Weight %			Atomic %			Error %		
		0.5 μm	1.0 μm	1.5 μm	0.5 μm	1.0 μm	1.5 μm	0.5 μm	1.0 μm	1.5 μm
Zn-bearing Bronze	Cu	48.77	50.57	50.16	56.56	58.05	57.73	4.18	4.02	4.06
	Zn	22.95	23.11	23.00	25.88	25.78	25.73	7.49	7.50	7.50
	Sn	28.28	26.32	26.84	17.56	16.17	16.54	3.09	3.02	2.96
Zn-free Bronze	Cu	62.50	61.37	62.14	75.66	74.70	75.36	4.97	5.03	4.98
	Pd	0.61	1.71	0.79	0.44	1.24	0.57	29.88	7.65	26.08
	Sn	36.88	36.92	37.07	23.90	24.06	24.07	3.04	2.78	2.81

Table 4 - Compositional results (metals only) of the EDX analysis on both Zn and Zn-free white bronzes. EDX measurements performed at 12 kV.

3.3.2 Surface composition (XPS)

A comparison of the XPS peaks for all metallic elements, Oxygen, and Carbon, before and after sputtering, is reported in Figure 55 and Figure 56. A complete summary of the surface composition is reported in Table 5.

Zn White Bronze



Zn-free White Bronze

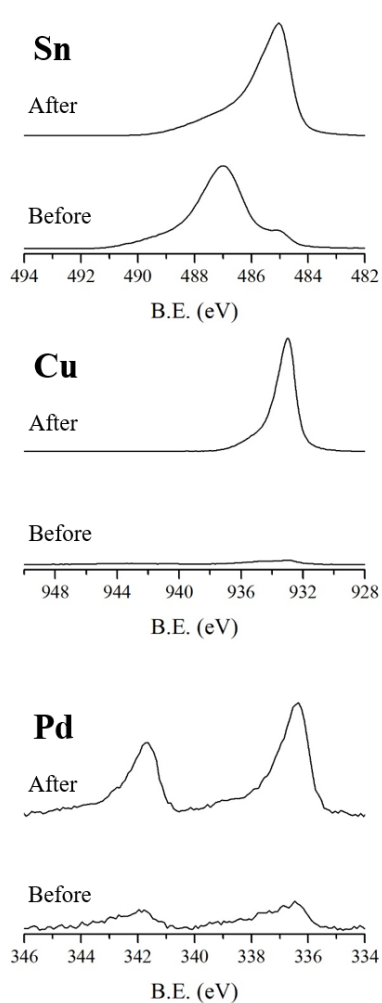


Figure 55 - High-resolution XPS spectra of the 1 μ m Zn white bronze (left) and 1 μ m Zn-free white bronze (right) before and after ion sputtering. Cu 2p, Sn 3d, Zn 2p and Pd 3d regions

Sample	Element	Before Sputtering (% Atomic)			After Sputtering (% Atomic)		
		0.5 μm	1.0 μm	1.5 μm	0.5 μm	1.0 μm	1.5 μm
Zn-bearing Bronze	C	72.67	76.10	75.22	3.48	7.03	3.66
	O	20.76	18.50	19.25	11.50	11.12	12.29
	Cu	ND	ND	ND	36.12	35.80	35.36
	Zn	5.29	3.91	4.26	25.41	25.42	25.31
	Sn	1.27	1.08	1.28	23.49	20.63	23.38
Zn-free Bronze	C	47.75	51.75	52.37	0.96	0.50	1.39
	O	35.40	33.53	33.00	1.37	3.27	4.30
	Cu	4.25	4.93	4.63	74.71	74.23	70.83
	Pd	0.11	0.17	0.08	1.13	1.71	1.32
	Sn	12.49	9.61	9.92	21.83	20.29	22.16

Table 5 - Surface atomic % composition of Zn white bronze and Zn-free white bronze before and after ion sputtering

Sample surfaces showed a composition that differs from the bulk composition found using EDS. First, a significant amount of carbon and oxygen was observed in both Zn-bearing and Zn-free coatings. The as-deposited samples showed a significant concentration of carbon at the surface. However, the shape of the carbon peak demonstrated dissimilar contamination for the two coatings. Zn-containing bronzes were the most contaminated, suggesting that additives used in the bath remained on the surface even after cleaning with water and ultrasounds. For the Zn-bearing white bronzes, an intense signal can be attributed to C-O, in agreement with the results obtained by the morphological studies (Table 5). All samples

showed a component at 286.3 eV that is typical of the polyalcohols employed as brighteners [74] (Figure 56).

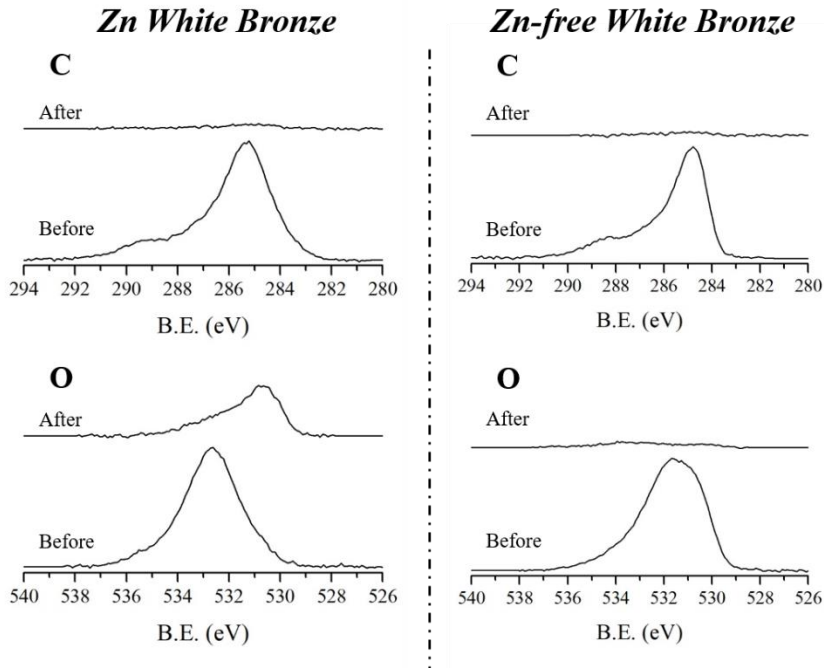


Figure 56 - High-resolution XPS spectra of the 1 μ m Zn white bronze (left) and 1 μ m Zn-free white bronze (right) before and after ion sputtering. C 1s and O 1s regions

The surface of samples before sputtering showed no copper in the case of the Zn-bearing bronze. Similarly, the unsputtered Zn-free bronze showed a copper content significantly lower than what was expected from the analysis of the bulk concentration, with copper atoms in the form of oxide or hydroxide species (Cu^0 and Cu_2O at 932.1 eV, that are not distinguishable using standard XPS analysis, and CuO at 933.4 eV [75]). Additionally, surface tin was almost completely oxidized in the Zn-free bronze (Sn^0 at 485.0 eV, Sn Oxides at 486.5 eV [76]), while a direct comparison with the Zn-bearing

bronze showed that a more substantial fraction of tin at the surface was metallic. In these samples, Zn is in the form of oxides (Zn^0 at 1021.8 eV, Zn Oxide at 1022.1 eV [77]).

All the examined samples showed metal ratios much different from the bulk, with lower copper content on the surface (*Table 6*).

Sample	Element	Before Sputtering (% Atomic)			After Sputtering (% Atomic)		
		0.5 μm	1.0 μm	1.5 μm	0.5 μm	1.0 μm	1.5 μm
Zn-bearing Bronze	Cu	ND	ND	ND	42.5	43.7	42.1
	Zn	80.6	78.4	76.9	29.9	31.1	30.1
	Sn	19.4	21.6	23.1	27.6	25.2	27.8
Zn-Free Bronze	Cu	25.2	33.5	31.7	76.5	77.1	75.1
	Pd	0.7	1.2	0.5	1.2	1.8	1.4
	Sn	74.1	65.3	67.8	22.3	21.1	23.5

Table 6 - XPS atomic ratios between a single metal and the overall metal content in Zn white bronze moreover, Zn-free white bronze before and after ion sputtering

XPS acquired after sputtering showed better agreement with the result of the bulk composition (*Table 3*) for the Zn-free bronze samples. The concentration of zinc and tin for the Zn bronze after sputtering was still noticeable, despite a lower extent to the non-sputtered samples. Pd content does not change significantly after surface sputtering, as its atomic fraction remained aligned with the values acquired during EDS experiments. Moreover, we found that all the elements in bulk were in the metallic state, and the carbon contamination disappeared after sputtering. Only a tiny amount of carbon

(less than 1% at.) remained. Considering that after the sputtering process, the superficial carbon contamination (adventitious carbon) was removed, the remaining atoms of this element can be located only on the bulk of the samples. This indicates that the coatings may retain some carbon impurities due to incorporating the galvanic bath organic additives.

3.3.3 XRD Measurements

To identify the crystalline structure of the coatings, we performed X-ray diffraction experiments; Figure 57 reports the experimental diffractograms along with the simulated patterns. Typically, electrodeposited bronze consists of intermetallic compounds such as Cu_6Sn_5 and Cu_5Zn_8 [78,79]. The diffractograms of the Zn bearing and the zinc-free materials showed a peak at 30° due to the (101) reflection of the Cu_6Sn_5 structure [80,81]. The peak fitting of the diffractogram confirmed this. The occurrence of the Cu_5Zn_8 [80] phase in the Zn bearing material is harder to prove, as its peaks superimpose much with those of Cu_6Sn_5 and the brass substrate (the (110) at $\sim 42.8^\circ$ of the β -brass). XRD spectra simulation was performed to separate the contribution of the layers. The fit of the diffraction pattern matches (Figure 57) the intensities of the peaks much better when the Cu_5Zn_8 phase is added in the simulated spectra (Mean squared error, wR^2 , is reduced from 10% to 6%), suggesting its presence. No Pd-related peak was visible from the Zn-Free bronze XRD data, suggesting that adding a small palladium fraction does not significantly affect the coating structure.

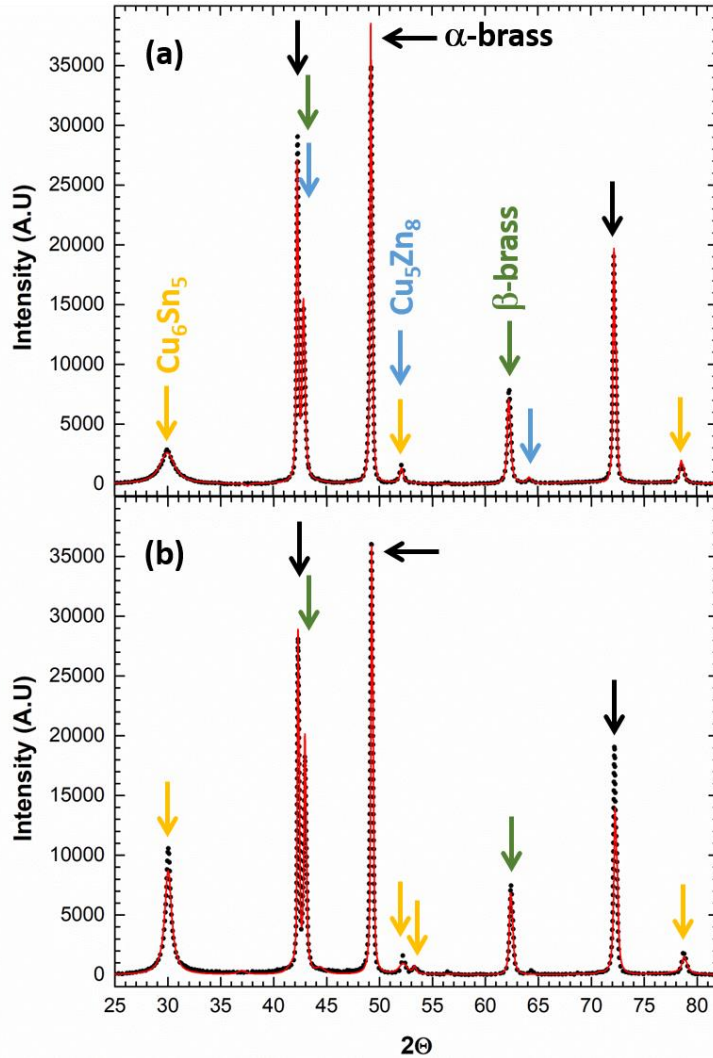


Figure 57 - Simulated (solid red line) and experimental (dotted black line) X-ray diffractograms of the Zn-bearing (a) and the Zn-free (b) bronzes. The α -brass (black), β -brass (green), Cu_6Sn_5 (yellow), and Cu_5Zn_8 (blue) visible peaks are reported

All the recorded diffractograms clearly showed the peaks of the substrate; three peaks were attributed to the α -phase, while three others were to the β -phase. This is consistent with the phase speciation expected for a Cu 67 wt. % and Zn 33 wt. % brass [82].

The whole pattern analysis yields a crystallite size of $70(\pm 5)$ nm for the Zn-bearing bronze and of $50(\pm 5)$ for the Zn-free bronze (isotropic approximation). This finding agrees with SEM observations, which showed a nanometric roughness of the surface with minor features in the case of the Zn-Free bronze.

3.3.4 *Characterization of the color*

Color coordinates were reported in *Table 7* (where unity distances between samples in color space are shown) and in and in *Table 8* (where, for each sample, color coordinates are given). In the tabs also, silver coordinates are reported; silver is used as a target color for the bright whitish deposits used in the industry. In the tabs also, silver coordinates are reported; silver is used as a target color for the bright whitish deposits used in the industry. All samples show a bright white color, with a reddish hue, barely perceivable by the naked eye, and a luminosity close to the reference white. Zn white bronzes show a lower dependency of the Lab coordinates on the thickness of the coatings, having all the color distances in the 0-2 range (not distinguishable by naked-eye observation) but a slightly more reddish color (larger a values, see *Table 8*). Zn-Free bronzes are white, but the thinner deposit (0.5 mm) shows a noticeable difference, with the other two samples having a color difference in the range of 2-4. The former has a slightly reddish color, more similar to the Zn white bronzes, having a color distance from those in the range of 1-2 (not distinguishable by the naked eye).

dE (distance)		Zn white bronze			Zn-free white bronze			Ag
		1.5 μm	1.0 μm	0.5 μm	1.5 μm	1.0 μm	0.5 μm	
Zn white bronze	1.5 μm	0	2	2	4	6	2	18
	1.0 μm	2	0	0	2	4	1	17
	0.5 μm	2	0	0	2	4	0	17
Zn-Free white bronze	1.5 μm	4	2	2	0	2	2	15
	1.0 μm	6	4	4	2	0	4	13
	0.5 μm	2	1	0	2	4	0	17
Ag		18	17	17	15	13	17	0

Table 7 – Unit distances between samples in dE units (colour space).

Label		L	A	b
Zn white bronze	1.5 μm	91	0.7	6.8
	1.0 μm	92	0.5	4.6
	0.5 μm	91	0.7	4.9
Zn-Free white bronze	1.5 μm	93	0.4	3.6
	1.0 μm	95	0.4	3.2
	0.5 μm	91	0.3	5.1
Ag		107	0.1	-1.8

Table 8 – Colour coordinates of the deposited surfaces

3.3.5 Electrochemical corrosion in 3.5% sodium chloride

To determine the corrosion protection that the Zn-Free and Zn-bearing coatings give to brass and to compare the performance of the various coatings, we performed OCP measurements, anodic polarization, and Electrochemical Impedance Spectroscopy (EIS) on the surfaces in sodium chloride solution.

Figure 58 shows the OCP data of the two 1mm thick samples and od brass substrate. The curves demonstrate a nobler behavior of the Zn-free sample compared to the Zn-bearing white bronze. Moreover, the OCP data from the two coatings differs sharply from the value obtained from the brass substrate, which is much more negative.

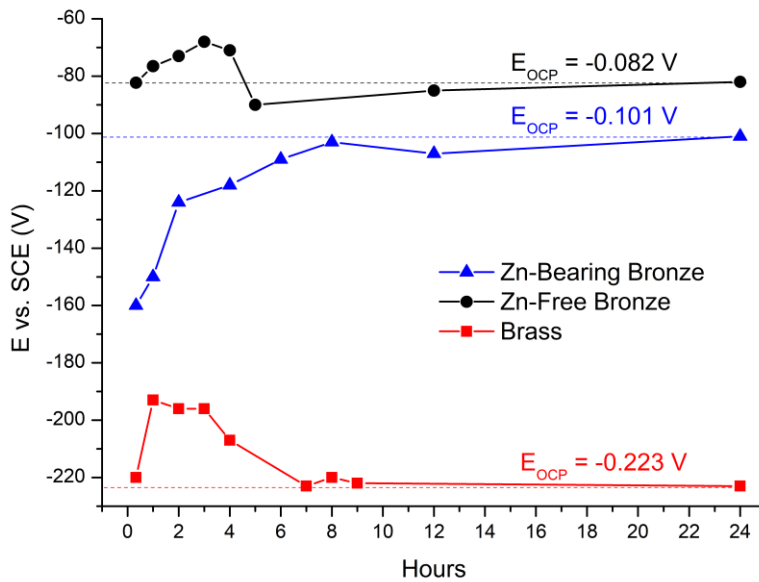


Figure 58 – 24h OCP curves of 1 μ m samples, brass in comparison

Figure 59 reports the polarization curves of the white bronzes of three different thicknesses compared to brass. The corresponding corrosion parameters, OCPs, and corrosion current densities are listed in *Table 9*. From the dataset, it is clear that all the investigated coatings prevent corrosion on the brass; indeed, all the coated samples have more positive OCPs and lower J_{corr} than the substrate (*Table 9*). On such a basis, we conclude that the white bronzes behave as cathodic coatings. However, the OCPs difference between

the two coatings and the uncoated brass is small. We found the most notable difference (147 mV) between brass and the 1.5 μm thick-Zn-Free coating. In contrast, for the Zn-bearing materials, the OCP difference with the substrate is lower than 100 mV for each film thickness, indicating a small galvanic coupling between the coating and the substrate.

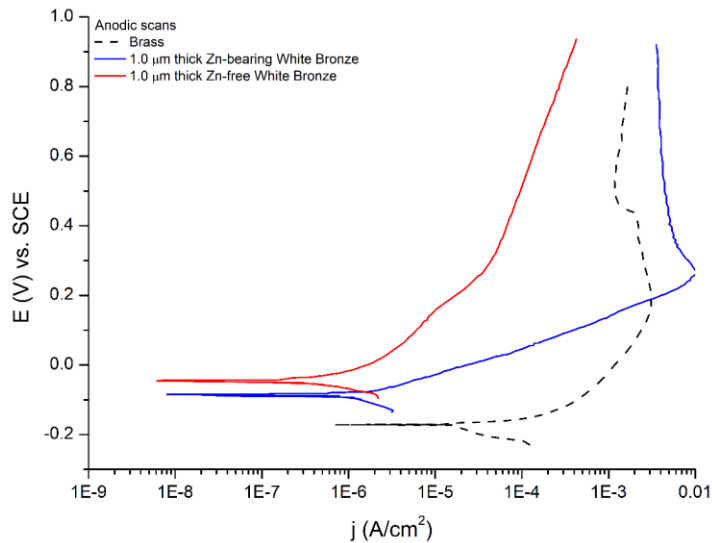


Figure 59 – Comparison between anodic sweeps of different thicknesses of Zn-bearing white bronzes (blue curve), Zn-free white bronzes (red curve) and bare brass (substrate, dotted curve)

We observed that at a fixed anodic potential of 0.23 V, the corrosion current of the Zn-bearing bronzes (ca. 10^{-2} A cm^{-2}) is much larger than the Zn-Free bronze (10^{-5} A cm^{-2}). This trend is maintained in the whole anodic range of the potentiodynamic scan; Zn-Free shows a steeper slope indicating that the kinetics of the corrosion process is slower than for the Zn-bearing materials. Accordingly, the resistance to the anodic stress of the brass protected with the Zn-Free coatings significantly exceeds the resistance of the Zn-bearing ones.

Sample		OCP 1 [V]	J _{corr} 1 [A/cm ²]	OCP 2 [V]	J _{corr} 2 [A/cm ²]
Zn-bearing White Bronze	0.5 μm	-0.126	1.66 x 10 ⁻⁶	-0.166	4.40 x 10 ⁻⁵
	1.0 μm	-0.085	2.79 x 10 ⁻⁷	-0.115	3.19 x 10 ⁻⁵
	1.5 μm	-0.095	4.37 x 10 ⁻⁷	-0.111	2.24 x 10 ⁻⁵
Zn-Free White Bronze	0.5 μm	-0.132	4.77 x 10 ⁻⁷	-0.088	2.23 x 10 ⁻⁶
	1.0 μm	-0.046	1.49 x 10 ⁻⁷	-0.107	2.06 x 10 ⁻⁵
	1.5 μm	-0.023	5.80 x 10 ⁻⁷	-0.107	1.42 x 10 ⁻⁵
Brass		-0.170	1.11 x 10 ⁻⁵	-0.117	3.22 x 10 ⁻⁵

Table 9 – Summary of the electrochemical parameters obtained from potentiodynamic cycles

Additionally, we explored the effect of the thickness on the corrosion performance. To do so, we recorded the samples' polarization curves with a nominal thickness of 0.5, 1, and 1.5 μm (Figure 60). We observed that for both materials, the 0.5 μm samples show more negative OCPs and that these are relatively close to that of brass (Table 9). The 1.0 and 1.5 μm samples show more cathodic OCP values than the 0.5 μm samples. In addition, the 1.0 and 1.5 μm samples show OCP values more cathodic compared to the 0.5 μm

samples. In addition, the 1.0 and 1.5 μm samples show OCP values more cathodic compared to the 0.5 μm samples. Moreover, the maximum corrosion current density was lower in the thinnest films than in the thicker ones (*Table 9*).

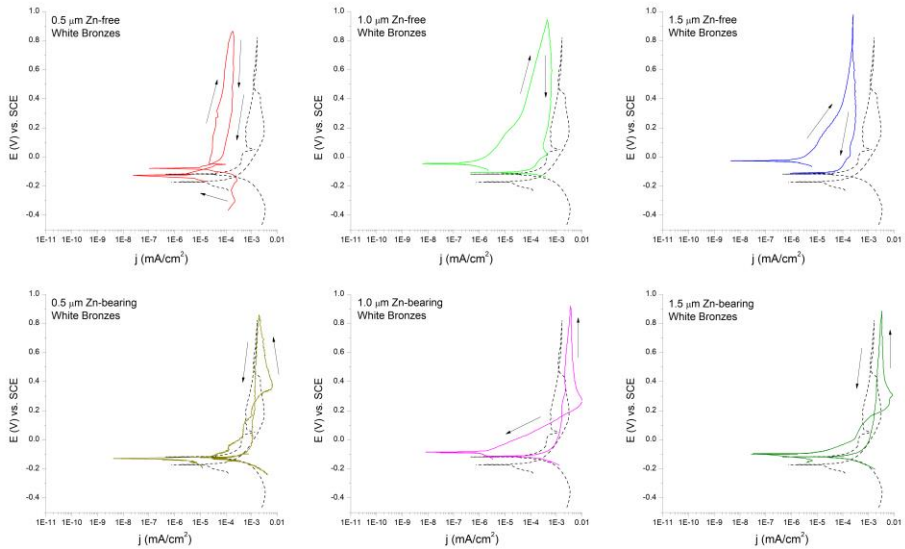


Figure 60 - Comparison between the polarisation curves of Zn-free white bronze (top row), and Zn-bearing white bronze (bottom row) electrodeposited white bronzes in a 0.62M NaCl solution in water at pH 8.2

As the composition does not significantly change with thickness, such behavior may likely result from discontinuities in the thinner coatings, exposing the brass underneath.

Figure 61 reports the result of the visual inspection of the samples after the cyclic polarization experiments. The Zn-Free samples did not show appreciable changes after the corrosion test, retaining the original silvery appearance. In contrast, the Zn-bearing samples experienced a homogeneous corrosion process that changed the color from metallic to brownish copper.



Figure 61 – Zn-bearing (top row) and Zn-free (bottom row) samples after polarisation cycles; the red square indicates an almost-invisible corrosion mark for the 0.5 μm Zn-free sample

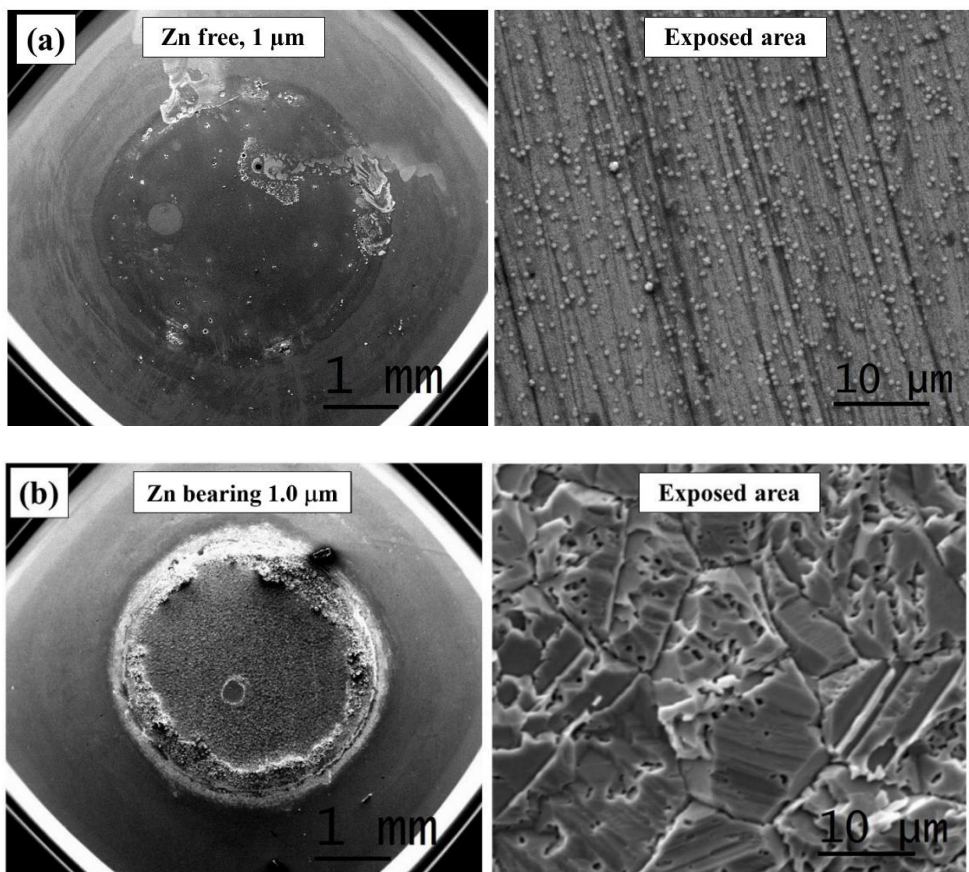


Figure 62 – (a) Zn-free and (b) Zn-bearing white bronze samples after the polarisation cycles.

SEM images (Figure 62) supported the evidence of uniform corrosion in the Zn-bearing bronzes (Figure 62b). From the images, a complete dissolution of the coating can be seen, with the uncovering of the dezincified brass grains of the substrate. Oppositely the surfaces of the Zn-Free bronzes showed evidence of localized corrosion phenomena (Figure 62a), in line with what was reported in the literature for bulk materials of similar composition [83]. This phenomena manifest to a bigger extent on the boundary between sample holder sealing and exposed sample surface and can result from a localized higher current density. However, copper content in an alloy is known to favor pit nucleation when the object is immersed in a NaCl-rich

solution. This process is assisted by the hydrolysis of Sn^{4+} ($\text{Sn}^{4+} + 4\text{H}_2\text{O} \rightarrow \text{Sn}(\text{OH})_4 + 4\text{H}^+$).

In contrast, Cu-Zn-Sn alloys with Zn content of 20% or more initially form a Zn oxide surface layer providing some protective action, followed by dissolution in chloride media [50]. Figure 63 also shows the formation of localized flakes in the Zn-Free sample. EDS suggests an oxygen enrichment on these structures, which is consistent with the formation of Zn oxide in the proximity of the corroded regions, while flakes likely originate from the precipitation of the dissolved zinc from the brass underneath the sample's surface. This demonstrates that the corrosion proceeds locally on small anodic spots of uncovered brass in the Zn-Free bronze. In contrast, the corrosion of the Zn-bearing coatings is uniform, as revealed by the SEM images that, after the polarization experiments, showed the etched grain structure of the brass substrate.

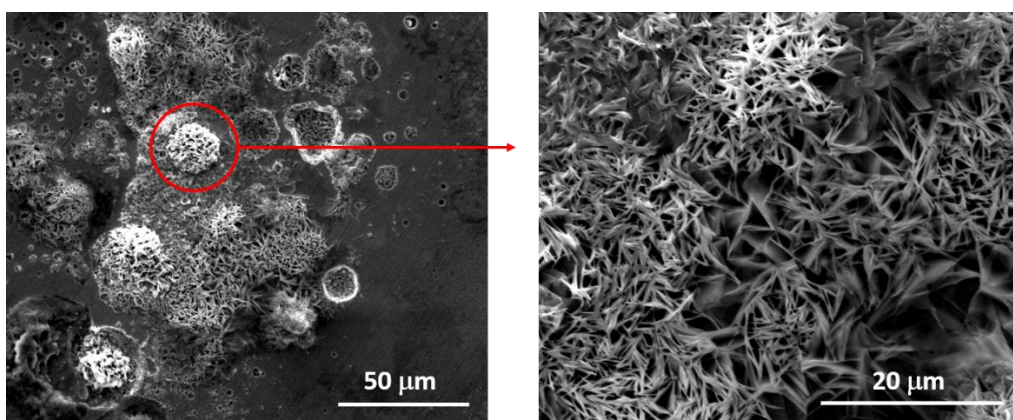


Figure 63 – (left) An image of the surface of a Zn-free bronze sample ($1\mu\text{m}$ thick) after polarisation tests. A zoomed image of the flaky-like Zn structure (right) is also presented.

A perusal of XPS data can achieve further insight into the behavior of the coatings. All the tested samples were left in the atmosphere after their preparation, forming the open-air passivation patina on their surface. We found that in the Zn-Free bronze, the passivation layer at the surface consists mainly of tin dioxide with a small amount of copper oxide, while in the Zn-bronze, it was a mixture of various oxides of Sn and Cu and metallic Sn. The literature shows that tin's passivation power in chloride media is higher than that of Zn [84].

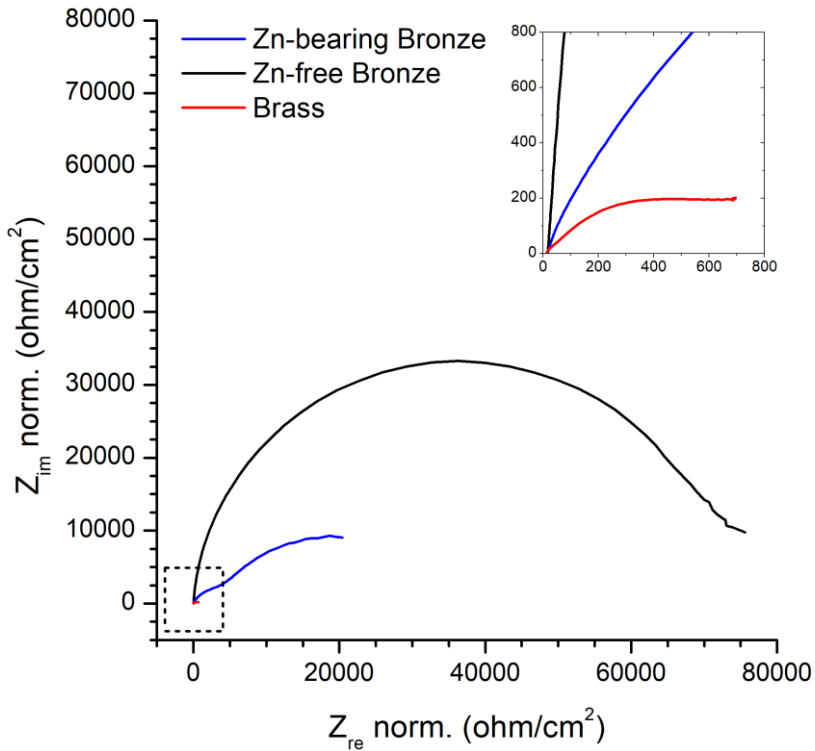


Figure 64 – Nyquist plot of $1\mu\text{m}$ samples and substrate brass

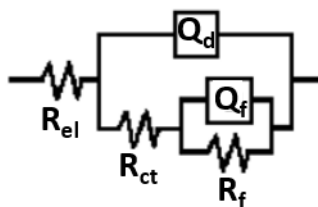


Figure 65 – The circuit used for EIS data fitting. R_{el} , R_{ct} , and R_f are, respectively, the electrolyte resistance, the charge transfer resistance, and the Faradic resistance. Q_d and Q_f are Constant Phase Elements related to double-layer capacitance and faradic capacitance.

Finally, we performed EIS measurements, on two pristine 1mm thick coatings, after an hour of immersion in the NaCl electrolyte. In Figure 64, shows the Nyquist Plot of the two 1 mm thick bronzes. The figure shows that the sample with the highest impedance at low frequencies (less than 10 Hz) is the Zn-free with respect to the Zn-bearing one. EIS data were fitted using a circuit with two CPE elements (Figure 65). The model includes charge transfer and faradic reactions above the surface, and it is widely reported in the literature for investigating copper alloys in NaCl aqueous solutions [85–87]. From the fitting of the data related to the two bronzes, we obtained two different values for R_{ct} ; for the Zn-bearing sample, we obtained an R_{ct} of $3.96 \times 10^3 \Omega$, while the value for the Zn-free one was $6.92 \times 10^4 \Omega$. We found an R_{ct} value for the brass substrate of $2.14 \times 10^1 \Omega$. A minor variation was seen between the two R_f values ($3.58 \times 10^4 \Omega$ and $3.29 \times 10^4 \Omega$, respectively vs. $1.93 \times 10^3 \Omega$ of the brass). The χ^2 between the fitting and the obtained data were below 10^{-3} for all the samples. Both the data obtained by EIS circuit fitting and the Nyquist plot confirmed a faster corrosion rate for the Cu-Zn-Sn bronzes and a more passive electrochemical behavior of the Zn-free sample, confirming the trends already observed in the potentiodynamic scans.

3.4 Conclusion

In this work, we have investigated two electrodeposited white bronzes: Cu, Zn, and Sn (Zn-bearing white bronze) and another consisting of Cu, Sn, and a small amount of Pd as an alloying element (1 % wt., Zn-free white bronze).

A particular focus was placed on determining the corrosion protection the coatings bestow in chloride media. This is a point of high significance since white bronzes applications, e.g., protective layers for electrical connection for automotive or as coatings for fashion or technical clothes, often involve being used in chloride-rich environments.

Electrochemical corrosion tests in 3.5 % NaCl demonstrated two different corrosion mechanisms for the coatings. Zn-free coatings perform better and retain the original appearance even after the potentiodynamic testing in NaCl solution. In contrast, the Zn-bearing ones tend to corrode uniformly, reaching the brass substrate underneath. Based on the results of the XPS analysis, we suggest that the enhanced corrosion resistance provided by the Zn-free coating results from the formation of a continuous and electrochemically inert tin oxide layer at the surface. In addition, SEM imaging of the coating surface after the polarization tests showed localized corrosion phenomena for these deposits. Such localized corrosion is mainly found near the sample holder's circular border and can result from a higher current density during potentiodynamic scans.

Moreover, it could result from an occasional lack of continuity in the film coverage. Oppositely, the Zn-bearing bronzes corrode uniformly with the color of the exposed area that turns from shiny metallic to reddish copper-like. This is due to the preferential dezincification of the surface, and the

precipitation of insoluble Cu oxides and hydroxides, with the formation of a porous patina.

After 24 hours, the OCP value of the Zn-free sample was the least negative, followed by the Zn-bearing coated sample and brass.

The EIS analysis confirmed the trend in corrosion resistance observed by the potentiodynamic scans. In addition, the Nyquist plots displayed that the Zn-free coating has the highest impedance in the spectrum's low-frequency (< 10 Hz) range, indicating a slow charge transfer and the highest faradaic resistance.

Our findings indicate that the Zn-free coated samples are less affected by corrosion in chloride media. Therefore Zn-free should be the coating of choice if exposure to the marine atmosphere may occur. A significant amount of Zn in the layer with the concurrent reduction of tin results in dramatically worsening degradation phenomena.

However, a clear explanation of Palladium's role in improving corrosion resistance performance was not achieved. Structural investigations and surface analysis showed that the limited concentration of Pd in the Zn-free coatings does not significantly affect the material's crystal structure and surface composition. No Pd phase was detected by XRD measurements, suggesting no significant role of this element on the anticorrosive properties of the coating. Moreover, XPS analysis reported a slightly lower surface Pd content with respect to bulk before the sputtering process, proposing a lesser influence of this element in the anticorrosive properties of the film.

Section 4

4 A Comparative Research on Corrosion Behaviour of Electroplated and Magnetron Sputtered Chromium Coatings

4.1 Introduction

After nickel, chromium is the most important metal in the electroplating industry. A pleasing reflective appearance, significant corrosion resistance, hardness, low friction, and durability are typical properties of metallic chromium. As a result, chromium layers are widely used as a finishing treatment to improve the functional and aesthetical quality of everyday articles and some industrial items [88–90]. In decorative and protective/decorative coatings based on nickel or copper/nickel, chromium is the almost universal topcoat [91,92]. Commonly the chromium layer is very thin, ranging from 0.1 to 0.8 μm , but it has the vital function of preventing the nickel from tarnishing. Without it, the nickel would soon acquire a greenish or yellowish stain, which is unsightly while not detracting from its corrosion protection. Although electrochemically active, it is fairly corrosion resistant; thanks to a thin but well-adherent surface oxide layer, it becomes passive in many environments.

Chromium coatings are almost universally obtained from one of several variations of the chromic acid bath, using insoluble anodes, usually lead or lead alloys. However, the standard Cr(VI)-based process also has some issues. From an electroplating point of view, chromium has some undesirable characteristics. Also, the well-established Cr(VI) plating baths have a very poor throwing power (i.e., the ability of an electroplating solution to deposit

metal uniformly on cathodes of irregular shape). Articles to be plated, therefore, must be relatively simple in design; deeply recessed, internal angles, or sharp edges must be avoided. Special anode setups (e.g., conforming anodes) can be helpful in this sense, albeit their implementation is not straightforward and raises manufacturing costs. Moreover, plating efficiency is relatively low; extended plating times are required for all but the very thin deposits used in decorative work. Because of these long times, control of such variables as electroplating current, bath temperature, and composition become more critical [90].

Concerning environmental and human health aspects, while metallic and trivalent chromium is a relatively benign species, hexavalent chromium is a well-known human carcinogen [93], in addition to creating other health concerns such as deviated septa and skin and lung irritation [94]. This is why the ban on processes based on hexavalent chromium in the European Union and the USA is urging worldwide companies to look for less hazardous alternatives [95–97].

There are two different technologically feasible approaches to fulfilling this obligation: (1) substituting the hexavalent chromium with other, less toxic, chromium species such as Cr(III), and (2) depositing chromium directly from a metallic source employing gas-phase techniques, thus avoiding, in such a way, the use of chromium ions at all.

The first one is the most straightforward solution. Indeed, electroplating from Cr(III) aqua complexes such as $[\text{Cr}(\text{H}_2\text{O})_6]^{3+}$ has been used for plating the chromium layer. However, this process requires high temperature and high voltages [98], resulting in slow and highly inefficient due to intense hydrogen evolution leading to the formation of aesthetically and functionally barely

suitable coatings [99–102]. Due to the presence of organic complexing agents in the plating baths, Cr coatings obtained from Cr(III) solutions are characterized by the presence of carbides formed during the electrodeposition process, which are responsible for the formation of microcracks that drastically decrease the anticorrosion properties [103]. From an aesthetical standpoint, coatings derived from Cr(III) baths are less appealing than the Cr(VI) ones. The main caveat is that the color or the deposit does not precisely match that of a “conventional” hexavalent chromium which is still considered a benchmark in decorative chromium plating. While the latter exhibit a blueish appearance, a slightly yellow or dark hue is characteristic of chromium layers plated from most trivalent chromium-based electrolytes [104]. This can be ascribable to the abovementioned carbides [105] as well as some inorganic contaminants such as nickel and iron [92] which also negatively affect their anticorrosion properties [106].

On the other hand, chromium electrodeposition from ionic liquids (ILs) and deep eutectic solvents (DES) has also been reported [107–109]. It was thought that using these non-aqueous media would overcome some of the abovementioned obstacles. However, issues regarding the industrial application of these technologies, which require dedicated plants and careful waste management, remain. For instance, as a direct consequence of the high viscosity of these electrochemical baths, both solution losses and potential severe environmental issues due to higher drag-out must be considered.

Regarding non-electrochemical methods used to deposit chromium coatings, thermal spray HVOF (High-Velocity Oxy-Fuel), 3D laser-melt coating, and

atmospheric plasma spraying could be used for industrial applications, mainly to substitute hard and thick (up to 100 μm) chromium plating, such as for the protection of nuclear fuel elements [110]. However, these cannot be considered viable alternatives for decorative purposes due to the relatively high roughness of the obtained deposits. Vice-versa, techniques based upon physical vapor deposition (PVD) allow for the deposition of a thin layer with smooth surfaces, presenting good mechanical and tribological properties. For this reason, several PVD-based techniques are currently used, with a wide range of already established applications [111], especially for aesthetical purposes as a finishing treatment [112,113]. In PVD processes, the material to be deposited is transformed into atomic particles by a thermal collision process and directed to the substrates, where they condense to form a solid coating [114]. The process is typically carried out in a low-pressure and low-temperature chamber, avoiding the internal stresses typical of electrodeposited [115] and high-temperature sputtered coatings [116].

While many types of sputtering processes are available, magnetron sputtering (MS) is the most common. This technique uses the confinement of the exiting plasma by a strong magnetic field that results in high deposition rates and superior adhesion properties compared to vacuum-evaporated films [117,118]. On the other hand, MS coatings also present some drawbacks, such as the formation of defects due to the columnar growth mechanism, which may cause the formation of micropores and pinholes that would negatively affect the tribological and corrosion resistance of the coatings [117,118].

Indeed, the use of MS for the deposition of Cr-based coatings, such as Cr-alloys and CrN, for industrial and technological applications has already been

reported [119,120]. Nevertheless, comparative studies on the morphological and structural characteristics of layers derived from MS and electrochemical deposition methods are relatively scarce in the literature [107–109]. Moreover, although the pros and cons of the two different deposition methods are well known, specific considerations may apply to the system under investigation, impairing the straightforward generalization of their characteristics, such as color, roughness, type of defects, and corrosion behavior [121,122].

In this context, this work aimed to examine the characteristics and physicochemical properties of industrially feasible pure chromium coatings produced by electrodeposition (ED) and magnetron sputtering (MS). In doing this, thin films of the same nominal thickness (0.8 μm) were deposited onto the same copper substrates. The characteristics of these coatings, such as thickness homogeneity, color, and anticorrosion properties, were evaluated and rationally compared to assess the suitability of MS-Cr coating as an industrially feasible alternative to Cr(VI) electroplating.

4.2 Materials and Methods

4.2.1 *Cr Thin Films Deposition*

Copper disks (Electrolytic Tough Pitch purity grade) 20 mm in diameter and 4 mm thick were cut from a bar and used as substrates after polishing up to the mirror finishing with emery paper and alumina paste suspension (down to 1 μm). Before deposition, they were degreased in isopropyl alcohol using an ultrasonic bath (5 minutes), pickled in acidic solution (H_2SO_4 10%v, 3 minutes), rinsed with bidistilled water, acetone (ACS purity grade), and then

dried under nitrogen flow. The absence of embedded abrasive particles was assessed by optical microscope check.

Electrodeposited chromium layers (ED-Cr) were obtained from a commercial bath (NOVOLIT PROCESS, La Tecnogalvano s.r.l., Novara, Italy) directly in an industrial galvanic line, applying voltages between 3,0 and 3,5 V (DC, potentiostatic condition) until obtaining chrome thicknesses of about 0,8 μm . Nominal thicknesses were calculated from bath specifications and checked, after deposition, by weight gain.

MS process was realized on a lab-scale Korvus HEX deposition system (Korvus Technology. Ltd., Newington, UK) equipped with DC magnetron sputtering sources, using a 50 mm diameter chromium target (99,95% purity grade). Before deposition, the chamber was evacuated to a pressure lower than $6.3 \cdot 10^{-3}$ Pa. No electrical polarization of the substrate-holder was applied during the deposition, but the substrate was maintained at 300°C to achieve a smoother surface and better adhesion. The plasma current was set to 150 mA. During deposition (140 minutes), the flow rate of Argon was 30 standard cubic centimeters per minute (SCCM), and the sample stage was kept rotating to improve the thickness uniformity.

4.2.2 Characterization Methods

The thickness of the coatings was determined through X-ray fluorescence (XRF) measurements by using a Bowman B Series XRF spectrometer (Bowman, Schaumburg, IL, USA) employing a semi-fundamental parameter approach (1-point empirical correction) and an acquisition time of 60 s, 50 kV tube voltage, 0.8 mA tube current, and a collimator of 0.6 mm in diameter.

Quantitative color comparisons were obtained using a 380–780 nm wavelength range portable spectrophotometer CM-700d (Konica Minolta, Tokyo, Japan) equipped with an integrating sphere controlled by SpectraMagicNX software (Konica Minolta, Tokyo, Japan). Color coordinates (L^* , a^* , b^*) were obtained from diffuse reflectance spectra according to the CIE's recommendations [36] using a D65 illuminant, an observer at 2° , and a maximum aperture with an angle of incidence $\theta = 8^\circ$. The specular component was included (SCI). The sampled area was 95 mm^2 , corresponding to circular masks having a diameter of 11 mm (MAV11). Each result was averaged using five independent measurements on different sample spots.

Morphological investigations were carried out using a Nikon eclipse LV150 optical microscope (Nikon Metrology Europe NV, Leuven, Belgium) and an electron microscope (Hitachi SU3800 SEM, Hitachi High-Tech, Tokyo, Japan). Near-surface chemical composition was checked through X-ray Photoelectron Spectroscopy (XPS). The experiments were carried out in a vacuum system equipped with a VSW HAC 500 hemispherical electron-energy analyzer using a non-monochromatic Mg $K\alpha$ X-ray source operating at 120 W power ($12 \text{ kV} \times 10 \text{ mA}$). The peaks were fitted using CasaXPS software employing Gauss–Lorentz curves after subtracting a Shirley-type background. X-ray diffraction (XRD) was employed to check the mineralogical nature of the deposits. The spectra were collected at CRIST Centre, University of Florence (Florence, Italy) using an XRD D8 Advance (Bruker Corporation, Billerica, MA, USA) powder diffractometer employing Cu $K\alpha$ (0.154187 nm) radiation in the 2θ range 30° – 100° , applying a step size of 0.03° .

Electrochemical characterization was performed using an Autolab PGSTAT204 potentiostat (Metrohm AG, Herisau, Switzerland) equipped with a FRA32M Frequency Response Analyzer to conduct electrochemical spectroscopy measurements (EIS), controlled by NOVA software and a K0235 flat cell kit (Ametek, Berwyn, PA, USA). A classical three-electrode set-up was employed using a platinum mesh as counter electrodes and an SCE reference electrode separated from the solution by an ion-conducting glass frit. All the experiments were conducted at room temperature ($25 \pm 1^\circ\text{C}$) in a 0.62 M NaCl (3.5 wt.%) aqueous solution, and the exposed working electrode surface was 1.0 cm². Open circuit potentials (OCPs) were obtained by monitoring the potential as a function of time up to one hour. After this period, EIS measurements were carried out at the open circuit potential (E_{ocp}), in a 100 kHz to 10 MHz frequency range, with 10 mV of voltage perturbation amplitude. Then, potentiodynamic curves were acquired in a -0.1 to 1.0 Volt range with respect to the E_{ocp} at the scan rate of 0.167 mV/s. Triplicate measurements checked the reproducibility of the presented data, and typical results were reported.

Finally, free corrosion tests were performed on five samples for every type of coating in a DCT600 P salt spray cabinet (ACS Angelantoni, Massa Martana, Italy), spraying a 50 ± 5 g/dm³ NaCl solution at $35 \pm 2^\circ\text{C}$ (UNI ISO 9227—Corrosion tests in artificial atmospheres. Salt spray tests) for up to 144 h. The corrosion features were then evaluated via visual and optical microscope investigations.

4.3 Results

4.3.1 *XRF Thickness Measurement*

The homogeneity of a coating's thickness was determined via XRF investigation on a grid constituting 13 points of measurement (Figure 66) As expected, the ED samples presented typical tiny edge effects (Figure 66), while these features were almost absent in the MS deposits. On the other hand, these measurements also show that the central portion of the two series of samples on which the electrochemical experiments were performed are very close in terms of thickness, thus allowing for the direct comparison of these results.

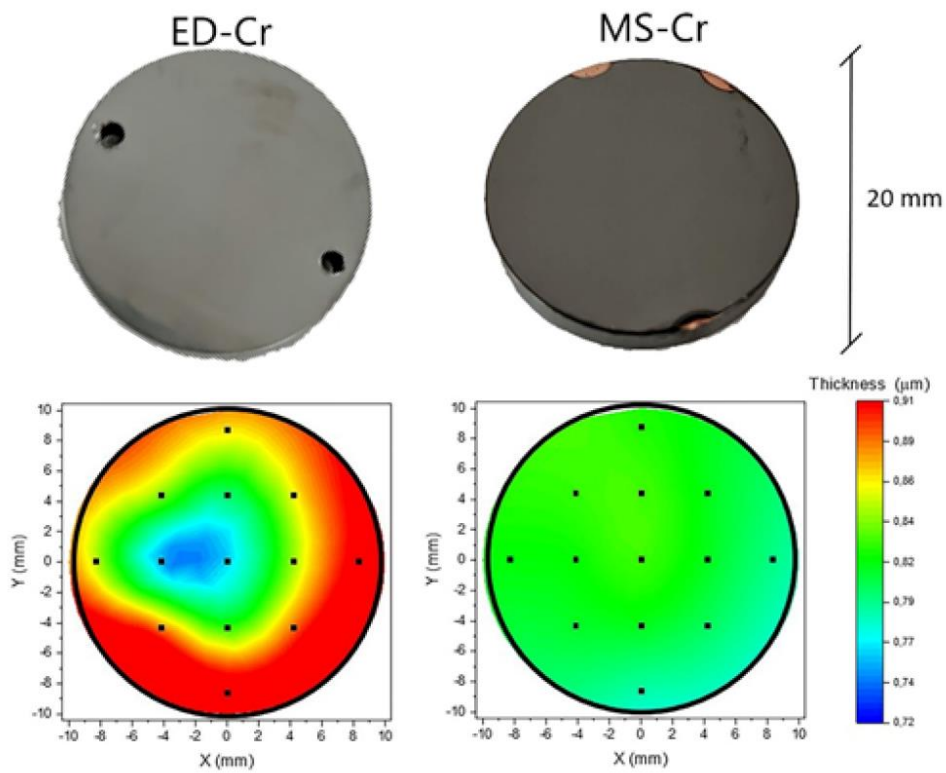


Figure 66 Optical images (above) and respective thickness contour plots (below) of electrodeposited and magnetron-sputtered samples. The black dots in the contour plots depict the grid of points checked by XRF.

4.3.2 Color Measurement

The images displayed in Figure 66 are representative of the different chromium coatings. It is evident that there are some aesthetic differences between them. Both the coatings appeared smooth with a lustrous metallic aspect; however, the MS-Cr samples were darker than the ED ones. Regarding this characteristic, accurate color measurements were performed and expressed in terms of L^* , a^* , and b^* parameters (L^* =light vs. dark, a^* = red vs. green, and b^* = yellow vs. blue). In the CIELAB color space (see Figure 67), the a and b coordinates define the hue (color) and the chroma

(vividness/dullness), while the L^* values represent the degree of lightness. Table 10 summarizes the results of this investigation, evidencing that the MS-Cr coatings were darker and more yellowish than the ED ones. Color differences between differently deposited chromium coatings have already been observed. In many cases, these differences have been attributed to metallic impurities [100] or to the presence of amorphous Cr-phase, graphite, and Cr_{23}C_6 nanoparticles [123] deriving from organic bath additives. In this case, however, different reasons need to be addressed, since XRD, XPS, and EDS measurements (see the following paragraphs) ruled out the presence of carbides and surface or bulk contaminants.

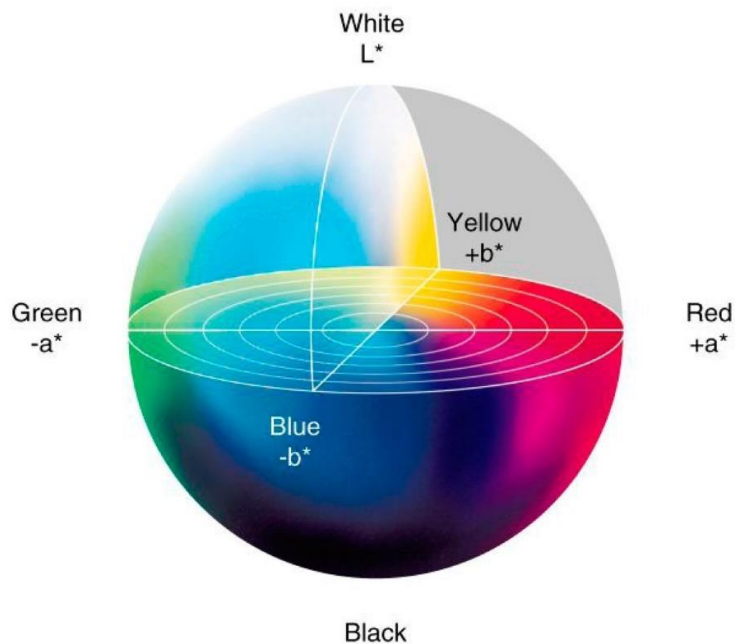


Figure 67 CIELAB color space.

Samples	L*(D65)	a*(D65)	b*(D65)
ED-Cr	81,74	-1,01	-0,96
MS-Cr	48,95	0,90	8,34

Table 10 Colour parameters characteristic of ED and MS chromium coatings.

4.3.3 Morphological and Near Surface Chemical Investigation

An insight into the surface morphology of the samples was achieved by using SEM, which revealed significant differences between the ED and MS coatings, as evidenced by the images in Figure 68. Specifically, even if they were chemically identical (checked by EDS, not shown here), the ED-Cr coatings featured globular structures with grains in the 400–600 nm range. In addition, the coatings also presented some defects, such as holes and macro cracks. On the other hand, the MS-Cr samples did not show evidence of macro defects, and the surface of the coatings exhibited a finer structure not larger than 100 nm, typical of columnar-sputtered Cr coatings [123].

Chemically speaking, the surface of these samples was constituted by nearly pure chromium oxides. XPS spectra collected on the MS-Cr sample (Figure 68c) show the absence of all extraneous elements but carbon, a well-known ubiquitous atmospheric contamination. Therefore, it is reasonable to attribute the darker appearance of these samples to the finer surface nanostructure of the MS-Cr coatings [15]. This conclusion is supported by several literature works on which the visual aspect of MS-Cr coatings changed as a function of different microstructure obtained by tuning the operating parameters such as plasma power and pressure [110] or by polarizing the sample [124].

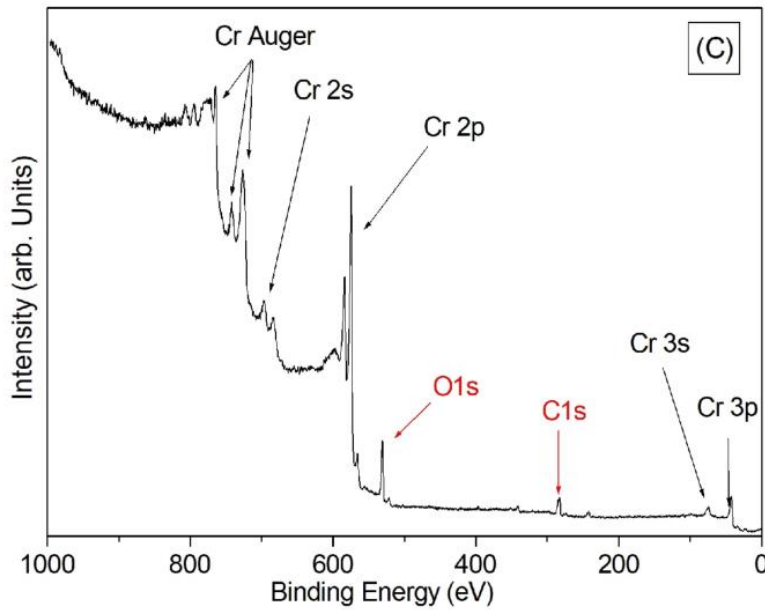
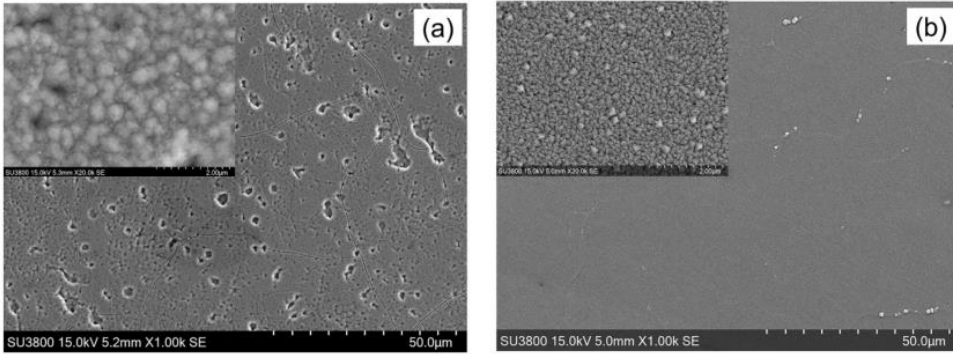


Figure 68 SEM images of the surface topography of ED-Cr, (a) and MS-Cr (b) coating surfaces. XPS survey spectra of MS-Cr coatings evidencing the presence of peaks only attributable to metallic chromium and atmospheric contaminants (carbon and oxygen) (c).

4.3.4 X-Ray Investigation

Figure 69 illustrates the XRD patterns of the ED-Cr and MS-Cr samples collected in Bragg–Brentano mode. The peaks at 44° , clearly detectable for both samples, are attributed to the (110) plane of crystalline chromium. Other characteristic diffraction peaks of crystalline chromium planes (200) and (211) are barely detectable only for the MS-Cr samples, indicating the strong texturizing of both types of deposits. Substrate (copper) diffraction peaks are also indicated. However, there are no peaks attributable to carbides which sometimes result from the reaction of organic additives in the electroplating bath and have been proposed as the reason for yellowish color shifts in the appearance of electrodeposited Cr coatings in the case of chromium (III)-based solutions.

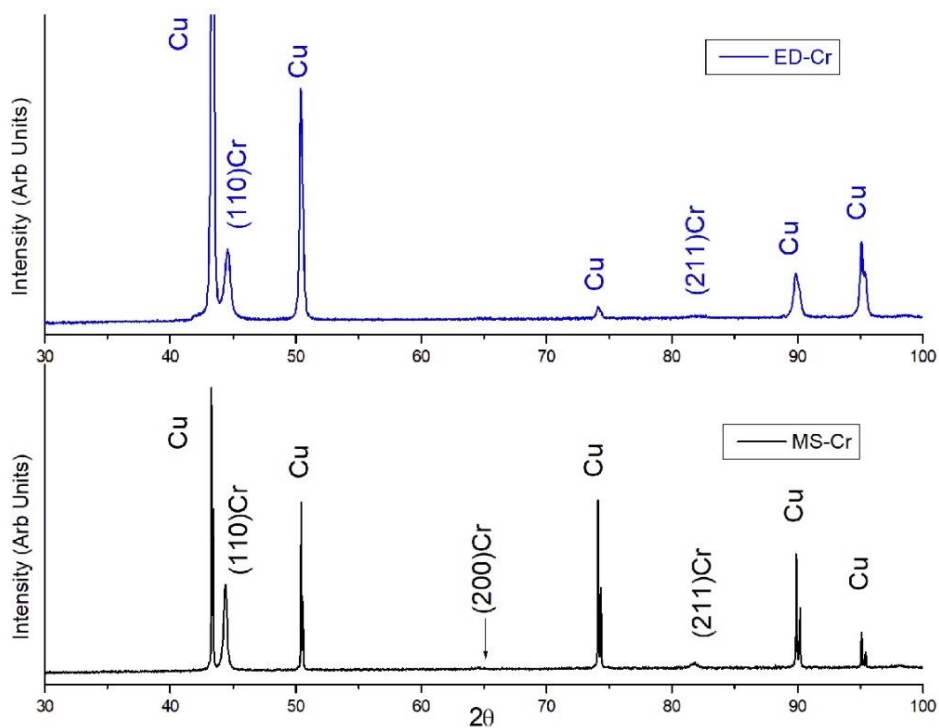


Figure 69 X-ray diffraction of the electrodeposited (ED-Cr, above) and magnetron sputtered (MS-Cr, below) chromium coatings. Substrate (copper) diffraction peaks (copper) have also been indicated.

4.3.5 Electrochemical Characterization

4.3.5.1 OCP

Open circuit potential (OCP) curves were recorded to gain insight into the relative activity of the two chromium coatings. Figure 70 depicts the potential values as a function of time in aerated 3.5% NaCl solution for the two samples compared with the bare substrate (copper). The curves demonstrate the superior behavior of the MS samples with respect to the ED ones, which behaved similarly to the substrate (-0.29 V/SCE for ED-Cr and -0.27 V/SCE copper). That is due to the presence of small cracks and pinholes (Figure 68a) in the ED samples, which allow the test solution to make contact with the

substrate, promoting an active behavior. Vice versa, the absence of these macro defects allowed the MS-Cr coatings to exert a superior level of corrosion protection, reaching a less negative plateau potential (-0.01 V/SCE).

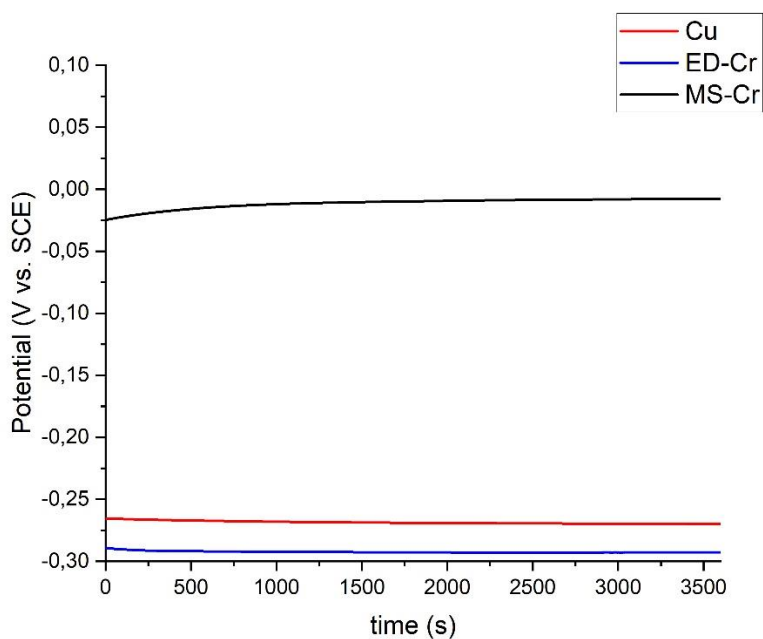


Figure 70 Open circuit potential curves (OCPs) of ED-Cr and MS-Cr coatings compared with the bare Cu in aerated 3.5% NaCl solution as a function of time.

4.3.5.2 Potentiodynamic Polarization

Potentiodynamic polarization (PD) curves were recorded to shed some light on the kinetics of the corrosion processes taking place at the surface. The corresponding curves are displayed in Figure 71 and are compared to pure copper. The ED-Cr samples closely resemble the behavior of copper, the corrosion mechanism of which, in aerated chloride-bearing solutions, is a well-known process [39,40]. Specifically, the process starts with the dissolution of metal through the oxidation of Cu (0) to Cu (I). Next, a labile insoluble CuCl layer absorbs at the surface, providing modest corrosion protection, and finally, Cu (I) oxidizes to Cu (II). On the ground of the similarities in the shapes of the curves collected for Cr-ED samples, it is reasonable that the above-mentioned mechanism also dominates the redox processes taking place at the surface of Cr-ED samples; this is consistent with the presence of macro cracks, as evidenced in Figure 68, which allow the testing solution to make contact with the substrate. However, it is also worth noting that for the ED-Cr samples, the i_{corr} is lower than the pure copper (Figure 71 and Table 11 Electrochemical corrosion data. Table 11), indicating that the corrosion phenomena are the same overall, despite the extent of the result being reduced for the Cr-coated samples. This is attributable to the role played by the Cr-coating in terms of corrosion protection.

The curves collected on the MS coating are characterized by a more positive E_{corr} (Table 11), indicating the superior behavior of this system. On the other hand, the corrosion current, though lower than the pure copper, is higher than in the Cr-ED samples (Table 11). This is probably due to the much finer surface structure of these coatings, which translates onto a larger real surface and, therefore, a higher apparent current density.

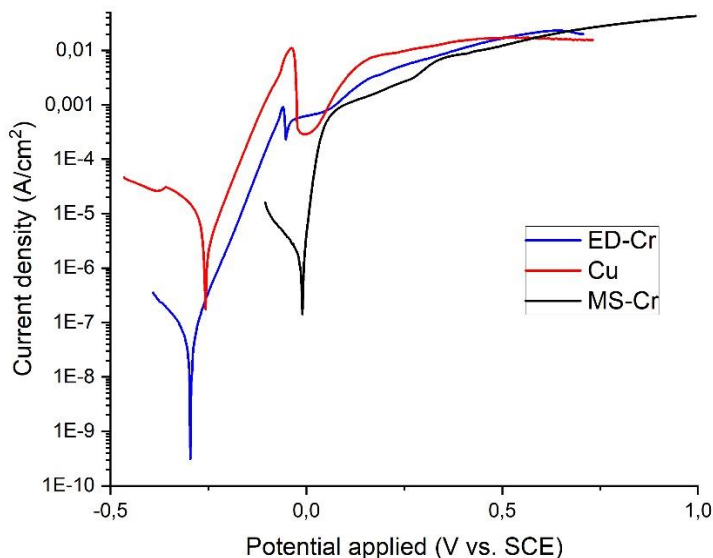


Figure 71 Potentiodynamic curves of ED-Cr and MS-Cr chromium coatings compared with the bare copper substrate in aerated 3.5% NaCl solution.

4.3.5.3 Electrochemical Impedance Spectroscopy (EIS)

Further insight into the interactions between the surface and the solution was gained through investigations through EIS. The AC impedance responses of the prepared samples are depicted as Nyquist and Bode view plots in Figure 71 and compared to those of the bare copper substrates. As shown, the Cr-coated samples are characterized by single capacitive loops with different diameters, while the bare copper substrate presents a more complex AC response which requires two constant phase elements [125]. The equivalent circuits used to fit EIS data are depicted in Figure 73. In these circuits, R_s is the solution resistance, R_{ct} is the charge transfer resistance, and CPE_{dl} is the constant phase element, generally attributed to the double layers

formed at the electrode/electrolyte interface. Table 11 summarizes the data fitting of the experimental curves depicted in Figures 71 and 73.

As shown, the higher values of charge transfer resistance (R_{ct}) are related to the Cr-coated samples, which exhibited less corrosion current densities in the potentiodynamic polarization curve (Figure 71), resulting in a good consistency between these measurements.

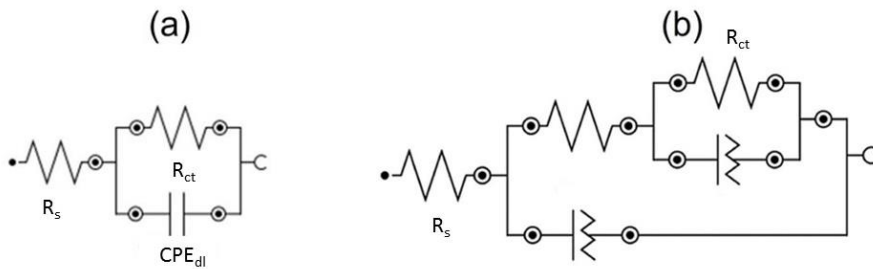


Figure 72 Schemes of the equivalent circuits used for modeling the EIS data in Figure 70. Scheme (a) was used for Cr-coated and (b) for the copper substrate.

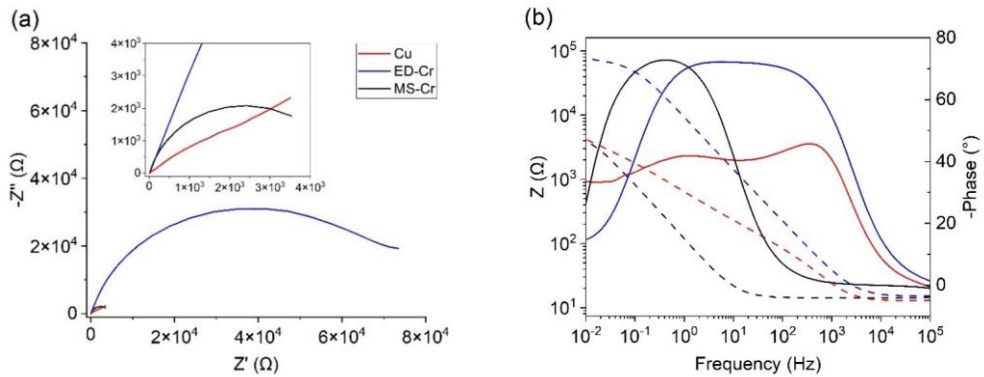


Figure 73 EIS data represented as Nyquist plot (a) and Bode phase plots (b) obtained in aerated 3.5% NaCl solution at room temperature. Samples as in the legend. Inset in the Figure 73a depicts a zoomed view of Nyquist plot.

Samples	OCP	i_{corr} (A/cm ²)	ba (V/dec)	bc (V/dec)	Polarization Resistance R_{ct} (k Ω)
Cu	-0.26±0.01	2,6 E-06	0,06	0,07	13,5
ED-Cr	-0,29±0.01	1,6 E-07	0,06	0,15	130,7
MS-Cr	-0,02±0.01	9,6 E-07	0,02	0,06	4,8

Table 11 Electrochemical corrosion data.

4.3.5.4 Salt Spray Test (Free Corrosion)

Five samples for each type of coating were prepared, as described in the experimental section, and placed in the salt spray chamber for the free corrosion test (neutral salt spray or NSS test, as described in UNI ISO 9227) for up to 144 h. During this time, the corrosion behavior of the different coatings was monitored by visual investigation. A series of photographs representing the same samples at different exposure times are depicted in Table 12. The photographs attest that, in this environment, the MS-coated samples present superior corrosion resistance compared to the ED-Cr ones. This is proved by the reduced color variation due to the smaller amounts of corrosion products developed on the surface. The optical microscope investigation also confirmed this macroscopic result. The micrographs in Figure 74 show the samples' surfaces after 144 h of exposure to the NSS test. These images highlight the formation of larger amounts of dark and dull corrosion products (mainly constituted by copper oxides) on the surface of the ED-Cr compared to the MS-Cr ones.











time (h)	0	24	48	72	144
ED-Cr					
MS-Cr					

Table 12 Images of the samples exposed to the saline environment as a function of time. An ED-Cr sample (above) and an MS-Cr one (below).

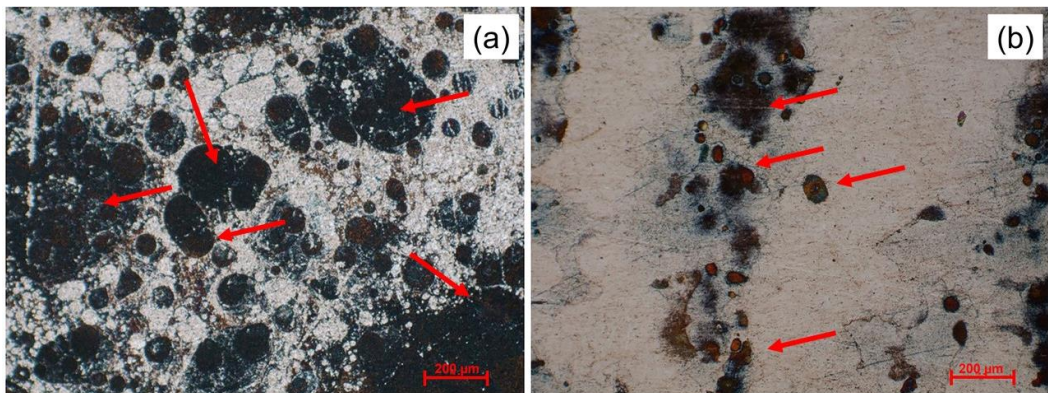


Figure 74 Optical micrographs of the ED-Cr (a) and MS-Cr (b) coatings after free corrosion test (NSS 144 hours). The red arrows indicate the locations of corrosion products. Scale bar 200 μm.

4.4 Conclusion

Pure chromium layers 800 nm thick were deposited, via the magnetron sputtering (MS) technique, onto copper substrates and compared with analogous ones obtained via traditional electrodeposition (ED) from a commercial Cr (VI) plating bath. Although the MS-Cr coatings were

characterized by a darker color, they presented a more homogeneous thickness distribution and similar, if not better, resistance to corrosion in a 3.5% NaCl solution, as proved by both electrochemical and free corrosion tests. Indeed, the MS-Cr coatings displayed superior corrosion potential and developed smaller amounts of corrosion products during free corrosion tests. By means of this comparative investigation in mild condition Cl-bearing aqueous environments, we can support the suitability of the chromium magnetron sputtering technique for use as a viable industrial alternative to the traditional technique of hexavalent chromium electroplating for both aesthetic and corrosion protection purposes.

References

1. Lampke, Th.; Steger, H.; Zacher, M.; Steinhäuser, S.; Wielage, B. Status Quo Und Trends Der Galvanotechnik. *Materwiss Werksttech* **2008**, *39*, 52–57, doi:10.1002/mawe.200700241.
2. Penney, D.J.; Sullivan, J.H.; Worsley, D.A. Investigation into the Effects of Metallic Coating Thickness on the Corrosion Properties of Zn-Al Alloy Galvanising Coatings. *Corros Sci* **2007**, *49*, 1321–1339, doi:10.1016/j.corsci.2006.07.006.
3. Giurlani, W.; Zangari, G.; Gambinossi, F.; Passaponti, M.; Salvietti, E.; Di Benedetto, F.; Caporali, S.; Innocenti, M.; Giurlani, W.; Zangari, G.; et al. Electroplating for Decorative Applications: Recent Trends in Research and Development. *Coatings* **2018**, *8*, 260, doi:10.3390/coatings8080260.
4. The Current Distribution in Electrochemical Cells. In *Fundamental Aspects of Electrometallurgy*; Kluwer Academic Publishers, 2005; pp. 101–143.
5. Park, C.W.; Park, K.Y. An Effect of Dummy Cathode on Thickness Uniformity in Electroforming Process. *Results Phys* **2014**, *4*, 107–112, doi:10.1016/j.rinp.2014.07.004.
6. Belov, I.; Zanella, C.; Edström, C.; Leisner, P. Finite Element Modeling of Silver Electrodeposition for Evaluation of Thickness Distribution on Complex Geometries. *Mater Des* **2016**, *90*, 693–703, doi:10.1016/j.matdes.2015.11.005.

7. Giurlani, W.; Berretti, E.; Innocenti, M.; Lavacchi, A. Measuring the Thickness of Metal Coatings: A Review of the Methods. *Coatings* **2020**, *10*, 1211, doi:10.3390/coatings10121211.
8. ISO 1463:2003 Metallic and Oxide Coatings — Measurement of Coating Thickness — Microscopical Method.
9. ISO 9220:1988 Testing the Accuracy of the Calculation of Gold Leaf Thickness by Mc Simulations and MA-XRF Scanning.
10. Van Kouwen, L. Introduction to Focused Ion Beams, Ion Sources, and the Nano-Aperture Ion Source. In *Advances in Imaging and Electron Physics*; Academic Press Inc., 2019; Vol. 212, pp. 181–216.
11. Schaepe, K.; Jungnickel, H.; Heinrich, T.; Tentschert, J.; Luch, A.; Unger, W.E.S. Secondary Ion Mass Spectrometry. In *Characterization of Nanoparticles: Measurement Processes for Nanoparticles*; Elsevier, 2019; pp. 481–509 ISBN 9780128141830.
12. Sitko, R. Quantitative X-Ray Fluorescence Analysis of Samples of Less than “Infinite Thickness”: Difficulties and Possibilities. *Spectrochim Acta Part B At Spectrosc* **2009**, *64*, 1161–1172, doi:10.1016/j.sab.2009.09.005.
13. Giurlani, W.; Berretti, E.; Lavacchi, A.; Innocenti, M. Thickness Determination of Metal Multilayers by ED-XRF Multivariate Analysis Using Monte Carlo Simulated Standards. *Anal Chim Acta* **2020**, *1130*, 72–79, doi:10.1016/j.aca.2020.07.047.
14. Giurlani, W.; Berretti, E.; Innocenti, M.; Lavacchi, A. Coating Thickness Determination Using X-Ray Fluorescence Spectroscopy: Monte Carlo

- Simulations as an Alternative to the Use of Standards. *Coatings* **2019**, *9*, 79, doi:10.3390/coatings9020079.
15. Barcellos Lins, S.A.; Gigante, G.E.; Cesareo, R.; Ridolfi, S.; Brunetti, A. Testing the Accuracy of the Calculation of Gold Leaf Thickness by MC Simulations and MA-XRF Scanning. *Applied Sciences* **2020**, *10*, 3582, doi:10.3390/app10103582.
 16. Brocchieri, J.; Sabbarese, C. Thickness Determination of the Gilding on Brass Materials by XRF Technique. *Nucl Instrum Methods Phys Res B* **2021**, *496*, 29–36, doi:10.1016/j.nimb.2021.03.018.
 17. Sabbarese, C.; Brocchieri, J.; Scialla, E. Gold-coating Thickness Determination on Ag, Cu, Fe, and Pb Using a Handheld X-ray Instrument. *X-Ray Spectrometry* **2021**, xrs.3221, doi:10.1002/xrs.3221.
 18. Porcinai, S.; Heginbotham, A. Thickness Mapping of Organic Layers Applied on Sterling Silver by Means of X-Ray Fluorescence Scanning. *Spectrochim Acta Part B At Spectrosc* **2021**, *180*, 106158, doi:10.1016/j.sab.2021.106158.
 19. Nygård, K.; Hämäläinen, K.; Manninen, S.; Jalas, P.; Ruottinen, J.-P. Quantitative Thickness Determination Using X-Ray Fluorescence: Application to Multiple Layers. *X-Ray Spectrometry* **2004**, *33*, 354–359, doi:10.1002/xrs.729.
 20. Vrieling, J.A.M.; Tiggelaar, R.M.; Gardeniers, J.G.E.; Lefferts, L. Applicability of X-Ray Fluorescence Spectroscopy as Method to Determine Thickness and Composition of Stacks of Metal Thin Films: A Comparison with Imaging and Profilometry. *Thin Solid Films* **2012**, *520*, 1740–1744, doi:10.1016/j.tsf.2011.08.049.

21. Staudt, G.E. Estimation of Uncertainty in Plate Thickness Measurement By X-Ray Fluorescence Spectrometry - Tyco Electronics. *AMP Journal of Technology* **1993**, 3, 85–97.
22. Sokolov; Hasikova; Pecerskis; Gostilo Industrial X-Ray Fluorescence Analyzer for Real-Time Thickness Measurements of Aluminium Coatings on Rolled Steel. *Coatings* **2019**, 9, 425, doi:10.3390/coatings9070425.
23. ASTM B568 - 98(2014) Standard Test Method for Measurement of Coating Thickness by X-Ray Spectrometry 2014.
24. *Surface Engineering for Corrosion and Wear Resistance*; Davis, J.R., Ed.; 1st ed.; ASM International, 2001; ISBN 9780871707000.
25. Taylor, S.R. Coatings for Corrosion Protection: Metallic. In *Encyclopedia of Materials: Science and Technology*; Elsevier, 2001; pp. 1–5.
26. IDC2D.
27. ISO 3497:2000 Metallic Coatings — Measurement of Coating Thickness — X-Ray Spectrometric Methods 2000.
28. Dickinson, E.J.F.; Ekström, H.; Fontes, E. COMSOL Multiphysics®: Finite Element Software for Electrochemical Analysis. A Mini-Review. *Electrochem commun* **2014**, 40, 71–74, doi:10.1016/J.ELECOM.2013.12.020.
29. Dos Santos, W.A.T.; Dos Santos, W.I.A.; De Assis, S.L.; Terada, M.; Costa, I. Bronze as Alternative for Replacement of Nickel in

- Intermediate Layers underneath Gold Coatings. *Electrochim Acta* **2013**, *114*, 799–804, doi:10.1016/j.electacta.2013.10.040.
30. Moretti, G.; Guidi, F.; Capobianco, G.; Tonini, R. Ni-Free Alloys as Final Coatings: White Bronze Coatings on Copper. *J Mater Chem* **2001**, *11*, 922–925, doi:10.1039/b006401g.
 31. Caporali, S.; Bardi, U. Corrosion Mechanism in Artificial Sweat Solution of In-Bearing White Bronze Alloy. *Corrosion* **2012**, *68*, doi:10.5006/1.3683223.
 32. Hovestad, A.; Tacken, R.A.; 'T Mannelje, H.H. Electrodeposited Nanocrystalline Bronze Alloys as Replacement for Ni. *Physica Status Solidi (C) Current Topics in Solid State Physics* **2008**, *5*, 3506–3509, doi:10.1002/pssc.200779424.
 33. Beck, U.; Reiners, G.; Urban, I.; Jehn, H.A.; Kopacz, U.; Schack, H. Decorative Hard Coatings: New Layer Systems without Allergy Risk. *Surf Coat Technol* **1993**, *61*, 215–222, doi:10.1016/0257-8972(93)90228-G.
 34. Unveroglu, B.; Zangari, G. Effect of Cell Configuration on the Compositional Homogeneity of Electrodeposited Cu-Zn-Sn Alloys and Phase Purity of the Resulting Cu₂ZnSnS₄ Absorber Layers. *Electrochim Acta* **2017**, *255*, 347–357, doi:10.1016/j.electacta.2017.08.155.
 35. Ahmed, S.; Reuter, K.B.; Gunawan, O.; Guo, L.; Romankiw, L.T.; Deligianni, H. A High Efficiency Electrodeposited Cu₂ZnSnS₄ Solar Cell. *Adv Energy Mater* **2012**, *2*, 253–259, doi:10.1002/aenm.201100526.
 36. Streitberger H; Dössel K *Automotive Paints and Coatings*; Streitberger, H., Dössel, K., Eds.; Wiley, 2008; ISBN 9783527309719.

37. Lipowsky, H.; Arpaci, E. *Copper in the Automotive Industry*; Wiley, 2006; ISBN 9783527317691.
38. Hreid, T.; Li, J.; Zhang, Y.; Spratt, H.J.; Wang, H.; Will, G. Effects of Metal Ion Concentration on Electrodeposited CuZnSn Film and Its Application in Kesterite Cu₂ZnSnS₄ Solar Cells. *RSC Adv* **2015**, *5*, 65114–65122, doi:10.1039/c5ra09966h.
39. Berg, D.M.; Crossay, A.; Guillot, J.; Izquierdo-Roca, V.; Pérez-Rodríguez, A.; Ahmed, S.; Deligianni, H.; Siebentritt, S.; Dale, P.J. Simplified Formation Process for Cu₂ZnSnS₄-Based Solar Cells. *Thin Solid Films* **2014**, *573*, 148–158, doi:10.1016/j.tsf.2014.11.012.
40. Guo, L.; Zhu, Y.; Gunawan, O.; Gokmen, T.; Deline, V.R.; Ahmed, S.; Romankiw, L.T.; Deligianni, H. Electrodeposited Cu₂ZnSnSe₄ Thin Film Solar Cell with 7% Power Conversion Efficiency. *Progress in Photovoltaics: Research and Applications* **2014**, *22*, 58–68, doi:10.1002/pip.2332.
41. Juškeenas, R.; Niaura, G.; Mockus, Z.; Kanapeckaite, S.; Giraitis, R.; Kondrotas, R.; Naujokaitis, A.; Stalnionis, G.; Pakštis, V.; Karpavičiene, V. XRD Studies of an Electrochemically Co-Deposited Cu-Zn-Sn Precursor and Formation of a Cu₂ZnSnSe₄ Absorber for Thin-Film Solar Cells. *J Alloys Compd* **2016**, *655*, 281–289, doi:10.1016/j.jallcom.2015.09.186.
42. Mandich, N. Cyanide Copper Plating Reinvents Itself. *Metal Finishing* **2005**, *103*, 30–36, doi:10.1016/S0026-0576(05)80077-7.
43. Xing, S. Environmentally Friendly Baths for Cu-Sn Co-Electrodeposition: Cyanide-Free Aqueous Bath and Deep Eutectic

Solvents, PhD Thesis. *Environmentally Friendly Baths for Cu-Sn Co-electrodeposition: Cyanide-free Aqueous Bath and Deep Eutectic Solvents* **2014**.

44. Piccinini, N.; Ruggiero, G.N.; Baldi, G.; Robotto, A. Risk of Hydrocyanic Acid Release in the Electroplating Industry. *J Hazard Mater* **2000**, *71*, 395–407, doi:10.1016/S0304-3894(99)00089-8.
45. Mordechay Schlesinger, M.P. *Modern Electroplating*; Schlesinger, M., Paunovic, M., Eds.; John Wiley & Sons, Inc.: Hoboken, NJ, USA, 2010; ISBN 9780470602638.
46. Fujiwara, Y.; Enomoto, H. Electrodeposition of β -Brass from Cyanide Baths with Accumulative Underpotential Deposition of Zn. *J Electrochem Soc* **2000**, *147*, 1840–1846, doi:10.1149/1.1393444.
47. Gamburg, Y.D.; Zangari, G. *Theory and Practice of Metal Electrodeposition*; Springer New York: New York, NY, 2011; ISBN 978-1-4419-9668-8.
48. Bertorelle, E. *Trattato Di Galvanotecnica*; Hoepli, Ed.; Hoepli, 2016; ISBN 9788820374990.
49. Strow, H. Brass and Bronze Plating. *Metal Finishing* **2007**, *105*, 163–167, doi:10.1016/S0026-0576(07)80330-8.
50. Brian, E. Studies of Bronze Electrodeposition. **1992**.
51. Brooman, E.W. Corrosion Behavior of Environmentally Acceptable Alternatives to Nickel Coatings. *Metal Finishing* **2001**, *99*, 100–102, doi:10.1016/S0026-0576(01)81296-4.

52. Powell, C.; Webster, P. Copper Alloys for Marine Environments. **2011**, 33.
53. Brasses, A. Section 7 – BRASSES FOR CORROSION RESISTANCE. 45–60.
54. Lyon, S.B. Corrosion of Tin and Its Alloys. *Shreir's Corrosion* **2010**, 2068–2077, doi:10.1016/B978-044452787-5.00099-8.
55. Muller, J.; Laïk, B.; Guillot, I. α -CuSn Bronzes in Sulphate Medium: Influence of the Tin Content on Corrosion Processes. *Corros Sci* **2013**, 77, 46–51, doi:10.1016/j.corsci.2013.07.025.
56. Sohn, S.; Kang, T. The Effects of Tin and Nickel on the Corrosion Behavior of 60Cu-40Zn Alloys. *J Alloys Compd* **2002**, 335, 281–289, doi:10.1016/S0925-8388(01)01839-4.
57. El-Mahdy, G.A. Electrochemical Impedance Study on Brass Corrosion in NaCl and (NH₄)₂SO₄ solutions during Cyclic Wet-Dry Conditions. *J Appl Electrochem* **2005**, 35, 347–353, doi:10.1007/s10800-004-8347-1.
58. Kleber, Ch.; Schreiner, M. Multianalytical In-Situ Investigations of the Early Stages of Corrosion of Copper, Zinc and Binary Copper/Zinc Alloys. *Corros Sci* **2003**, 45, 2851–2866, doi:10.1016/S0010-938X(03)00113-6.
59. Altomare, A.; Corriero, N.; Cuocci, C.; Falcicchio, A.; Moliterni, A.; Rizzi, R. QUALX2.0: A Qualitative Phase Analysis Software Using the Freely Available Database POW-COD. *J Appl Crystallogr* **2015**, 48, 598–603, doi:10.1107/S1600576715002319.

60. Toby, B.H.; Von Dreele, R.B. GSAS-II: The Genesis of a Modern Open-Source All Purpose Crystallography Software Package. *J Appl Crystallogr* **2013**, *46*, 544–549, doi:10.1107/S0021889813003531.
61. Taylor, J.L. Reflectance Measurements of Materials Used in the Solar Industry Selecting the Appropriate Accessories for UV / Vis / NIR Measurements.
62. Giaccherini, A. Multispectra Software Available online: <https://github.com/AndreaGiaccherini> (accessed on 7 February 2020).
63. Sjö Dahl, M. ColorMath—a Package for Color Summed Calculations in SU(N c). *The European Physical Journal C* **2013**, *73*, 2310, doi:10.1140/epjc/s10052-013-2310-4.
64. Illumination, I.C. on Colorimetry - Part 4 : CIE 1976 L * a * b * COLOUR. **2007**.
65. Oniciu, L.; Mure\csan, L. Some Fundamental Aspects of Levelling and Brightening in Metal Electrodeposition. *J Appl Electrochem* **1991**, *21*, 565–574, doi:10.1007/BF01024843.
66. Portela, A.L.; Lacconi, G.I.; Lo, M. Nicotinic Acid as Brightener Agent in Copper Electrodeposition. **2001**, *495*, 169–172.
67. Survila, A.; Mockus, Z.; Kanapeckaitė, S.; Bražinskiene, D.; Juške nas, R.; Kanapeckaitė, S.; Bražinskienė, D.; Juškė nas, R. Surfactant Effects in Cu-Sn Alloy Deposition. *J Electrochem Soc* **2012**, *159*, D296--D302, doi:10.1149/2.084205jes.
68. Ritchie, N.W.M.; Davis, J.; Newbury, D.E. DTSA-II: A New Tool for Simulating and Quantifying EDS Spectra - Application to Difficult

- Overlaps. *Microscopy and Microanalysis* **2008**, *14*, 1176–1177, doi:10.1017/S143192760808361X.
69. Llovet, X.; Salvat, F. PENEPMA: A Monte Carlo Program for the Simulation of X-Ray Emission in Electron Probe Microanalysis. *Microscopy and Microanalysis* **2017**, *23*, 634–646, doi:10.1017/S1431927617000526.
70. Demers, H.; Horny, P.; Gauvin, R.; Lifshin, E. WinX-Ray: A New Monte Carlo Program for the Simulation of X-Ray and Charging Materials. *Microscopy and Microanalysis* **2002**, *8*, 1498–1499, doi:10.1017/s1431927602104120.
71. Giurlani, W.; Berretti, E.; Innocenti, M.; Lavacchi, A. Coating Thickness Determination Using X-Ray Fluorescence Spectroscopy: Monte Carlo Simulations as an Alternative to the Use of Standards. *Coatings* **2019**, *9*, 79, doi:10.3390/coatings9020079.
72. Hovington, P.; Drouin, D.; Gauvin, R. CASINO: A New Monte Carlo Code in C Language for Electron Beam Interaction -Part I: Description of the Program. *Scanning* **2006**, *19*, 1–14, doi:10.1002/sca.4950190101.
73. Goldstein, J.I.; Newbury, D.E.; Echlin, P.; Joy, D.C.; Lyman, C.E.; Lifshin, E.; Sawyer, L.; Michael, J.R. Quantitative X-Ray Analysis: The Basics. In *Scanning Electron Microscopy and X-ray Microanalysis*; Springer US: Boston, MA, 2003; pp. 391–451.
74. Rouxhet, P.G.; Genet, M.J. XPS Analysis of Bio-Organic Systems. *Surface and Interface Analysis* **2011**, *43*, 1453–1470, doi:10.1002/sia.3831.

75. Ertl, G.; Hierl, R.; Knözinger, H.; Thiele, N.; Urbach, H.P. XPS Study of Copper Aluminate Catalysts. *Applications of Surface Science* **1980**, *5*, 49–64, doi:10.1016/0378-5963(80)90117-8.
76. Kövér, L.; Kovács, Z.; Sanjinés, R.; Moretti, G.; Cserny, I.; Margaritondo, G.; Pálincás, J.; Adachi, H. Electronic Structure of Tin Oxides: High-resolution Study of XPS and Auger Spectra. *Surface and Interface Analysis* **1995**, *23*, 461–466, doi:10.1002/sia.740230705.
77. Deroubaix, G.; Marcus, P. X-ray Photoelectron Spectroscopy Analysis of Copper and Zinc Oxides and Sulphides. *Surface and Interface Analysis* **1992**, *18*, 39–46, doi:10.1002/sia.740180107.
78. Cavallotti, P.L.; Nobili, L.; Vincenzo, A. Phase Structure of Electrodeposited Alloys. *Electrochim Acta* **2005**, *50*, 4557–4565, doi:10.1016/j.electacta.2005.03.060.
79. Girin, O.; Alloy, E.; Phase, I.; Material, M.; Composition, P. Phase and Structure Formation of Metallic Materials Electrodeposited via a Liquid State Stage : New Experimental Proof. **2010**, *304*, 99–105, doi:10.4028/www.scientific.net/DDF.303-304.99.
80. Petzow, G.; Henig, E.Th.; Lukas, H.L.; Aldinger, F.; Prince, A. Comprehensive Handbook of Ternary Alloy Phase Diagrams. *Bulletin of Alloy Phase Diagrams* **1980**, *1*, 36–40, doi:10.1007/BF02881177.
81. Lei, W.X.; Pan, Y.; Zhou, Y.C.; Zhou, W.; Peng, M.L.; Ma, Z.S. RSC Advances CNTs – Cu Composite Layer Enhanced Sn – Cu Alloy as High Performance Anode Materials for Lithium- Ion Batteries. **2014**, 3233–3237, doi:10.1039/c3ra44431g.

82. Guy, A.G. *Elements of Physical Metallurgy*; Addison-Wesley Press, Ed.; 1951; ISBN 0201026333.
83. Constantinides, I.; Adriaens, A.; Adams, F. Surface Characterization of Artificial Corrosion Layers on Copper Alloy Reference Materials. *Appl Surf Sci* **2002**, *189*, 90–101, doi:10.1016/S0169-4332(02)00005-3.
84. Spilker, H.G.; Jänsch-Kaiser, G.; Pérez, N. Copper-Zinc Alloys (Brass). In *Corrosion Handbook*; Wiley-VCH Verlag GmbH & Co. KGaA: Weinheim, Germany, 2012; p. NA-NA.
85. Marušić, K.; Ćurković, H.O.; Lisac, E.S.; Takenouti, H. Two Imidazole Based Corrosion Inhibitors for Protection of Bronze from Urban Atmospheres. *Croatica Chemica Acta* **2018**, *91*, 435–446, doi:10.5562/cca3440.
86. Marušić, K.; Ćurković, H.O.; Takenouti, H. Inhibiting Effect of 4-Methyl-1-p-Tolylimidazole to the Corrosion of Bronze Patinated in Sulphate Medium. *Electrochim Acta* **2011**, *56*, 7491–7502, doi:10.1016/j.electacta.2011.06.107.
87. Marušić, K.; Ćurković, H.O.; Takenouti, H. Corrosion Inhibition of Bronze and Its Patina Exposed to Acid Rain. *J Electrochem Soc* **2013**, *160*, C356–C363, doi:10.1149/2.063308jes.
88. Lindsay, J.H. Decorative and Hard Chromium Plating. *Plating and Surface Finishing* **1997**, *84*, 50–51.
89. Ohmi, T.; Nakagawa, Y.; Nakamura, M.; Ohki, A.; Koyama, T. Formation of Chromium Oxide on 316L Austenitic Stainless Steel. *Journal of Vacuum Science & Technology A: Vacuum, Surfaces, and Films* **1998**, *14*, 2505, doi:10.1116/1.580010.

90. Durney, L.J. *Electroplating Engineering Handbook*; Springer US, 1996; ISBN 978-0-412-74110-4.
91. Taylor, S.R. Coatings for Corrosion Protection: Metallic. In *Encyclopedia of Materials: Science and Technology*; Elsevier, 2001; pp. 1–5.
92. Schlesinger, M.; Paunovic, M. *Modern Electroplating*; Wiley, 2010; ISBN 9780470602638.
93. Wang, Y.; Su, H.; Gu, Y.; Song, X.; Zhao, J. Carcinogenicity of Chromium and Chemoprevention: A Brief Update. *Onco Targets Ther* **2017**, *10*, 4065, doi:10.2147/OTT.S139262.
94. Kim, J.; Seo, S.; Kim, Y.; Kim, D.H. Review of Carcinogenicity of Hexavalent Chrome and Proposal of Revising Approval Standards for an Occupational Cancers in Korea. *Ann Occup Environ Med* **2018**, *30*, 7, doi:10.1186/S40557-018-0215-2.
95. Restricted Substances by Annex XVII to REACH Regulation.
96. Baral, A.; Engelken, R.D. Chromium-Based Regulations and Greening in Metal Finishing Industries in the USA. *Environ Sci Policy* **2002**, *5*, 121–133, doi:10.1016/S1462-9011(02)00028-X.
97. Legg, K.O.; Graham, M.; Chang, P.; Rastagar, F.; Gonzales, A.; Sartwell, B. The Replacement of Electroplating. *Surf Coat Technol* **1996**, *81*, 99–105, doi:10.1016/0257-8972(95)02653-3.
98. Del Pianta, D.; Frayret, J.; Gleyzes, C.; Cugnet, C.; Dupin, J.C.; Le Hecho, I. Determination of the Chromium(III) Reduction Mechanism during

- Chromium Electroplating. *Electrochim Acta* **2018**, *284*, 234–241, doi:10.1016/J.ELECTACTA.2018.07.114.
99. Dennis, J.K.; Such, C.E. *Nickel and Chromium Plating*; Woodhead Publishing, 1993;
 100. Leimbach, M.; Tschaar, C.; Zapf, D.; Kurniawan, M.; Schmidt, U.; Bund, A. Relation between Color and Surface Morphology of Electrodeposited Chromium for Decorative Applications. *J Electrochem Soc* **2019**, *166*, D205, doi:10.1149/2.0871906JES.
 101. Leimbach, M.; Tschaar, C.; Schmidt, U.; Bund, A. Low-Frequency Pulse Plating for Tailoring the Optical Appearance of Chromium Layers for Decorative Applications. *Journal of Applied Electrochemistry* **2020** *50*:4 **2020**, *50*, 489–499, doi:10.1007/S10800-020-01406-3.
 102. Aguilar, M.; Barrera, E.; Palomar-Pardavé, M.; Huerta, L.; Muhl, S. Characterization of Black and White Chromium Electrodeposition Films: Surface and Optical Properties. *J Non Cryst Solids* **2003**, *329*, 31–38, doi:10.1016/J.JNONCRYSOL.2003.08.008.
 103. Chien, C.W.; Liu, C.L.; Chen, F.J.; Lin, K.H.; Lin, C.S. Microstructure and Properties of Carbon–Sulfur-Containing Chromium Deposits Electroplated in Trivalent Chromium Baths with Thiosalicylic Acid. *Electrochim Acta* **2012**, *72*, 74–80, doi:10.1016/J.ELECTACTA.2012.03.168.
 104. Leimbach, M.; Tschaar, C.; Schmidt, U.; Bund, A. Low-Frequency Pulse Plating for Tailoring the Optical Appearance of Chromium Layers for Decorative Applications. *J Appl Electrochem* **2020**, *50*, 489–499, doi:10.1007/S10800-020-01406-3/FIGURES/9.

105. Polukarov, Y.M.; Safonov, V.A.; Edigaryan, A.A.; Vykhodtseva, L.N. Chrome Plating from Sulfate–Oxalate Cr(III) Baths. Structure, Composition, and Corrosion Behavior. *Protection of Metals* **2001**, *37*, 447–451, doi:10.1023/A:1012366130428.
106. Lansdell, P.; Farr, J.P.G. The Corrosion Resistance of Chromium Electroplated from Trivalent and Hexavalent Chromium Plating Solutions. <http://dx.doi.org/10.1080/00202967.1997.11871178> **2017**, *75*, 219–223, doi:10.1080/00202967.1997.11871178.
107. He, X.; Li, C.; Zhu, Q.; Hou, B.; Jiang, Y.; Wu, L. Electrochemical Mechanism of Cr(III) Reduction for Preparing Crystalline Chromium Coatings Based on 1-Butyl-3-Methylimidazolium Hydrogen Sulfate Ionic Liquid. *RSC Adv* **2014**, *4*, 64174–64182, doi:10.1039/C4RA12335B.
108. Abbott, A.P.; Capper, G.; Davies, D.L.; Rasheed, R.K.; Archer, J.; John, C. Electrodeposition of Chromium Black from Ionic Liquids. <http://dx.doi.org/10.1080/00202967.2004.11871547> **2017**, *82*, 14–17, doi:10.1080/00202967.2004.11871547.
109. Verdonck, T.; Verpoort, P.; Strycker, J. De; Cleene, A. De; Banerjee, D.; Nockemann, P.; Deun, R. Van; Hecke, K. Van Chromium(III) in Deep Eutectic Solvents: Towards a Sustainable Chromium(VI)-Free Steel Plating Process. *Green Chemistry* **2019**, *21*, 3637–3650, doi:10.1039/C9GC00690G.
110. Chen, H.; Wang, X.; Zhang, R. Application and Development Progress of Cr-Based Surface Coatings in Nuclear Fuel Element: I. Selection,

- Preparation, and Characteristics of Coating Materials. *Coatings* **2020**, *Vol. 10*, Page 808 **2020**, *10*, 808, doi:10.3390/COATINGS10090808.
111. Baptista, A.; Silva, F.J.G.; Porteiro, J.; Míguez, J.L.; Pinto, G.; Fernandes, L. On the Physical Vapour Deposition (PVD): Evolution of Magnetron Sputtering Processes for Industrial Applications. *Procedia Manuf* **2018**, *17*, 746–757, doi:10.1016/J.PROMFG.2018.10.125.
 112. Constantin, R.; Miremad, B. Performance of Hard Coatings, Made by Balanced and Unbalanced Magnetron Sputtering, for Decorative Applications. *Surf Coat Technol* **1999**, *120–121*, 728–733, doi:10.1016/S0257-8972(99)00366-7.
 113. Fenker, M.; Jackson, N.; Spolding, M.; Nicole, P.; Schönhut, K.; Gregory, G.; Hovsepian, P.E.; Münz, W.D. Corrosion Performance of PVD-Coated and Anodised Materials for the Decorative Market. *Surf Coat Technol* **2004**, *188–189*, 466–472, doi:10.1016/J.SURFCOAT.2004.08.054.
 114. Mattox, D.M. *The Foundations of Vacuum Coating Technology*; Elsevier, 2003; ISBN 978-3-662-10329-6.
 115. Martyak, N.M.; McCaskie, J.E.; Voos, B.; Plieth, W. Microcracks in Chromium Electrodeposits. *Journal of Materials Science* **1997** *32:22*, *32*, 6069–6073, doi:10.1023/A:1018639800595.
 116. Thornton, J.A.; Hoffman, D.W. Stress-Related Effects in Thin Films. *Thin Solid Films* **1989**, *171*, 5–31, doi:10.1016/0040-6090(89)90030-8.
 117. Mattox, D.M. *Handbook of Physical Vapor Deposition (PVD) Processing*; 2nd ed.; Elsevier Inc., 2010;

118. *Handbook of Sputter Deposition Technology*; Wasa, K., Kanno, I., Kotera, H., Eds.; 2nd ed.; Elsevier Inc., 2012;
119. Krella, A. Resistance of PVD Coatings to Erosive and Wear Processes: A Review. *Coatings* **2020**, *Vol. 10*, Page 921 **2020**, *10*, 921, doi:10.3390/COATINGS10100921.
120. *Magnetron Sputtering System Market Size, Market Share, Application Analysis, Regional Outlook, Growth Trends, Key Players, Competitive Strategies and Forecasts, 2020 To 2028*; 2021;
121. Cialone, M.; Fernandez-Barcia, M.; Celegato, F.; Coisson, M.; Barrera, G.; Uhlemann, M.; Gebert, A.; Sort, J.; Pellicer, E.; Rizzi, P.; et al. A Comparative Study of the Influence of the Deposition Technique (Electrodeposition versus Sputtering) on the Properties of Nanostructured Fe₇₀Pd₃₀ Films. *Sci Technol Adv Mater* **2020**, *21*, 424–434, doi:10.1080/14686996.2020.1780097.
122. Giroire, B.; Ali Ahmad, M.; Aubert, G.; Teule-Gay, L.; Michau, D.; Watkins, J.J.; Aymonier, C.; Poulon-Quintin, A. A Comparative Study of Copper Thin Films Deposited Using Magnetron Sputtering and Supercritical Fluid Deposition Techniques. *Thin Solid Films* **2017**, *643*, 53–59, doi:10.1016/J.TSF.2017.09.002.
123. Liang, A.; Zhang, J. Why the Decorative Chromium Coating Electrodeposited from Trivalent Chromium Electrolyte Containing Formic Acid Is Darker. *Surf Coat Technol* **2012**, *206*, 3614–3618, doi:10.1016/J.SURFCOAT.2012.02.053.

124. Anders, A. A Structure Zone Diagram Including Plasma-Based Deposition and Ion Etching. *Thin Solid Films* **2010**, *518*, 4087–4090, doi:10.1016/J.TSF.2009.10.145.
125. Huttunen-Saarivirta, E.; Rajala, P.; Bomberg, M.; Carpén, L. EIS Study on Aerobic Corrosion of Copper in Ground Water: Influence of Micro-Organisms. *Electrochim Acta* **2017**, *240*, 163–174, doi:10.1016/J.ELECTACTA.2017.04.073.